

Department of Physics and Astronomy

University of Heidelberg

Master thesis in Physics

submitted by

Hannah Klungenmeyer

born in Heidelberg

2017

Tracklet-based particle identification with the ALICE TRD for LHC RUN 3

This Master thesis has been carried out by Hannah Klingenmeyer
at the
Physikalisches Institut Heidelberg
under the supervision of
Prof. Dr. Johanna Stachel

Abstract

The Transition Radiation Detector (TRD) at the LHC (CERN) provides electron identification as well as particle tracking in the central barrel of ALICE. To cope with the increased collision rates planned for LHC RUN 3, the read-out speed of the TRD has to be increased. It is foreseen to reduce the data volume by reading out online-processed track segments instead of the raw data. These track segments, also referred to as tracklets, contain information about position, incident angle and Particle IDentification (PID), which is currently read out in 32-bit words. The challenge of the tracklet-only read-out for RUN 3 in terms of PID will be to ensure an adequate PID performance using only the information from the tracklet word, instead of the raw data as in RUN 1 and RUN 2. To this end, a change in the mode of operation of the TRD Front-End Electronics (FEE) regarding the calculation of the tracklet PID is foreseen for RUN 3.

In this thesis, various possible scenarios for the PID calculation in the FEE for RUN 3 are defined in the form of sets of three different parameters. The method for the evaluation of the tracklet-based PID performance is developed and applied to the data generated in a Monte Carlo (MC) simulation, which was specifically produced for this thesis. Using a multi-dimensional likelihood approach, the pion efficiency is determined for the various parameter sets as a means to judge the quality of the PID performance. In the end, the two best suited sets of parameters are presented in a proposal of implementation in the FEE. For these sets, a pion efficiency $\leq 4.4 \cdot 10^{-3}$ and $\leq 5.4 \cdot 10^{-3}$ at 90% electron efficiency can be achieved for negatively and positively charged tracklets, respectively.

Zusammenfassung

Der Übergangsstrahlungsdetektor (TRD) am LHC (CERN) ermöglicht die Identifikation von Elektronen und die Rekonstruktion von Teilchenspuren in ALICE bei mittlerer Rapidität. Um die für den LHC RUN 3 geplanten Kollisionsraten im TRD bewältigen zu können, muss die Auslesegeschwindigkeit erhöht werden. Hierfür ist vorgesehen, das Datenvolumen durch die Auslese von online-berechneten Spursegmenten anstatt der Rohdaten zu reduzieren. Die Spursegmente, die des Weiteren als „tracklets“ bezeichnet werden, enthalten Informationen bezüglich der Position, des Einfallswinkels und der Teilchenidentifikation (PID). Diese Informationen werden derzeit in 32 bit-Wörtern ausgelesen. Da im bisherigen Betrieb des TRD die Rohdaten zur Teilchenidentifikation verwendet werden konnten, besteht die Herausforderung künftig darin, eine angemessene Qualität der Teilchenidentifikation basierend auf den Informationen der tracklets zu gewährleisten. Dazu ist eine Veränderung der Arbeitsweise der Frontend-Elektronik (FEE) bezüglich der PID-Berechnung für die tracklets für RUN 3 vorgesehen.

In dieser Arbeit werden verschiedene mögliche Einstellungen der FEE für die PID-Berechnung in RUN 3 festgelegt, die durch einen Satz von drei verschiedenen Parametern definiert werden. Des Weiteren wird eine Methode zur Auswertung der Qualität der Teilchenidentifikation entwickelt und auf Daten angewendet, die aus einer eigens für diese Arbeit produzierten Monte Carlo (MC)-Simulation stammen. Mit Hilfe einer Methode zur mehr-dimensionalen Wahrscheinlichkeitsberechnung wird die Pioneffizienz für die verschiedenen Parameter-Sätze bestimmt, um ein Maß für die Qualität der Teilchenidentifikation zu erhalten. Schlussendlich werden die Parameterkombinationen präsentiert, die sich am besten zur Teilchenidentifikation in RUN 3 eignen und daher in der FEE verwendet werden sollten. Für diese Parameter kann eine Pioneffizienz $\leq 4.4 \cdot 10^{-3}$ bzw. $\leq 5.4 \cdot 10^{-3}$ bei einer Elektroneffizienz von 90% für negativ bzw. positiv geladene tracklets erreicht werden.

Contents

1	Introduction	1
2	Theoretical background	3
2.1	The Standard Model of particle physics	3
2.2	The Quark–Gluon Plasma	6
2.3	Probing the Quark–Gluon Plasma	7
3	ALICE at the LHC	9
3.1	The Large Hadron Collider	9
3.2	A Large Ion Collider Experiment	11
3.2.1	Global coordinate system	12
3.2.2	Central barrel detectors	13
3.3	Data processing	14
4	The Transition Radiation Detector	17
4.1	Detector overview	17
4.1.1	TRD structure	17
4.1.2	Local coordinate system	18
4.2	Chamber layout and principle of operation	19
4.3	Signal processing and read-out	23
4.3.1	The front-end electronics	23
4.3.2	The global tracking unit	24
4.4	Operation in RUN 1 and RUN 2	25
4.4.1	Triggering and raw data transfer	25
4.4.2	Offline tracking	27
4.4.3	Offline particle identification	28
4.5	Integration into AliRoot	28
5	Upgrade considerations for RUN 3	31
5.1	The ALICE upgrade for RUN 3	31
5.2	The TRD upgrade strategy	32
5.2.1	Read-out modes	32
5.2.2	Possible tracklet formats	33
5.2.3	Constraints	34
6	The analysis method	37
6.1	Data access	37

6.2	Offline track sample	38
6.2.1	Track quality	38
6.2.2	Track identification	39
6.3	Tracklet matching and processing	39
6.3.1	Matching procedure	39
6.3.2	Tracklet cluster processing	42
6.3.3	z -row merging	43
6.3.4	Double-tracklet rejection	44
7	Evaluation of the tracklet-based PID approach	47
7.1	The multi-dimensional likelihood method	47
7.1.1	Likelihood in one dimension	47
7.1.2	Extension to two and three dimensions	52
7.2	Analysis strategy for the tracklet-based PID	57
7.2.1	Definition of samples	57
7.2.2	Transformation to n bits	58
7.3	Performance evaluation	60
7.3.1	Prior considerations	60
7.3.2	Performance using the linear function	63
7.3.3	Performance using the non-linear function	75
8	Proposal for implementation	79
9	Summary and outlook	83
A	Tracklet-based PID analysis	85
A.1	Monte Carlo simulation	85
A.2	Track cuts	85
A.3	LQND results	86
B	Acronyms	101
	Bibliography	103

Chapter 1

Introduction

Since the end of the 19th century, the field of particle physics has been growing and evolving continuously, ever improving our understanding of the laws of nature and the constituents of matter. Following the discovery of the electron by J. J. Thompson in 1897 [1], soon other particles were observed: in 1919, E. Rutherford reported the discovery of the proton [2], and later suggested the existence of the neutron, which was found in 1932 by J. Chadwick [3]. 1932 also saw the discovery of the positron by C. D. Anderson [4], who again had a part in the first detection of another particle, the muon, in 1936/37 [5, 6]. Furthermore, measurements of the β^- decay prompted W. Pauli in 1933 to postulate another particle, the neutrino, to explain the measured energy spectrum. In 1956, the neutrino was discovered [7], and added to the growing “zoo” of particles.

As the binding between protons and neutrons within the atomic nucleus could not be explained by the already well-known electromagnetic force, another form of interaction was proposed [8]. It was predicted to be short-ranged and stronger than the electromagnetic interaction, and was therefore called the *strong force*. Further discoveries of strongly interacting particles — called *hadrons* — included, for example, the neutral and charged pions and kaons in 1947 [9, 10]. Subsequent investigations of their properties finally led to the conclusion that all hadrons consist of even smaller building blocks, the *quarks*, which were first predicted independently by M. Gell-Mann and G. Zweig in 1964 [11, 12], and could be indirectly verified in deep inelastic scattering experiments in 1969 [13]. The quarks interact strongly with each other by exchanging the mediators of the strong force, the *gluons* (indirectly observed for the first time in 1979 [14]). Experimentally, it was found that quarks only exist in groups, i.e. as hadrons, and not on their own — a property which is known as *confinement*.

Today, our understanding of the elementary particles and their interactions is summarised in the *Standard Model of particle physics* [15]. Although the Standard Model was developed in the early 1970s, it has only recently been completely confirmed experimentally, when in 2012 the Higgs boson was discovered at the Large Hadron Collider (LHC) [16, 17]. The LHC, which is built at CERN, the European Organisation for Nuclear Research, is the largest and most powerful hadron collider currently in existence [18]. It is an important tool to investigate predictions made by the Standard Model — be it the discovery of a new particle like the Higgs boson, or the measurement of particle or interaction properties. The quantum field theory

for the strong interaction, *Quantum ChromoDynamics (QCD)*, for example predicts a state at either high temperatures and/or high densities where quarks and gluons are *asymptotically free*, i.e. (almost) no longer confined. Investigating this state of matter, which is assumed to have existed shortly after the Big Bang [19] and is commonly referred to as the *Quark–Gluon Plasma (QGP)* [20], is the goal of A Large Ion Collider Experiment (ALICE) [21], one of the four major experiments at the LHC. For this purpose, the LHC collides lead ions at energies of several TeV to create a QGP. ALICE in turn was designed and optimised to observe these collisions, and thus is able to detect QGP signatures. Measuring the properties of particles which were created before the QGP has formed and which have been influenced by it, or of particles which originate from the QGP itself, makes it possible to draw conclusions about the formation and evolution of the QGP. In addition, for some probes it is useful to study their behaviour in proton–proton collisions as well, where no QGP is expected to have formed. Subsequently, the measurements from pp and Pb–Pb collisions can be compared in order to distinguish effects that are truly caused by the quark–gluon plasma from those present in both collision systems.

Some of the QGP probes ALICE is interested in have a short lifetime and therefore decay before they even reach the experiment. In this case, it is the decay products which are detected by ALICE. A number of important probes (e.g. quarkonia like the J/Ψ , or heavy-flavour mesons like the D mesons) can decay into electrons. One sub-detector of ALICE, the Transition Radiation Detector (TRD), is therefore built specifically with the purpose of identifying electrons and measuring their properties [22]. The modification and evaluation of the Particle IDentification (PID) performance of the TRD for the LHC’s third operational run phase, called RUN 3 and set to start in 2021, is the topic of this thesis.

Following this introduction, the theoretical background relevant for this thesis — in particular a description of the Standard Model and of the QGP — is provided in Chapter 2. A short introduction on the LHC and ALICE is given in Chapter 3, with a more detailed description of the TRD and its operation in Chapter 4. Subsequently, Chapter 5 provides an overview of the upgrade plans of ALICE for LHC RUN 3 and the implications of this upgrade, especially for particle identification with the TRD.

The evaluation of the PID performance under the constraints imposed by the planned upgrade is the main subject of this thesis. Therefore, Chapter 6 describes the technical implementation of the analysis of the PID performance, while the actual performance study is discussed in Chapter 7. Chapter 8 makes a proposal on how to implement particle identification with the TRD in RUN 3. Finally, Chapter 9 provides a brief summary of this thesis.

Chapter 2

Theoretical background

Investigating the properties of the quark–gluon plasma is one of the motivations for building and operating ALICE. To understand the requirements which have to be fulfilled by the experiment to detect signatures of the QGP, a short overview of the theory of interest is given in this chapter. Following a description of the Standard Model, which serves as a brief introduction to the fundamental particles and forces (in particular quarks and gluons), the second half of this chapter is concerned with the description and observation of the quark–gluon plasma. When discussing suitable probes of the QGP, the focus lies primarily on those which involve electrons, as electron identification is one of the purposes of the TRD.

2.1 The Standard Model of particle physics

In the Standard Model of particle physics, our present understanding of the elementary particles and the interactions between them is summarised [15]. Many theoretical concepts and predictions of the Standard Model have been measured and tested experimentally, some to extremely high precision, thus making the Standard Model one of the most successful models in modern physics. And yet, it is clear that it is not a complete “theory of everything”, able to entirely describe our Universe, since there are a number of phenomena not (yet) included: the matter–antimatter asymmetry observed in the Universe can only be insufficiently explained; it has not yet been possible to combine the theory of gravity, General Relativity, with the quantum field theories contained in the Standard Model; and no explanation is offered for dark matter and dark energy, which have been found by cosmological and astrophysical experiments to make up almost the entire matter–energy density in the Universe [15]. To advance in the search for these phenomena of new physics, it is of great interest for particle physicists around the globe to further investigate and test the limitations of the Standard Model in experiments, with the LHC being one of many facilities all over the world to contribute to this search.

In general, the content of this section is based on [15], unless specified otherwise.

In the Standard Model, the fundamental particles can be classified based on their spin, as shown in Fig. 2.1: *fermions*, which carry a half-integer spin, are described by Fermi–Dirac statistics — hence the name “fermion”. There are twelve fermions (and their corresponding anti-particles) in the Standard Model, which can again be

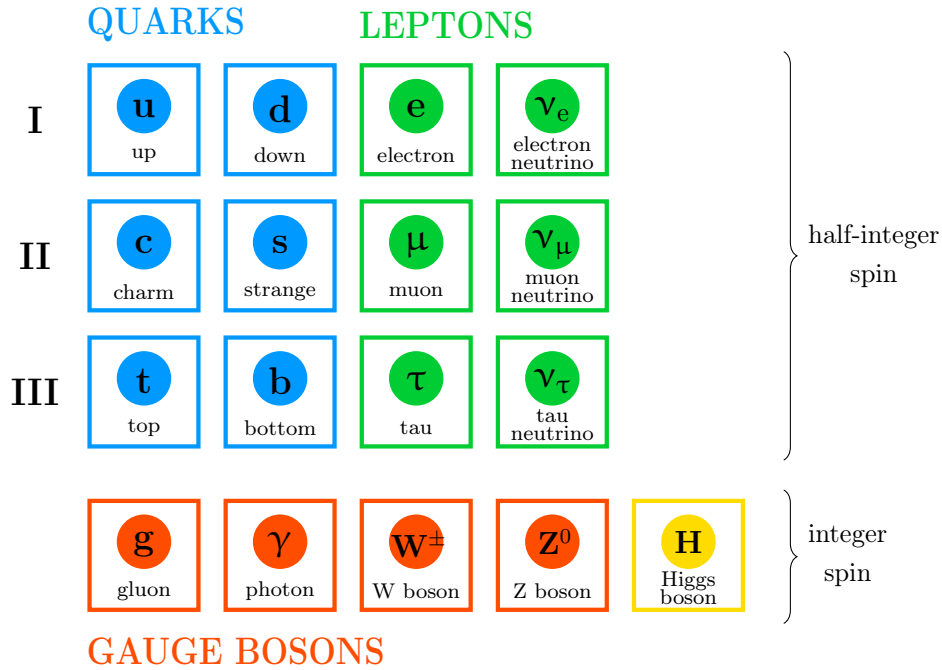


Figure 2.1: Visualisation of the Standard Model of particle physics [23] (sketch based on [24]). The twelve fermions, which are sorted into three generations based on their discoveries, carry half-integer spins, while the four gauge bosons and the Higgs boson carry integer spins.

divided into two groups: quarks and leptons both carry a spin of $1/2$, but differ in the interactions they partake in. They are sorted into three generations, where the up quark, the down quark, the electron, and the electron neutrino make up the first generation. The second and third generation particles are basically “copies” of their first generation counterpart in all aspects except for their mass.

Particles with an integer spin, which are described by Bose–Einstein statistics, are called *bosons*. The Standard Model contains four bosons with a spin of 1, which mediate the fundamental interactions and are called gauge bosons. Finally, the Higgs boson with a spin of 0 is associated with the Higgs mechanism, which is responsible for the mass of the elementary particles.

Table 2.1 summarises some of the most important properties of the fundamental fermions, with the leptons described in the left and the quarks in the right column. All twelve particles participate in the weak interaction, which is mediated either by a W^\pm or a Z^0 boson. Except for the neutrinos, which are electrically neutral, the remaining nine fermions carry an electric charge and can interact electromagnetically via the exchange of a photon. The six quark types, or *flavours* — up, down, charm, strange, top, and bottom — carry an additional *colour charge*, which allows them to partake in the strong interaction, mediated by the gluon. The quarks are held together by the strong force in bound states, the hadrons, which are classified based

leptons				quarks			
particle		Q	mass	particle		Q	mass
electron	(e^-)	-1	$511.0 \text{ keV}/c^2$	up	(u)	$2/3$	$2.2 \text{ MeV}/c^2$
neutrino	(ν_e)	0	$< 1 \text{ eV}/c^2$	down	(d)	$-1/3$	$4.7 \text{ MeV}/c^2$
muon	(μ^-)	-1	$105.7 \text{ MeV}/c^2$	charm	(c)	$2/3$	$1.3 \text{ GeV}/c^2$
neutrino	(ν_μ)	0	$< 1 \text{ eV}/c^2$	strange	(s)	$-1/3$	$96 \text{ MeV}/c^2$
tau	(τ^-)	-1	$1.8 \text{ GeV}/c^2$	top	(t)	$2/3$	$173.2 \text{ GeV}/c^2$
neutrino	(ν_τ)	0	$< 1 \text{ eV}/c^2$	bottom	(b)	$-1/3$	$4.2 \text{ GeV}/c^2$

Table 2.1: Properties of the fundamental fermions [23]. The charge Q is given in units of the electron charge e . Note that the neutrino masses must be considered with care, as the flavour eigenstates ν_e , ν_μ and ν_τ are actually mixtures of the mass eigenstates (denoted simply as ν_1 , ν_2 and ν_3 [15]). However, the neutrino masses have not been determined yet; therefore, only an upper limit is given.

on their quark content: *mesons* always contain a quark–antiquark pair (commonly denoted as $q\bar{q}$), while *(anti)baryons* consist of three (anti)quarks (qqq and $\bar{q}\bar{q}\bar{q}$, respectively). The most common examples for baryons are the proton, comprised of two up-quarks and a down-quark, $p(uud)$, and the neutron, which contains two down-quarks and an up-quark, $n(udd)$. The most abundant mesons, on the other hand, are the pions, which consist of a combination of up- and down-quarks, $\pi^+(u\bar{d})$, $\pi^-(d\bar{u})$, and $\pi^0(\frac{1}{\sqrt{2}}(u\bar{u} - d\bar{d}))$.

interaction	gauge boson	mass	coupling to
electromagnetic	photon (γ)	0	electric charge
weak	W boson (W^\pm)	$80.4 \text{ GeV}/c^2$	weak charge, electric charge
	Z boson (Z^0)	$91.2 \text{ GeV}/c^2$	weak charge
strong	gluon (g)	0	colour charge

Table 2.2: Properties of the gauge bosons of the electromagnetic, weak and strong interactions [23].

In the Standard Model, the fundamental interactions (excluding gravity) are described by quantum field theories, which explain the forces as exchanges of particles, the gauge bosons. A brief overview of the gauge bosons is given in Table 2.2. The fundamental theory describing the electromagnetic force is the theory of Quantum ElectroDynamics (QED), and the exchanged gauge boson is the massless neutral photon. The weak interaction, on the other hand, is mediated by two types of heavy gauge bosons, the charged W boson (which carries a charge of $\pm 1e$) and the neutral Z boson. In the 1960s, Glashow, Salam and Weinberg succeeded in unifying the

electromagnetic and the weak interaction into one theory, which earned them the Nobel Prize in Physics in 1979 [25]. Finally, the strong interaction is described by the already mentioned theory of Quantum ChromoDynamics, with eight massless gluons as its gauge bosons.

2.2 The Quark–Gluon Plasma

Although there are many experiments which have searched for them, single free quarks have not been detected directly yet. This behaviour is known as colour confinement, meaning that colour must be confined within a particle, i.e. every free particle must be colourless. Therefore, a quark carrying e.g. a red (r) colour charge must exist in a bound state, either with two other quarks carrying the complementary colour charges green (g) and blue (b), or with its antiquark partner carrying the corresponding anti-colour charge \bar{r} . The reason for this confinement is believed to be the gluon–gluon self-interaction [15]: the gluon is not only the exchange particle of the strong force, it also carries colour charge, allowing it to strongly interact with the quarks as well as with itself (as opposed to the photon, which mediates the electromagnetic interaction, but does not carry any electric charge). Picturing the interaction between two quarks as the exchange of gluons, these gluons themselves interact with each other, resulting in an attractive force. If the two quarks were now separated, the potential would grow linearly with the distance of separation such that the energy in the gluon field would become huge. Therefore, quarks remain confined in colour neutral states.

If the quarks, however, are very close to each other (or the momentum transfer between them is very large), the strength of the strong interaction is weakened — a phenomenon which is known as asymptotic freedom. Consequently, in the limit of high temperatures and/or high baryon densities, quarks and gluons can move freely in a deconfined state of matter, the quark–gluon plasma [26]. It is thought to have existed a few microseconds after the Big Bang [19], when the temperature was much higher than today. Following the subsequent expansion of the Universe, the matter cooled down until, upon reaching a critical temperature T_c , it became confined into hadrons, eventually forming the matter around us. The nuclear matter as we know it is marked in the sketch of the QCD phase diagram in Fig. 2.2 at low temperatures and intermediate densities. Going to vanishing baryon chemical potential (that is, equal amounts of baryons and anti-baryons) and high temperatures — conditions which are fulfilled in heavy-ion collisions at the LHC — the same phase transition as in the early Universe between the confined hadronic matter and the QGP state is expected. The critical temperature of this phase transition can be obtained using lattice QCD calculations to be $T_c \approx 154 \text{ MeV}$ [27, 28]¹.

¹Here, the temperature is given in kT units, meaning that the temperature values (in Kelvin) are multiplied by the Boltzmann constant $k = 8.62 \times 10^{-5} \text{ eV K}^{-1}$ [23].

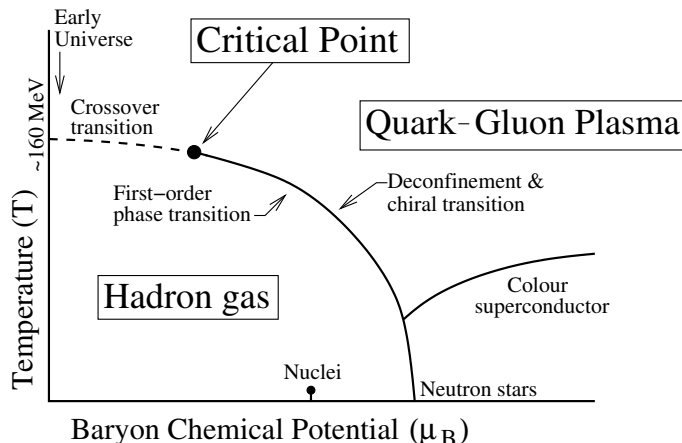


Figure 2.2: Sketch of the QCD phase diagram [29].

Already in the early 1980s, heavy-ion collisions were considered ideal to create a QGP, and to investigate its behaviour and properties at the phase transition. For this purpose, several facilities have been converted or newly constructed since the late '80s to suit a heavy-ion programme, the most recent being the Relativistic Heavy-Ion Collider (RHIC) at Brookhaven National Laboratory, New York, and the LHC at CERN, colliding gold and lead nuclei, respectively [19]. In the heavy-ion collisions at the LHC, it is possible to recreate the conditions shortly after the Big Bang in the laboratory, corresponding to the region at low μ_B and high T in Fig. 2.2. Consequently, the phase boundary between the hadronic state and the QGP can be investigated, for example to experimentally determine the critical temperature.

2.3 Probing the Quark–Gluon Plasma

Observing the QGP directly is not possible; instead, one must resort to indirect observations using signatures which indicate that indeed a QGP has been formed, or which can be used to measure its properties. There are many probes suitable to investigate the QGP (listed for example in [30]). Here, only a few examples, which involve electrons and are therefore of interest in the context of this thesis, are presented:

Direct photons are produced directly in a particle collision [30]. As opposed to decay photons, which originate from the decay of hadrons (which can only form below T_c), direct photons can be emitted at different stages on the way to a deconfined medium. Thus, they contain information about the history of the QGP and might provide experimental access to the initial QGP temperature. Since the photons only take part in the electromagnetic interaction, they remain undisturbed by the medium and carry information of their origin to the “outside” (i.e. to the experiment).

Dileptons (l^+l^- pairs), like the photons, can be emitted at different stages of the heavy-ion collision, where those with a high mass and transverse momentum are

produced early at high temperatures and those with lower mass and momentum later on at lower temperatures [30]. Again like the photons, they only interact electromagnetically and thus remain undisturbed by the strongly interacting medium around them, making them useful probes for the evolution of the QGP.

Quarkonia are bound states of heavy (charm or bottom) quark–antiquark pairs, for example the J/Ψ ($c\bar{c}$) or the Υ ($b\bar{b}$). They are created in the initial heavy-ion collision, and thus experience the formation of the QGP. Due to the high density of gluons in the QGP, the colour charge is screened, resulting in the “melting” of the quarkonia into the deconfined medium [26]. This suppression of the quarkonium states relative to their production rates without QGP should occur sequentially, with the strongly bound ground states (e.g. the $\Upsilon(1S)$) dissociating at higher temperatures of the QGP than the more loosely bound higher states. In this way, analysing the quarkonia spectra could provide an estimate for the temperature of the QGP. Indeed, a sequential suppression was first observed at the LHC for the $\Upsilon(1S)$, $\Upsilon(2S)$ and $\Upsilon(3S)$ states by the CMS experiment [31].

For the charmonia ($c\bar{c}$ pairs), the situation at the LHC is quite different: while a suppression is expected at low (RHIC) energies, at high energies like those at the LHC the number of produced charm quarks per collision is much higher, and the formation of new $c\bar{c}$ states during the hadronisation stage becomes therefore much more likely [19]. Thus, the J/Ψ production at the LHC is increased compared to the production at RHIC [32]. Studying the J/Ψ is therefore of particular interest, as it can provide important insights on the deconfinement of charm quarks as well as the mechanisms of charmonium production in the QGP.

The above examples of QGP signatures require clean electron identification (where from this point on, “electron” refers to both e^+ and e^-): quarkonia can decay via the dielectron channel, e.g. $J/\Psi \rightarrow e^+e^-$; photons can be converted to electrons via interaction with the detector material; and dileptons can be produced as e^+e^- pairs. In addition, a selection of events containing rare probes (e.g. the J/Ψ or the Υ) is necessary, as these are produced only in small amounts. Both the identification of electrons and the selection of rare probes (in the form of a contribution to the ALICE trigger system) can be provided by the TRD, which is integrated in the ALICE detector setup, as described in the following chapter.

Chapter 3

ALICE at the LHC

In 1952, the *Conseil Européen pour la Recherche Nucléaire (CERN)* [18], or European Council for Nuclear Research, was founded with the purpose of building a new laboratory for the research of fundamental physics in Europe. Two years later, the European Organisation for Nuclear Research was established, the original council was dissolved (although the acronym CERN was kept) and building started on the selected site near Geneva in Switzerland, close to the French border.

Over the years, several accelerator complexes have been built at CERN, with the latest instalment being the Large Hadron Collider, currently the world's largest particle accelerator [18]. The collisions of protons and lead nuclei in the LHC are detected by several experiments, which are installed around the accelerator ring. The LHC with its injection chain and the four major LHC experiments will be described briefly in the first section of this chapter, while the later sections will focus on ALICE, the experiment specialised on the study of heavy-ion collisions and the quark–gluon plasma. Included in the overview of ALICE is a first description of the TRD, which will be the main subject of the next chapter.

3.1 The Large Hadron Collider

The Large Hadron Collider is a two-ring hadron accelerator, installed between the Jura mountains and Lake Geneva in the 26.7 km tunnel that was originally built for its predecessor, the Large Electron-Positron collider (LEP) [33]. However, in contrast to LEP, which was limited in the achievable collision energy by synchrotron radiation, the LHC is designed to reach much higher energies, namely a centre-of-mass energy of $\sqrt{s} = 14$ TeV for proton-proton collisions as well as a centre-of-mass energy of $\sqrt{s_{NN}} = 5.023$ TeV per nucleon-nucleon pair in collisions of lead ions. Here, the limiting factor is not the synchrotron radiation, but the strength of the magnetic field: keeping a beam of 7 TeV protons in a circle of ~ 27 km circumference requires a field of 8.33 T, which can only be achieved using superconducting magnets. Therefore, 1232 dipole magnets are installed in the whole LHC, which are cooled down to 1.9 K using superfluid helium.

Like the LEP before it, the LHC makes use of the already existing accelerator complex at CERN, as shown in Fig. 3.1. Protons are first accelerated in the linear accelerator Linac 2 before subsequently entering the Proton Synchrotron Booster

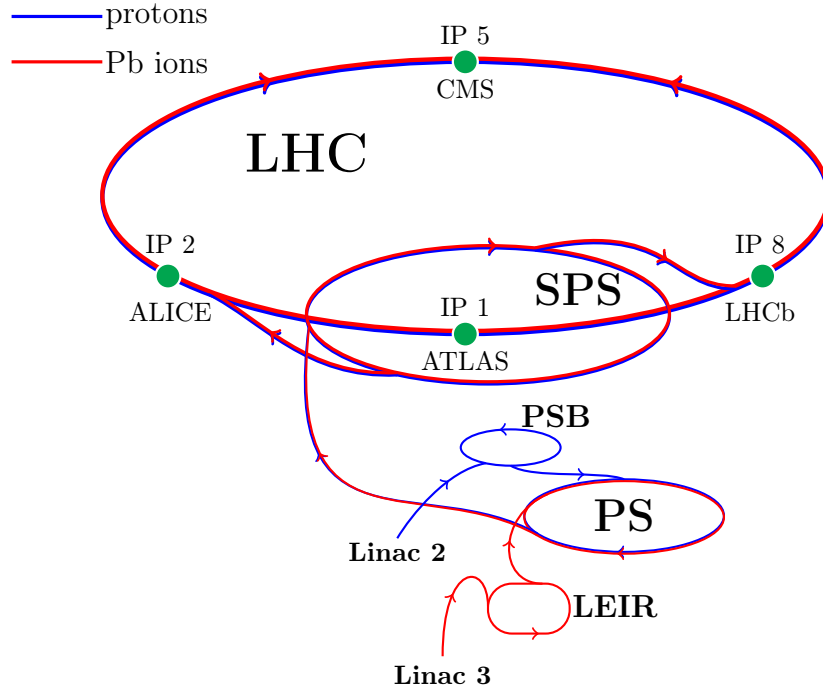


Figure 3.1: LHC injection chain (figure based on [35]). Protons (blue) and Pb ions (red) are accelerated in the different stages of the accelerator complex before entering the LHC. Within the LHC, the beams are brought to collision at four interaction points, where the four major experiments ATLAS, ALICE, CMS, and LHCb are installed.

(PSB), the Proton Synchrotron (PS), and the Super Proton Synchrotron (SPS). Once the beams have reached an energy of 450 GeV, they are finally injected into the LHC. The Pb ions, on the other hand, start out at the Linac 3 and are then accelerated in the Low Energy Ion Ring (LEIR), before taking the same route as the protons through PS and SPS into the LHC. Using this injection chain, it is not only possible to collide protons with protons and lead ions with lead ions, but also to have “mixed” collisions, i.e. colliding protons with lead ions. This is done in the LHC since 2012 [34].

There are four Interaction Points (IPs) where the two beams collide. At these IPs, the four major LHC experiments are installed, as shown in Fig. 3.1. They will be briefly introduced below:

ATLAS [36]: A Toroidal LHC ApparatuS (ATLAS) is a general purpose experiment located at IP 1, built with the aim to test predictions of the Standard Model and to investigate new physics like supersymmetry, extra dimensions, or dark matter candidates. The superconducting magnet system of ATLAS combines a solenoid surrounding the inner detector with a large toroidal barrel and two toroids as end-caps. Semiconductor pixel and strip detectors form the inner tracking system within the solenoid, which is encased by electromagnetic and hadronic calorimeters. A large

muon system with three layers of high precision tracking chambers surrounds the calorimeters.

CMS [37]: Like ATLAS, the Compact Muon Solenoid (CMS) experiment, installed at IP 5, is a multi-purpose detector. While CMS and ATLAS have similar scientific goals, they differ in the design of their magnet systems and in the applied detector technologies. CMS is constructed around a superconducting solenoid magnet, which is large enough to house the silicon tracker and the electromagnetic and hadronic calorimeters inside its coil. In the return yoke of the magnet, the muon chambers are placed, consisting of drift tubes in the barrel, cathode strip chambers in the end caps, and resistive plate chambers in both.

In 2012, the Higgs boson was discovered at both CMS and ATLAS [16, 17], thus providing the last missing experimental proof to complete the Standard Model.

LHCb [38]: The Large Hadron Collider beauty (LHCb) experiment is specialised in heavy flavour physics, in particular in b quarks, with the goal to study rare decays and to search for CP violation beyond the Standard Model. As b - and \bar{b} -hadrons are mainly produced in forward and backward direction at LHC energies, the detector at IP 8 is constructed as a single-arm forward spectrometer (instead of symmetrically surrounding the interaction point like ATLAS and CMS). Close to the collision point of the beams, precise measurements of the tracking coordinates with the silicon-based vertex locator allow for the reconstruction of secondary vertices. Following the vertex locator, further tracking chambers using silicon microstrip and straw-tube technology are installed in front of and behind a warm dipole magnet. Particle identification is provided by ring-imaging Cherenkov detectors, calorimeters, and a muon system.

ALICE [39]: ALICE at IP 2 is the dedicated heavy-ion experiment at the LHC and will be explained in detail in the following section.

3.2 A Large Ion Collider Experiment

The main goal of A Large Ion Collider Experiment (ALICE) is to study the deconfined state of strongly interacting matter known as the QGP, which is created in high-energy heavy-ion collisions [27, 28]. This results in different challenges, compared to the other LHC experiments, for ALICE to cope with: extremely high densities of charged particles in heavy-ion collisions complicate the reconstruction of all tracks; a large range for momentum measurements is necessary, covering low transverse momenta (p_{\perp}) of ~ 100 MeV/ c as well as high $p_{\perp} \geq 100$ GeV/ c ; the experiment must be able to provide global event characteristics (e.g. information on the centrality of the collisions, or on the event plane); and particle identification (PID) is crucial to reconstruct the decay products of many probes of interest [21, 39].

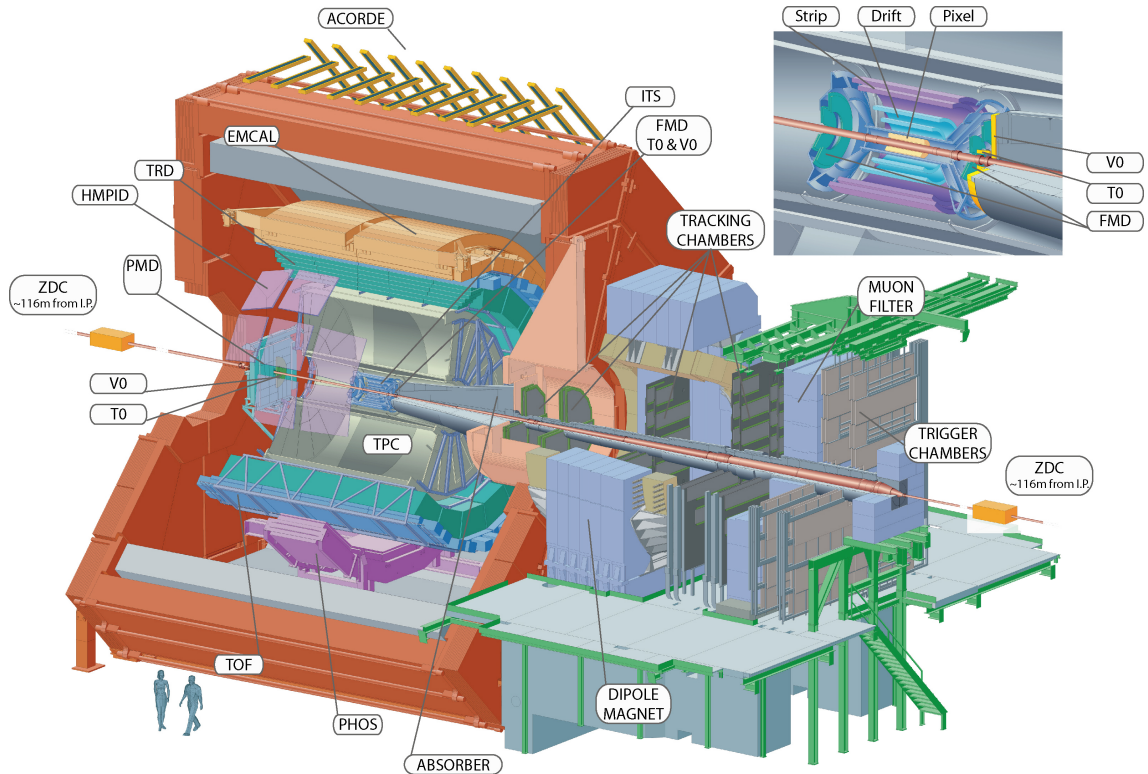


Figure 3.2: Sketch of the ALICE detector system [40]. The large solenoid magnet houses the central barrel detectors at mid-rapidity. In forward direction, the muon system is installed.

To fulfil these requirements, ALICE comprises a number of detector systems, which are shown in Fig. 3.2. The central barrel detectors are installed at mid-rapidity around the nominal collision point, inside the solenoid magnet inherited from the L3 experiment, which was installed at LEP. Four of the detectors in the central barrel — ITS, TPC, TRD, and TOF — cover the full azimuth. They are responsible for vertex determination, tracking, and particle identification, and will be introduced in more detail in Section 3.2.2. Two calorimeters (EMCal and PHOS) provide additional PID, while centrality, multiplicity, event plane, and other event characteristics are determined by a number of specialised detectors (e.g. V0, and T0). Finally, outside of the magnet, a dedicated muon system, consisting of a warm dipole magnet and several tracking stations, is installed at forward rapidity.

3.2.1 Global coordinate system

To ease further descriptions of detector positions and ranges within the experiment, the global coordinate system [41] used in ALICE is briefly described. It is a right-handed Cartesian system with the origin placed at the interaction point, as shown in Fig. 3.3. The x and y axes are perpendicular to the beam direction, with the x axis pointing inward to the centre of the LHC, while the y axis points upward. The

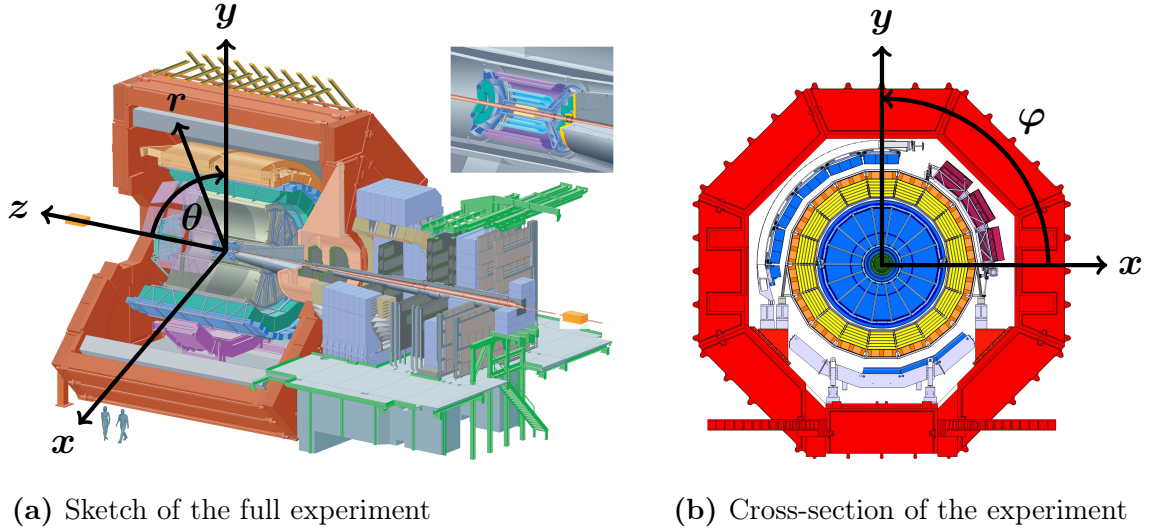


Figure 3.3: ALICE global coordinate system [41] (figures adapted from [40]). The right-handed Cartesian system is shown in (a). Instead of the Cartesian coordinates, spherical coordinates can be used as well, which are sketched in (a) and (b).

z axis follows the beam direction, with the positive z direction defined as pointing *away* from the muon arm.

Instead of the Cartesian system, spherical coordinates can be used as well. The radius r is defined as $\sqrt{x^2 + y^2 + z^2}$, starting at the origin and pointing out of the experiment. The polar angle θ is given as the angle between the z axis and the xy plane, with $\theta = 0$ at $z > 0$ and $\theta = \pi/2$ at $z = 0$, as shown in Fig. 3.3a. Finally, the azimuthal angle φ is defined as the angle in the transverse plane, see Fig. 3.3b. Standing at positive z and looking in the direction of the muon arm, it increases counter-clockwise from $\varphi(x) = 0$ to $\varphi(y) = \pi/2$.

3.2.2 Central barrel detectors

Within the central barrel, inside the longitudinal 0.5 T field provided by the solenoid magnet, the Inner Tracking System (ITS), the Time Projection Chamber (TPC), the Transition Radiation Detector (TRD), and the Time-Of-Flight (TOF) detector are installed (sorted by increasing radius). They cover the full azimuth with an 18-fold (20°) segmentation, as well as nearly two units in pseudorapidity ($|\eta| \lesssim 0.9$). A brief description of the main purpose of the detectors and the technologies in use is given below [21, 34, 39]:

ITS: Situated close to the collision point of the beams, the ITS consists of six layers of silicon-based detectors – two Silicon Pixel Detectors (SPD), two Silicon Drift Detectors (SDD), and two Silicon Strip Detectors (SSD). These detectors, which are shown in the inlay of Fig. 3.2, provide information on the primary vertex, as well as on secondary vertices, with high resolution. In addition, the ITS is used to track

and identify low-momentum particles, and to improve the TPC tracking resolution of high- p_{\perp} particles.

TPC: The main tracking detector of ALICE is the TPC, located between $r = 0.85$ m and $r = 2.47$ m. The gas-filled drift volume of about 90 m^3 is divided into two halves by a central electrode generating a drift voltage of 100 kV between the centre and the end plates, which are equipped with multi-wire proportional chambers for read-out. While the resulting drift time of the order of $100\text{ }\mu\text{s}$ is rather long, using the TPC technology ensures reliable tracking even at most central Pb–Pb collisions, where more than 20 000 charged particles are produced [42]. Additionally to its tracking capabilities, the TPC can be used to identify particles via the measurement of their specific energy loss dE/dx .

TRD: The TRD is specialised in electron identification by measuring the specific energy loss as well as transition radiation. In addition, it also contributes to the tracking of charged particles, and provides a trigger contribution for the ALICE trigger system. A detailed description of the layout and the principle of operation of the TRD will be given in Chapter 4.

TOF: The TRD is followed by the TOF detector, which provides particle identification at intermediate momenta using time-of-flight measurements. Built as a large array of multigap resistive plate chambers, the TOF detector achieves a timing resolution better than 100 ps , allowing for good π/K separation (up to $2.5\text{ GeV}/c$) and p/K separation (up to $4\text{ GeV}/c$).

3.3 Data processing

Once collisions have taken place, the measurements taken by ALICE are read out. In RUN 1 and RUN 2, a triggered read-out scheme is used, which consists of three stages of hardware triggers — called level-0, level-1, and level-2 — and a software stage, the so-called High-Level Trigger (HLT) [34]. Fast detectors, like V0, T0, or the SPD, provide the contribution to the level-0 trigger decision, about $1.2\text{ }\mu\text{s}$ after the interaction has occurred. Detectors which are not available within this time frame (for example the TRD) are used for the level-1 trigger decision, which must be made after $\sim 7.7\text{ }\mu\text{s}$ with respect to the collision [43]. The timing of the level-2 trigger is determined by the drift time of the TPC, about $100\text{ }\mu\text{s}$ after the interaction.

All trigger decisions are managed by the Central Trigger Processor (CTP), which receives the input for each trigger level provided by the corresponding trigger detectors. If the conditions for a trigger level are fulfilled, the trigger is accepted and sent to all detectors to initiate the next trigger stage; otherwise, the trigger is rejected and data taking is aborted. If all three hardware trigger stages are accepted, the detectors send their data to the Data Acquisition (DAQ). In addition, a copy is sent to the HLT, where the data are compressed, and events can be reconstructed and fil-

tered. This allows a further reduction of the data size before it is recorded and stored.

The stored data — also referred to as *raw data* — need to be processed offline to obtain actual physics results. The means for this processing, which consists of data reconstruction and subsequent analysis, are provided by the AliRoot framework [44]. AliRoot is based on the object-oriented scientific software framework ROOT [45], but has been specialised to accommodate for example the ALICE-specific detector geometries.

In addition to processing raw data, it is also possible to simulate collisions and detector responses in AliRoot using Monte Carlo (MC) event generators. The output of these simulations can then be reconstructed and analysed analogously to the raw data, as depicted in Fig. 3.4 [43]. During collisions, raw data are collected by the experiment. They can be transformed into digitised detector responses, the so-called digits, which can be used for quality assurance and debugging purposes. On the other hand, collision events can be produced by a MC event generator, which allows the calculation of digits by simulating the detector responses. These digits can also be transformed into raw data, providing an input for the reconstruction which is as close to the real data as possible.

The reconstruction, which can use both digits and raw data as input, can therefore run on simulated as well as on real data. In this way, MC simulations allow the generation of data as close as possible to the actual measurements. This can be exploited to evaluate and tune the analysis, as MC simulations provide information on the true properties of the particles — the so-called *Monte Carlo truth* — which can be directly compared to the detector response (as will be done in Chapter 6).

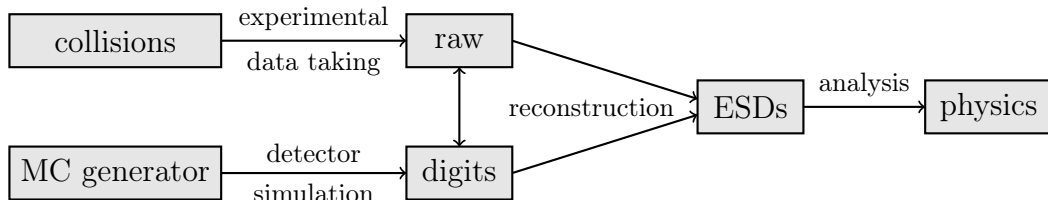


Figure 3.4: Overview of the tracking simulation (figure based on [43]). Raw data taken in collisions by the experiment, or digits obtained from MC simulations, can be used as input for the reconstruction, which yields for example particle tracks and PID. This information is stored in ESD files, which can be used as input for physics analyses.

To properly reproduce the detector response in simulations as well as for correct reconstruction, a number of detector-specific parameters must be known. This could be e.g. the configuration of the detector in question, the status of the read-out electronics, the gas composition, or temperature and pressure at the time of data taking. All of these values are saved during detector operation to ROOT files and stored in the Offline Condition DataBase (OCDB) [46]. If the raw data of a certain

period is reconstructed, or a simulation for the period in question is made, the corresponding OCDB entries will be called up and the relevant parameters can be extracted again.

At the end of the reconstruction step, the output — e.g. information on particle identification and track parameters — is written to Event Summary Data (ESD) files, which can subsequently be used as input for physics analyses. These can be implemented in the form of so-called *analysis tasks* based on the AliRoot class `AliAnalysisTask`, which allows the user to define a personal C++ class integrated in the AliRoot framework. Analysis tasks can be added to an analysis train, which loops over all events of the input data. In this way, the user can access the content in the ESD files event by event and e.g. select a sample of tracks that fulfils given filtering criteria to extract the physics information of interest.

Chapter 4

The Transition Radiation Detector

Electron identification in ALICE is crucial to measure a variety of QGP probes, including decays of quarkonia (e.g. the J/Ψ meson), photons, or dileptons. For electrons with a momentum of up to $1\text{ GeV}/c$, this can be done with the TPC via the measurement of the specific energy loss by ionisation dE/dx , as described by the Bethe–Bloch formula [15]. For higher momenta, however, the mass dependence of the energy loss weakens, making it increasingly difficult to distinguish electrons from pions, which are highly abundant in hadron collisions. To complement the PID capability of the TPC, a Transition Radiation Detector (TRD) was proposed to provide electron identification for momenta above $1\text{ GeV}/c$ by measuring the specific ionisation energy loss as well as Transition Radiation (TR). Transition radiation, predicted by V. Ginzburg and I. Frank in 1946 [47], is a form of electromagnetic radiation which occurs when a charged particle traverses the boundary surface between two media with different dielectric constants. As it only becomes relevant for highly relativistic particles with a Lorentz factor $\gamma = E/mc^2 \gtrsim 1000$, it is well-suited to discriminate between electrons and pions in a momentum range of a few GeV/c , where electrons will emit TR while pions will not [39].

In addition to the identification of electrons, the TRD can also be used for triggering to enhance rare probes — an essential part in the data taking with ALICE in RUN 1 and RUN 2. Furthermore, it provides a significant contribution to the tracking in the central barrel, increasing the momentum resolution for high- p_{\perp} particles by almost a factor of 2 [46].

To effectively measure the produced TR for particle identification and triggering, the TRD is built in a specialised way, which is explained in this chapter. Furthermore, a large part of the chapter focuses on the principle of operation of the TRD, and in particular its operation in RUN 1 and RUN 2, to pave the way for understanding what will change in RUN 3, which is explained in Chapter 5.

4.1 Detector overview

4.1.1 TRD structure

The TRD is one of the central barrel detectors within the solenoid magnet of ALICE, as shown in Fig. 3.2. It is built around the TPC at a radial distance of 2.90 m to 3.68 m relative to the beam axis and covers the full azimuth φ as well as a range in

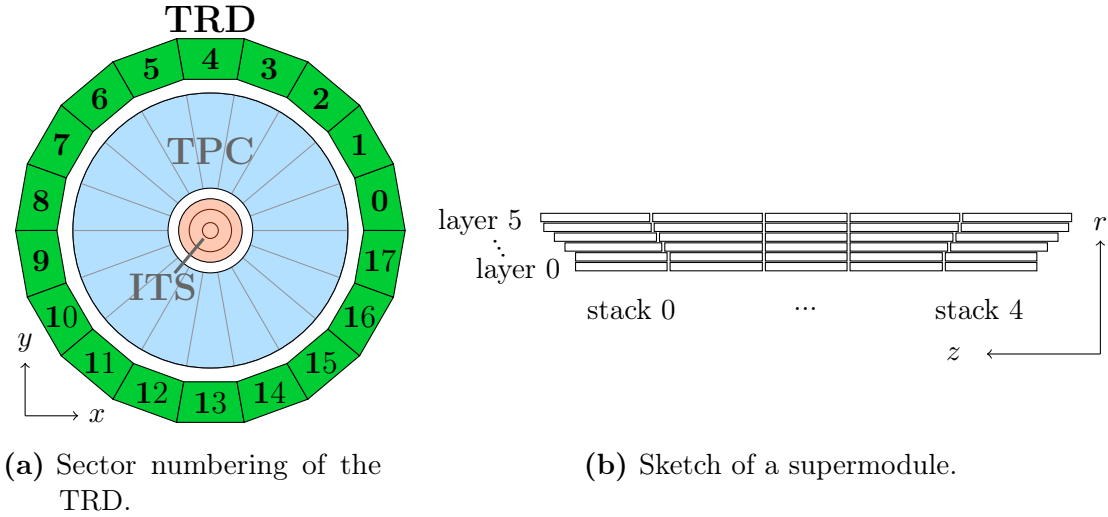


Figure 4.1: Sketch of the TRD structure. The TRD, located on the outer edge of the TPC, is segmented in azimuthal direction into 18 sectors. The sector numbering, shown in (a), starts with sector 0 at $\varphi = 0$ and continues counter-clockwise. Each sector, or supermodule, is divided into five stacks and six layers, as shown in (b).

pseudo-rapidity of $-0.84 \leq \eta \leq 0.84$ [46]. To match the TPC, the TRD is segmented 18-fold in φ direction into so-called sectors. In each sector, 30 detector modules, the Read-Out Chambers (ROCs), are arranged in five stacks (in z direction) of six layers (in r direction) inside a mechanical casing, the so-called supermodule. As a result, the TRD can host a total of 540 chambers of manageable size. However, the central stack of supermodules 13, 14, and 15 is empty to minimise the material budget in front of the PHOS detector, which is installed behind the TRD (cf. Fig 3.2).

In the global coordinate system of ALICE, the numbering of the 18 sectors starts with sector 0 at $\varphi = 0$, and increases counter-clockwise in azimuthal direction, as shown in Fig. 4.1a. Of the five stacks along the beam axis, stack 0 is located at positive z , farthest away from the muon arm, while stack 4 is closest to the muon arm at negative z . The layer numbering, finally, increases with the radius, meaning that layer 0 is closest to, and layer 5 farthest from, the beam pipe, as shown in Fig. 4.1b.

4.1.2 Local coordinate system

To ease the following descriptions of the read-out chamber design and the principle of operation, it is useful to introduce the local coordinate system used for the TRD [22]. It is a right-handed orthogonal Cartesian system, shown in Fig. 4.2, which has its origin — just like the global coordinate system — at the interaction point of the beams. The z axes of the global and local coordinate systems coincide as well,

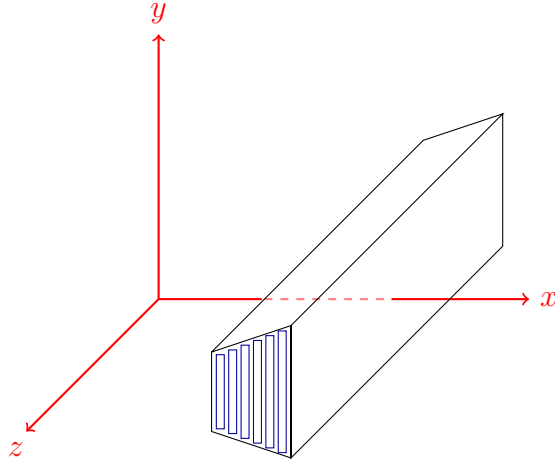


Figure 4.2: The local coordinate system used for the TRD (figure based on [48]). The origin of the right-handed Cartesian system lies at the collision point. The x axis points outwards and perpendicularly intersects the read-out chambers, while the y axis specifies the distance from the chamber centre. The z axis runs parallel to the beam direction.

running parallel to the beam line, with positive direction being defined as pointing away from the muon arm. The local x axis is defined perpendicular to the chambers, pointing outward from the origin and intersecting the supermodule in the range of $290 \text{ cm} \lesssim x \lesssim 370 \text{ cm}$. The local y axis, finally, specifies the distance relative to the centre of a chamber.

The size of the ROCs within one supermodule changes both in the local x and z direction, given the supermodules their trapezoidal shape. With increasing x , the width of the chamber increases as well, resulting in a minimal range of $-45 \text{ cm} \leq y \leq 45 \text{ cm}$ for layer 0 to a maximal range of $-56.5 \text{ cm} \leq y \leq 56.5 \text{ cm}$ for layer 5 [46]. Additionally, the chamber size changes in longitudinal direction, with the chambers in stack 2 being the smallest and the length increasing for large z and radii (as indicated in Fig. 4.1b).

From this point on, all coordinates are in principle given in the local coordinate system of the TRD. If a description in the global coordinate system of ALICE is necessary, it will be indicated accordingly.

4.2 Chamber layout and principle of operation

The basis of particle detection and identification with the TRD is measuring the specific ionisation energy loss of a particle as well as possible transition radiation. Each read-out chamber of the TRD therefore consists of a radiator of 4.8 cm thickness, a 3 cm drift region, and an amplification region in the form of a Multi-Wire Proportional Chamber (MWPC), as sketched in Fig. 4.3.

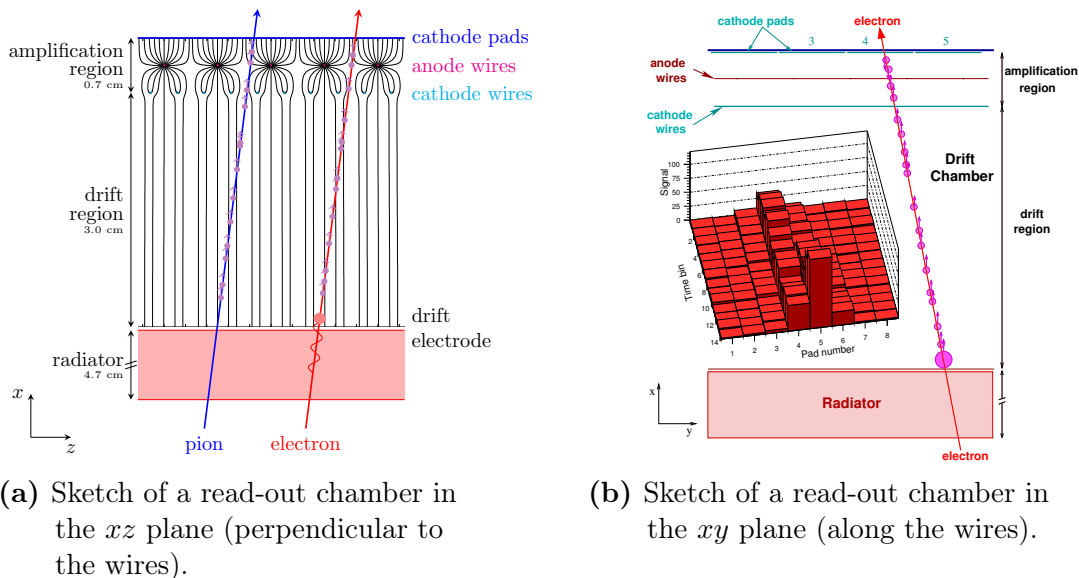


Figure 4.3: Sketch of a TRD read-out chamber to illustrate the principle of operation [22, 46]. (a) A pion track (in blue) and an electron track (in red) illustrate the specific energy loss due to gas ionisation. In addition, the transition radiation caused by the electron is drawn as a large red circle at the entrance of the chamber. (b) The absorption of the TR photons close to the chamber entrance is visible in the temporal evolution of the signal, shown in the inset.

In the following paragraphs, the properties and functions of the different chamber components will be described briefly. If not indicated otherwise, all information is taken from [46].

Radiator and TR production

A particle traversing the TRD will first pass through the radiator where it may cause transition radiation, shown in Fig. 4.3a for an electron (in red). As the probability of TR production for one boundary crossing is only of the order of the electromagnetic coupling constant $\alpha \approx 1/137$, a large number of boundaries are necessary to achieve a non-negligible TR yield. Accordingly, the radiators in the TRD are built as fibre/foam sandwich structures, which produce a sufficient amount of transition radiation while at the same time provide the mechanical stability needed for the chambers.

Drift region

Both the TR photons, which are typically produced at an energy of a few keV [46] when crossing the boundaries in the radiator, and the particle itself have to be detected in the chamber. The drift and amplification regions are therefore filled with a xenon-based gas mixture. In Xe, the absorption length of a 10 keV photon is ~ 1 cm, meaning that the photons are most likely absorbed in the beginning of the drift region. The charged particle, on the other hand, will uniformly ionise the gas during its passage through the drift and amplification regions. Thus, particles which

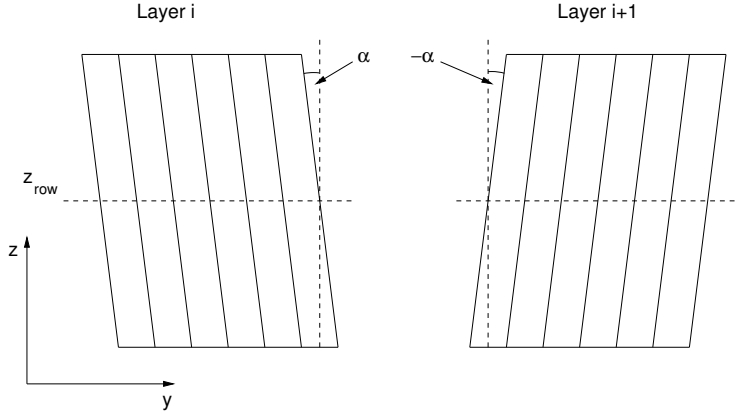


Figure 4.4: Tilting of the pads on the cathode pad plane for two consecutive layers [22]. The tilting by $\pm 2^\circ$ improves the z resolution during track reconstruction.

produce TR can be separated from those which do not by measuring the temporal evolution of the signal, as indicated in the inlay in Fig. 4.3b.

Amplification region and signal generation

Due to the uniform electric field between the drift electrode (top of the radiator) and the cathode wires, the electrons produced by the absorption of the TR photons and by the ionisation process drift towards the anode wires in the amplification region. The electric field increases in the close vicinity of the wires, thus accelerating the electrons and causing the formation of an avalanche to amplify the original signal. As a quenching gas, CO_2 is chosen, with the final gas mixture amounting to 85% Xe and 15% CO_2 .

While the electrons from the avalanche are collected at the anode wires, the positive ions drift back to the cathode wires. This movement of charged particles induces a signal on the cathode pad plane, which is read out and processed by the read-out electronics. The pad plane is segmented into 144 columns in y direction and 16 rows in z direction (12 rows for stack 2). The resulting pad width in one row — between ~ 0.65 cm and ~ 0.8 cm, depending on the layer — is small, such that the signal is induced on several (typically three) adjacent pads in y direction. This charge sharing allows for a position reconstruction in the bending plane with a spatial resolution $\lesssim 400 \mu\text{m}$ [49], which makes the TRD a useful extension of the lever arm to improve the p_\perp resolution. In z direction, on the other hand, the granularity is not as high, with pad lengths ranging between ~ 7.5 cm and ~ 9 cm. However, this is still sufficient for the track matching with the inner detectors. Furthermore, the pads are slightly tilted by $\pm 2^\circ$, with the sign alternating for neighbouring layers, as indicated in Fig. 4.4. By combining consecutive layers during track reconstruction a more precise determination of the z position of the track is thus possible.

The pads on the pad plane are connected via short cables to the read-out electronics installed on the back of the read-out chamber, which handle the signal processing

and read-out. Figure 4.5 shows the average signal on the pads — after amplification and sampling in time bins of 100 ns by the electronics — for pions (in blue), electrons without TR (in green), and electrons with TR (in red) with a momentum of $2 \text{ GeV}/c$. All three curves exhibit a peak at early drift times (around $0.5 \mu\text{s}$) corresponding to the amplification region, where ionisation from both sides of the anode wires contributes within the same time bins to the signal. The time evolution of the average signal remains similar for both pions and electrons without TR, with both the green and the blue curve showing a plateau caused by the electrons from the drift region. However, in this momentum region the deposited charge is larger for electrons than for pions due to the relativistic rise of the specific energy loss. If there is transition radiation in addition, a clear TR peak is visible at later times, that is in close vicinity of the chamber entrance. Hence, electrons deposit on average more charge than pions in the TRD, both by energy loss due to ionisation (in this momentum region) and TR production. The signal in a single chamber, however, can of course fluctuate with respect to the average pulse height shown in Fig. 4.5, making it more difficult to distinguish electrons from pions by simply determining the amount of deposited charge. Therefore, the measurement of the temporal signal evolution to differentiate between specific energy loss and a possible transition radiation contribution is an important tool to improve e/π separation.

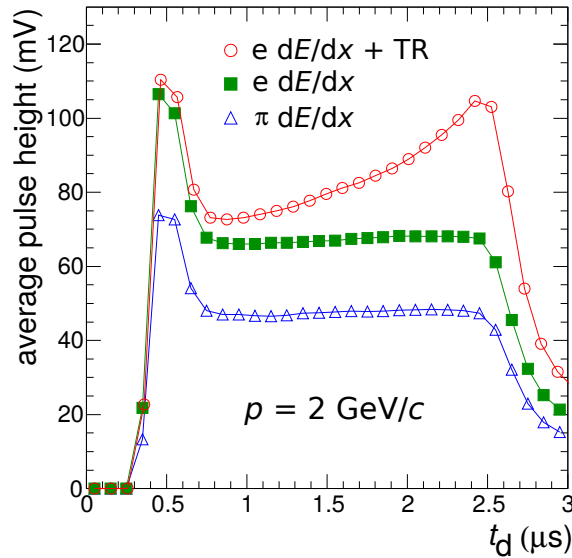


Figure 4.5: Average pulse height as a function of the drift time for electrons (with and without TR) and pions with $p = 2 \text{ GeV}/c$ [50]. The transition radiation is visible in the red curve as an increase in pulse height in late time bins, i.e. close to the chamber entrance.

4.3 Signal processing and read-out

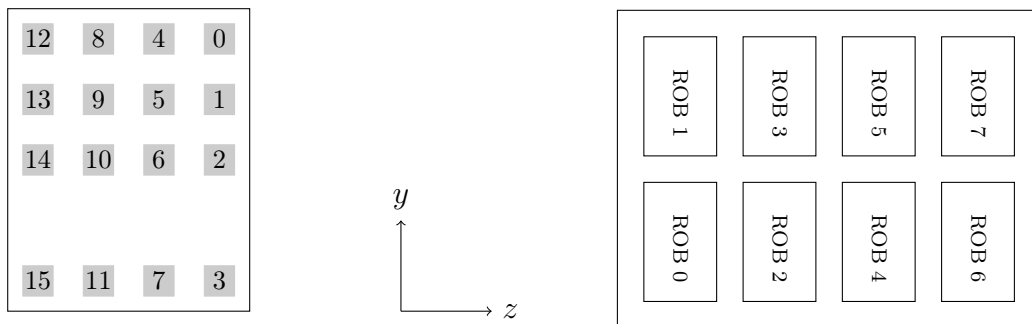
Handling the data taken by the TRD is the task of the front-end electronics, directly mounted on the back of the ROCs, and the global tracking unit [46]. They constitute the read-out and processing chain, which starts with the signal arriving at the pad plane, and ends with the transfer of event data to the DAQ system. During this process, the data are transmitted in two parallel computation steps: via the trigger path, which is optimised for speed, data are processed online to arrive at a fast trigger decision; while via the raw data path, minimally processed data are buffered until a trigger decision is made, and subsequently read out to be used in the offline reconstruction and analysis.

The timing of processing and data transfer of both front-end electronics and global tracking unit is steered by the three hardware stages of the ALICE trigger system (see Section 3.3). The TRD contributes to the decision of the middle stage, the level-1 trigger.

4.3.1 The front-end electronics

Processing the signals which arrive on the pad plane is the task of the Front-End Electronics (FEE). As well as being part of the read-out chain for the raw data, the FEE is also jointly responsible for the TRD trigger contribution to the ALICE triggering scheme, which requires a fast trigger decision for the level-1 trigger (within a few μs). To meet these demands, the FEE consists of Multi-Chip Modules (MCMs) designed for a highly parallelised processing and read-out. Each MCM is composed of two ASICs — a PreAmplifier-ShAper (PASA) and a TRAcklet Processor (TRAP) — which allow the customisation of the signal processing depending on the detector configuration [43].

The charge induced on the pad plane is transferred to the FEE via flexible flat cables. The signals of 18 pads are amplified by the charge-sensitive PASA on one MCM before being transferred to the TRAP on the same chip. The custom-designed TRAP contains in total 21 Analog-to-Digital Converter (ADC) channels, a chain of filters, a hardware pre-processor, four CPUs, and is equipped with ~ 400 registers to store configuration settings. In addition to the 18 ADC channels fed by the PASA on the same MCM, three excess channels receive the output of the PASAs on the neighbouring MCMs. After the digitisation of the analogue signal in the ADCs, the data are subjected to a configurable filter chain. In the pedestal filter, channel-by-channel variations of the baseline are corrected. Following the pedestal filter, a gain filter is used to compensate differences in the local gain within the chamber. The gain corrections, which are obtained in special calibration runs using krypton decays [51], are necessary to correctly measure the specific energy loss, and thus are important for the online PID needed for triggering (see Section 4.4.1). The third filter in the chain, the tail cancellation filter, can be used to reduce the ion tails of the signals induced on the pad plane, which deteriorate the angular



(a) Overview of the MCMs on one ROB. (b) Overview of the ROBs on one ROC.

Figure 4.6: Top-down view of a read-out board (a) and a read-out chamber (b), based on [43].

resolution. However, as the tail cancellation filter cuts away parts of the signal and thus deteriorates the online PID, it is not used in the FEE in RUN 1 and RUN 2.

At this stage, the processing and read-out chain is split up into the raw data and the triggering path: on the one hand, the data are stored in the event buffers until a trigger command arrives which initiates the read-out. On the other hand, they are sent to the pre-processor, where online clusters are calculated from the filtered signal. These clusters can then be further processed in the CPUs to calculate the contribution to the trigger decision. The online cluster finding algorithm and processing in the CPUs are described in more detail in Section 4.4.1.

The MCMs are mounted in groups of 16 on the ROBs, with one MCM connected to 18 read-out pads within one row [43]. Eight ROBs are installed on one chamber (six on chambers in stack 2), as sketched in Fig. 4.6. One Detector Control System (DCS) board per chamber, which is accessible via Ethernet connection, is used for monitoring and to distribute the FEE configuration to the MCMs.

Depending on the decision of the triggers, first the processed data from the CPUs, and later the raw data from the event buffers are sent for further processing and read-out to the global tracking unit.

4.3.2 The global tracking unit

In the Global Tracking Unit (GTU), the tracklets processed in the CPUs of the FEE are stack-wise combined in the so-called Track Matching Units (TMUs) to form tracks, for which the transverse momentum and the PID can be calculated to provide the level-1 trigger contribution of the TRD [46]. In addition, the raw data of up to four events can be stored in parallel in event buffers. The information from the five TMUs per supermodule are sent to a SuperModule Unit (SMU), controlled again by a DCS board, for a trigger decision to be made. In addition, after receiving the level-2 trigger accept, the SMU builds the corresponding event by combining the

event data stored in the buffers with tracking and triggering information, and sends it to the DAQ [46].

4.4 Operation in RUN 1 and RUN 2

4.4.1 Triggering and raw data transfer

In RUN 1 and RUN 2, one of the purposes of the TRD is to provide trigger signals on electrons and jets for the level-1 stage, $\sim 7.7 \mu\text{s}$ after the collision occurred [46]. The calculation of the trigger contribution is split into two parts: during the local online tracking in the FEE, the charge collected on the pad plane is digitised, filtered, and clusterised [43]. A subsequent straight-line fit of the position of the online clusters results in a segment of the track in the given chamber, the so-called *tracklet*. In addition to the information on position and incident angle resulting from the fit, the deposited charge of the clusters is translated into a PID value via a transformation function, which is stored in the form of a Look-Up Table (LUT) in the TRAP.

In the second part — the global online tracking — tracklets within one stack are combined to yield a track, whose p_{\perp} can be calculated. Additionally using the PID information gained from the charge deposit of the clusters, the TRD can make a decision on whether the track belonged to a particle of interest (e.g. an electron) with a transverse momentum of interest (e.g. $\geq 2 \text{ GeV}/c$).

Local online tracking and tracklet calculation

After the digitisation and filtering of the signal in the FEE, the data are sent to the hardware pre-processor, which searches time bin-wise for clusters. Two conditions must be fulfilled by the accumulated charge to be identified as a cluster [43]: firstly, the charge of three neighbouring channels must exceed a given (configurable) threshold Q_{thr} , and secondly, the middle channel must be a local maximum:

- 1) $Q_{i-1} + Q_i + Q_{i+1} \geq Q_{\text{thr}}$
- 2) $Q_i \geq Q_{i-1}$ and $Q_i > Q_{i+1}$

For up to six clusters per time bin and MCM, the transverse position y is calculated as the centre-of-gravity of the charge in three neighbouring channels which belong to the cluster in question. The transverse position is needed in the next step, in which fit sums are calculated for each channel. Based on these sums, straight-line fits of the clusters will be performed in the CPUs that are part of the TRAP. However, as there are only four CPUs, only up to four channels can be further processed. Therefore, two conditions on the number of clusters are introduced:

- 1) $N_i \geq N_{\text{CL}}^{\text{thr}}$
- 2) $N_i + N_{i+1} \geq N_{\text{CT}}^{\text{thr}}$

Here, N_i is the number of clusters found in channel i , while N_{i+1} is the number of clusters in the adjacent channel $i + 1$. The threshold values $N_{\text{CL}}^{\text{thr}}$ and $N_{\text{CT}}^{\text{thr}}$ can be set in the TRAP. If the conditions are met by a pair of channels i and $i + 1$, it is considered a tracklet candidate, and the fit sums are forwarded to one of the CPUs for the calculation of the linear fit, which is parametrised as

$$y(t) = y + b \cdot t,$$

with the transverse position y (relative to the chamber centre), and the slope b . However, instead of the slope, the deflection d_y over the drift length l_{drift} is used to describe the tracklet (see Fig. 4.7). It can be derived by multiplying the slope (given in units of pads per time bin) with the pad width w_{pad} and the number of time bins n_{drift} ,

$$d_y = b \cdot w_{\text{pad}} \cdot n_{\text{drift}}, \quad n_{\text{drift}} = \frac{l_{\text{drift}}}{v_{\text{drift}}},$$

where v_{drift} is the drift velocity in the chamber.

The deflection d_y and the transverse offset y (given at the radial position corresponding to time bin 0, which is at a slightly larger radius than the anode wire plane) are sketched in Fig. 4.7. Together with the z position derived from the pad row of the MCM, and the PID value, which is obtained from the LUT based on the accumulated charge in the two channels, they constitute the parameters for the full tracklet description. They are stored in a 32-bit word — the so-called *tracklet word* — which is then sent to the GTU for the global online tracking.

Global online tracking

During the first stage of the global online tracking in the GTU, the tracklets previously calculated in the FEE are first stack-wise matched into groups considered to belong to the same track. For this purpose, the tracklets are first pre-selected based on whether their positions are consistent with a primary track in the xz plane. A subsequent projection onto a virtual yz plane in the middle of a stack allows a further selection of those tracklets which are close together on this plane. If tracklets in at least four layers are found which are considered to originate from the same track, the online track is calculated. Only one tracklet per layer can contribute to a track; therefore, the global online tracks in the GTU consist of four tracklets at least, and six tracklets at most.

Using their positions, a linear fit is performed through the contributing tracklets. As the TRD is used for triggering on particles with momenta $\geq 2 \text{ GeV}/c$, the straight line is a sufficient approximation of the particle track [46]. The transverse momentum can be calculated from the transverse offset of the track to the nominal vertex position. Finally, the PID values of the contributing tracklets are averaged to yield the final value of the track. With both the track- p_{\perp} and the PID value given, a trigger decision can be made.

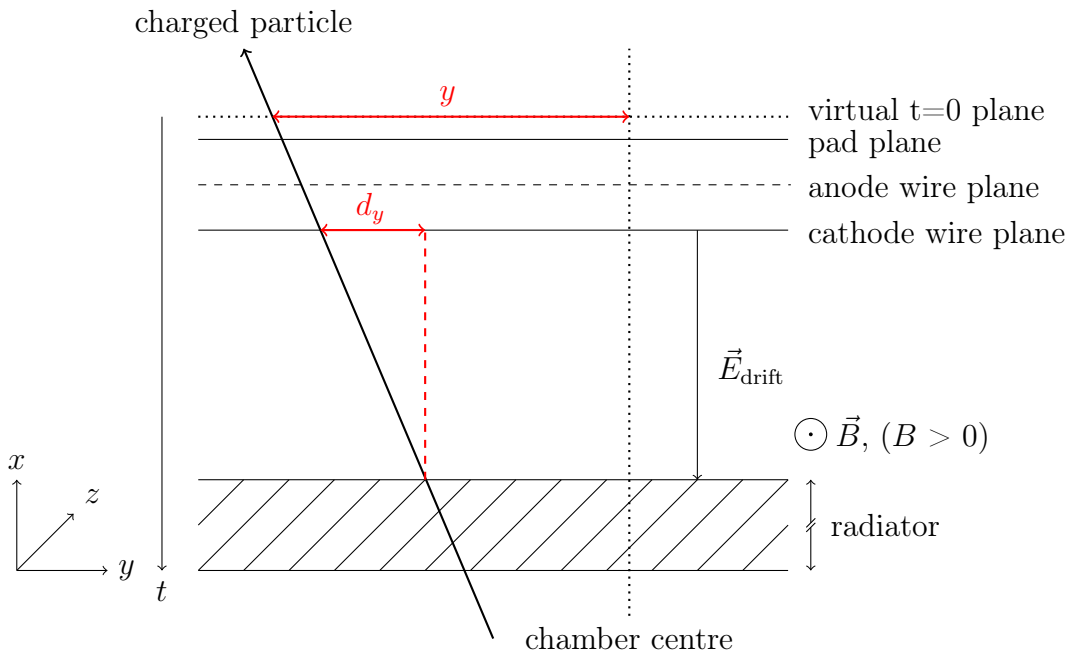


Figure 4.7: Sketch of the local online tracking (based on [43]). The transverse position y and the deflection over the drift length d_y are calculated in the TRAP for a tracklet, i.e. a segment of a track in one read-out chamber. Together with the z row of the MCM and a PID value based on the deposited charge, y and d_y form the description of the tracklet, stored in the tracklet word.

4.4.2 Offline tracking

Similarly to the cluster calculation during the local online tracking, clusters can be found in the TRD during the offline reconstruction of the raw data. Like the online clusters, they contain information about position and deposited charge; however, a number of corrections (concerning e.g. the drift velocity v_{drift} , variations of the gain, or $\vec{E} \times \vec{B}$ effects [46]) can be applied offline, as there is no need for a fast cluster finding to comply with the requirement of a low-latency trigger contribution. Thus, these clusters are used for the offline tracking and the offline PID calculation.

The TRD is part of the tracking of charged particles in the central barrel of ALICE, which is based on clusters of the individual detectors [46]. During the offline reconstruction stage, clusters at the outer radius of the TPC are used as seeds for the global tracking. The next step in the tracking algorithm, which uses a Kalman filter approach, is to search for further clusters at smaller TPC radii, as well as for ITS clusters. During the subsequent outward propagation, clusters from outer detectors like TRD or TOF are attached, updating the track parameters. The final track parameters are obtained with a last inward propagation to achieve the best possible precision. Storing the tracks with their parameters and PID information,

e.g. the deposited charge of the clusters, allows the subsequent particle identification with the TRD.

4.4.3 Offline particle identification

As already detailed in Section 4.2, particle identification with the TRD is based on measuring the specific energy loss in combination with transition radiation. As a basis, the TRD clusters which were attached to a global track during the tracking are used. To exploit the temporal evolution of the signal for electron identification, the clusters within one chamber are divided into seven equal slices, with each slice corresponding to ~ 5 mm of the drift/amplification region (for a particle passing the chamber at normal incidence). For each of the slices, a likelihood can be calculated for the deposited charge to belong to an electron. The subsequent combination of these “slice likelihoods” is the multi-dimensional likelihood (LQND) approach [52, 53]. In the end, to judge how well the TRD can identify electrons, the so-called electron and pion efficiencies are introduced. They can be calculated for different PID approaches, e.g. for the multi-dimensional likelihood method in one, two, or seven dimensions, as well as for different momenta, centralities, or contributing layers. In this way, the electron identification capabilities of the TRD depending on different parameters can be quantified [46]. A more detailed explanation of the performance evaluation using the electron/pion efficiencies and the multi-dimensional likelihood method will be given in Chapter 7.

4.5 Integration into AliRoot

In addition to the raw data, the online tracklets and tracks used for triggering are also stored and read out for each event. Accordingly, after the reconstruction step they are written to ESD files together with the global reconstruction output, and are subsequently available for analyses within the AliRoot framework in the classes `AliESDTrdTracklet` and `AliESDTrdTrack` [43]. While the ADC data are usually discarded after the cluster finding step in the reconstruction, they too can be stored, e.g. for a re-simulation of the local tracking in the TRAP (see the following paragraph).

Both for the local and the global online tracking, a realistic simulation is available in AliRoot. Figure 4.8 shows a sketch of the simulation chain for the online tracking: the digits containing the ADC data can either be produced in a MC simulation, or extracted from the raw data taken by the TRD. Tracklets, which form the basis for the global tracking simulation, are either again extracted directly from data, re-simulated in the TRAP simulation using raw ADC data as input, or simulated in a pure MC simulation [43].

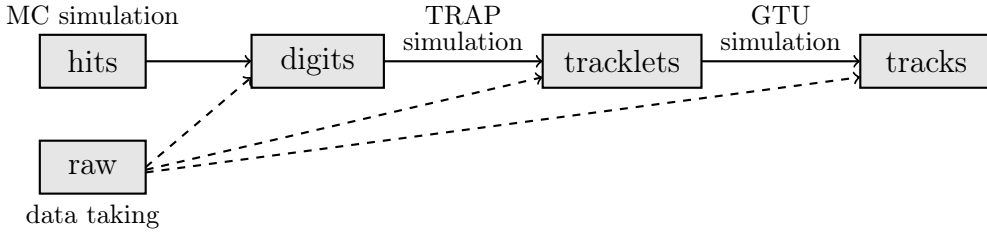


Figure 4.8: Overview of the online tracking simulation (adapted from [43]). In the simulation of the GTU, tracks are built from tracklets, which in turn are calculated in the TRAP simulation from digits obtained in a MC simulation. At every stage, the same structures — digits, tracklets, tracks — can be extracted from raw data for direct comparison.

The simulation of the local online tracking as it is performed in the TRAP is implemented in the class `AliTRDmcmSim`. To (re)produce results as close to the hardware as possible, the configuration of the TRAP during data taking is stored in the OCDB, and can be accessed in the simulation via the `AliTRDtrapConfig` class. The objects from this class contain the settings of all TRAP registers — for example the digital filters, or the cluster thresholds N_{CL}^{thr} and N_{CT}^{thr} — and are available in the OCDB via a reference, which consists of the configuration name and version [43].

It is also possible to build and subsequently store a new TRAP configuration in the OCDB, which has not been used for data taking (yet). This allows the testing of new TRAP settings in a MC simulation to see how the detector performance might be affected. In the course of this thesis, for example, a TRAP configuration with a new look-up table (used to translate the deposited charge of the tracklet into a PID value) was built and tested in a simulation. Particularly in view of the upgrade considerations for RUN 3, which foresee a change of the TRD online tracklet format (including changes in the TRAP), it will prove to be quite useful to extensively test new settings in MC simulations, before a final decision concerning the new tracklet format is made.

Chapter 5

Upgrade considerations for RUN 3

A major upgrade of the ALICE detector is foreseen for the third running period of the LHC, RUN 3, which at present is intended to start in 2021. The upgrade will be carried out during the preceding second long shutdown (LS2), which is currently planned to last from the end of 2018 to the end of 2020. This chapter is aimed at giving a short overview of the upgrade plans for ALICE in general, and a more detailed description of the upgrade considerations for the TRD. In particular, the differences in operation and available data for offline analyses between RUN 1/RUN 2 and RUN 3 will be pointed out, focussing mainly on the PID capabilities and constraints foreseen for RUN 3, which form the motivation for this thesis.

5.1 The ALICE upgrade for RUN 3

The fundamental components for the ALICE upgrade – i.e. the scientific objectives, as well as the detector upgrade plans – have already been formulated in 2012 in the letter of intent [54]. The physics goals of ALICE in RUN 3 will focus on precision measurements of the QGP, e.g. by measuring low-mass dileptons, heavy-flavour transport parameters, or the transverse momenta of quarkonia down to zero p_{\perp} [55]. As it is not possible to trigger on these probes, the ALICE upgrade strategy foresees the read-out of *all* collision events at a planned collision rate of 50 kHz for Pb–Pb collisions (as well as 200 kHz for pp and p–Pb collisions). This in turn requires a substantial increase in read-out speed of the detectors, which at present is limited to 500 Hz for Pb–Pb events. The upgrade plans for RUN 3 therefore include [54]

- the complete replacement of the six ITS layers with seven layers of monolithic pixel sensors to significantly improve the tracking and vertexing capabilities;
- the upgrade of the TPC read-out by replacing the MWPCs with Gas Electron Multiplier (GEM) detectors to enable a continuous read-out of the TPC;
- the upgrade and combination of the online and offline systems into the O^2 system, which will be able to handle the expected high rates [56];
- a new interface between the detector electronics and the O^2 system provided by newly developed Common Read-out Units (CRUs);
- the upgrade of the read-out electronics of TRD (i.e. replacing the GTU with a CRU), TOF, and the muon system to enable a high-rate data taking.

5.2 The TRD upgrade strategy

The TRD was originally designed for Pb–Pb collision rates of 8 kHz and is currently limited to read-out rates of a few kHz [55]. To cope with the increased collision rates planned for RUN 3, the TRD upgrade foresees two changes in the detector read-out: the GTU will be replaced by a CRU, which will provide a much higher bandwidth for the read-out; and the mode of operation of the FEE will be changed in order to reduce the processing time.

With the replacement of the GTU by the CRU, the limiting factor for the read-out speed is the FEE, which does not support multi-event buffering. This means that while one event is processed, the FEE is busy and cannot process another event, resulting in a dead-time of the TRD. For the collision rates foreseen for RUN 3, this means that the TRD will not be able to contribute data to all events that take place. A faster read-out is not possible with the current FEE; however, replacing the entire read-out electronics during LS2 (as it is done by other detectors) is also not feasible, as it would require taking apart every single chamber in all 18 supermodules. Instead, a compromise will be made between read-out speed and data volume: a reduced amount of processed data per event will be read out (instead of the raw data from the ADCs), thus increasing the read-out rate. A brief discussion of potential read-out modes to reduce the data volume, including possible advantages and constraints, is given in the following paragraphs.

5.2.1 Read-out modes

In the current mode of operation of the FEE, the read-out time of the online tracklets used to calculate the trigger contribution of the TRD lies in the range of 4 μ s to 8 μ s for each event, while the read-out time for the raw data amounts to several tens of microseconds [55]. The preferred option for RUN 3 is therefore the read-out of online tracklets for all events (i.e. disregarding the raw data), which will significantly increase the read-out rate of the TRD [57]. Assuming an average event read-out time of 6 μ s in the tracklet-only read-out mode, it was estimated in [55] that $\sim 76\%$ of the events could be read out by the TRD for Pb–Pb collisions at 50 kHz; in 200 kHz pp collisions, the fraction of events with TRD information would be reduced to $\sim 45\%$.

A possible drawback of a tracklet-only read-out is the limited amount of data which will be available: currently, 32 bits are used per tracklet to store the relevant tracklet parameters, i.e. transverse position, deflection, longitudinal position, and PID (cf. Section 4.4.1). In particular for the PID, the loss of granularity compared to the raw data currently used in offline analyses is expected to negatively influence the performance. Therefore, changes of the tracklet format to extend the available PID information are considered, which will be discussed in the next section.

In addition to the tracklet read-out, the read-out of the full zero-suppressed ADC data for a small fraction (e.g. every thousandth) of events is considered. These data

could then be used for quality monitoring and calibration, for example to determine the gain and the drift velocity, or to measure $\vec{E} \times \vec{B}$ effects.

5.2.2 Possible tracklet formats

Currently, up to four tracklets are calculated in parallel per MCM, which stores the tracklet parameters in a 32-bit word. For the transverse position y , 13 bits (signed) are available, while the deflection d_y is stored in a signed 7-bit value. For the longitudinal position z , 4 bits are enough to store the row of the MCM, while for the PID, the deposited charge assigned to the tracklet is transformed into an 8-bit value [43]:

$$\underbrace{pppp : pppp}_{\text{PID}} : \underbrace{zzzz}_{\text{long. position}} : \underbrace{dddd : dddy}_{\text{deflection}} : \underbrace{yyyy : yyyy : yyyy}_{\text{transverse position}}$$

While this distribution of the 32 bits among the four tracklet parameters was found to meet the demands for triggering in RUN 1 and RUN 2, it is not necessarily the best option for RUN 3, where no level-1 trigger contribution will be calculated by the TRD. Instead, the granularity of the tracklet parameters must be investigated with respect to the requirements of RUN 3, and the available storage should be re-distributed accordingly. Evaluating the performance of the PID for different bit sizes is the subject, and finding an adequate value to make a proposal for implementation is the goal of this thesis.

In the current implementation in the TRAP, the deposited charge, which is assigned to the clusters forming the online tracklet, is transformed to an 8-bit value via a look-up table. For the offline PID, on the other hand, the original cluster charge is available, without any reduction in granularity. Therefore, a way must be found to keep an adequate PID performance in offline analyses with the tracklet-only read-out planned for RUN 3. One option to be considered is to reduce the number of tracklets calculated in one MCM from four to three (or even two) [57]. The additional 32 bits (64 bits) could then be equally distributed to the remaining tracklets, increasing the available storage from 8 bits to 18 bits (40 bits for the case of two tracklets calculated in each MCM). However, it has to be determined whether three (or two) tracklets per MCM are enough to cope with the occupancy expected for RUN 3.

Another option could be to reduce the granularity of the deflection, i.e. to use less bits to store the deflection in favour of having more bits available for the PID. Table 5.1 shows the possible bits which could be used for the PID depending on the number of tracklets calculated per MCM, and for the two extreme cases of keeping the deflection as it is now (7 bits) and giving it up entirely. While the latter case is not really feasible for RUN 3, as the deflection is needed for the tracking in a high-multiplicity environment, it nevertheless serves as a limit for the range

tracklets/MCM	deflection included?	available PID bits
4	yes	8 bits
	no	15 bits
3	yes	18 bits
	no	25 bits
2	yes	40 bits
	no	47 bits

Table 5.1: Possible tracklet formats for RUN 3. Depending on the number of calculated tracklets per MCM and the inclusion of the deflection in the tracklet word, different numbers of bits will be available for the PID.

of possible PID sizes. Using this range of the resulting storage sizes as guidance, different bit values can be picked for the subsequent analysis of the PID performance in Chapter 7.

5.2.3 Constraints

At present, the detailed cluster information is used as input for the offline particle identification with the TRD. As briefly mentioned in Section 4.4.3, the clusters are calculated from the raw ADC data, which can be extensively processed and “improved” before being used for the PID calculation [57]. For example, a tail cancellation filter is applied to the offline data to reduce correlations between the different detector regions, i.e. the slices. Furthermore, a number of calibration parameters are stored for every run, which are needed to ensure that the clusters are correctly assigned to the slices. For the online tracklets, on the other hand, no real-time calibration parameters will be available, and the filtering and processing capabilities of the TRAP are limited.

In addition, only the sum of all contributing clusters — the total integrated charge — is available for each tracklet in the current implementation of the TRAP, instead of the individual cluster information. Consequently, the multi-dimensional likelihood approach, as it is currently used in the offline PID framework, cannot be applied to the tracklet PID for RUN 3. However, in the TRAP it is possible to directly calculate the deposited charge in two time slices, instead of the total integrated charge, without any additional delay. With an increased number of bits available to store the charge in two slices, the online PID performance could thus be improved. Technically, it would even be possible to calculate more than two slices; this, however, would have to be done in the CPUs by looping over the event data in the buffers [55], and would have to be implemented first.

A careful investigation of the different options for the online PID is therefore necessary to find the best option for the online PID, which will ensure a sufficient

performance with the tracklet-only read-out compared to the current offline PID capabilities. In the end, a compromise must be found between the achievable PID performance, the number of tracklets calculated per MCM (with regard to the occupancy), and the processing time.

Chapter 6

The analysis method

Within this thesis, the framework for the analysis of the tracklet-based PID approach has been developed. The analysis is divided into two parts: in the first part, which is implemented as an analysis task using ESD files as input, global offline tracks and TRD online tracklets are matched, and the available information on the deposited charge of the matched track-tracklets pairs is extracted and stored. The matching procedure, as well as further steps of online tracklet processing, are explained within this chapter. The output of the analysis task can then be used as input for the second part of the analysis, which evaluates the performance of the tracklet-based PID using the multi-dimensional likelihood method. The likelihood method and the processing steps necessary to calculate the likelihood and the final PID performance will be described in detail in Chapter 7.

6.1 Data access

In both parts of the analysis, data from a MC simulation produced specifically for this thesis are used as input. The MC events are generated by directly setting the event properties, e.g. the quantity, the species, or the momentum of the particles to be created. In this way, it can be ensured that a sufficient amount of electrons is available for the PID analysis — as opposed to a realistic simulation of pp or Pb–Pb collisions using e.g. PYTHIA as a generator, where only a small number of electrons (and a large number of pions) is produced per event.

For each event, 200 particles (50 e^+ , 50 e^- , 50 π^+ , and 50 π^-) were generated at a fixed momentum of 2 GeV/ c in a pseudo-rapidity range of $-0.9 \leq \eta \leq 0.9$, and distributed over the full azimuth. The particle momentum was chosen to be in the region where the separation of electrons and pions in the TPC starts to deteriorate and the PID contribution of the TRD becomes important due to the additional contribution of TR. For the TRD, an ideal detector geometry was assumed, meaning that there is no mis-alignment of the detector modules. In total, $\sim 100\,000$ events were produced, resulting in $\sim 20\,000\,000$ generated particles. Further details on the simulation can be found in Appendix A.1.

In the analysis presented in this thesis, the evaluation of the PID performance of different possible online tracklet formats is based on the online clusters, which are used to calculate the online tracklets. This allows the testing of different formats

using only one MC simulation as input, instead of having to produce a new simulation for every new tracklet format. The TRAP simulation is therefore an essential tool for this thesis, as it provides the possibility to store the online clusters in a dedicated file for further use. While only the data from the MC simulation are used in this analysis, it is also easily applicable on real data, which can simply be re-simulated using the TRAP simulation (see Section 3.3) to access the online clusters. The output of the simulation is written to ESD files, which can then be used for further analysis.

6.2 Offline track sample

In the first part of the PID analysis as presented in this thesis, the TRD online tracklets are matched to the global offline tracks which were calculated during the offline reconstruction process, as described in Section 4.4.2. This allows a direct comparison of the PID performance using the information from the offline tracks — as it is done in RUN 1 and RUN 2 — and the PID based on the online tracklets, as intended for RUN 3. Thus, a point of reference for the PID performance evaluation in Chapter 7 can be established.

Before the matching of the online tracklets takes place, the offline tracks are subjected to a number of selection criteria to ensure the quality of the data sample to be analysed. The analysis task was developed to be applicable to data from MC simulations as well as real data taken by the experiment. Therefore, the offline tracks first have to fulfil several requirements, which can be used for both MC and real data to make sure the track and PID quality are satisfactory. In the case of MC data, further selection criteria, as well as the identification of the particles associated with the offline tracks, are carried out using the available MC truth information.

For abbreviation, the global offline tracks are from here on simply referred to as “tracks”, while the TRD online tracklets will just be called “tracklets”.

6.2.1 Track quality

Only particles which originate from the primary vertex are considered in this analysis. Therefore, the tracks are required to have a distance of closest approach to the primary vertex of 3 cm at most in both transverse and longitudinal direction, and at least one hit in one of the two Silicon Pixel Detector (SPD) layers must be found. Furthermore, both ITS and TPC information must have been used for the track fit, and the track must have at least 80 clusters in the TPC. In addition, only tracks within a pseudo-rapidity range of $-0.9 \leq \eta \leq 0.9$ are considered.

To ensure that the tracks have crossed the TRD, hits in at least two TRD layers must have contributed to the calculation of the track. Furthermore, a lower limit is set for the momentum of the track, as electrons can lose a substantial amount of their energy via bremsstrahlung until they reach the TRD. The track momentum is calculated as the average of the momenta in the TRD layers (when available), and

the lower limit is set to $0.9 \text{ GeV}/c$. If a track fulfils these requirements, it is further processed, otherwise it is discarded.

Finally, for the simulated tracks, the MC truth is used to ensure that tracks truly originate from the primary vertex. The full list of track cuts is available in Appendix [A.2](#).

6.2.2 Track identification

In the next step, the PDG code [23] of the particle to which the track belongs is directly accessed using the available MC truth information. Thus, the tracks can be identified unambiguously, allowing the selection of only electrons and pions for further analysis.

If real data is to be used, the identification of the tracks can no longer be carried out using the MC truth information. Instead, the particles are identified using the TPC dE/dx signal (hence the necessity to ensure the track quality in the TPC). In addition, the PID information provided by the TOF detector can also be used to improve the identification; in this case, another cut is added at the track quality stage to ensure that the TOF information is available.

If a track fulfils all requirements up to this point, it will be used in the tracklet matching process described in the following section.

6.3 Tracklet matching and processing

In the matching stage of the analysis, tracklets are matched via spatial cuts to each track that has passed the selection criteria described in the previous section. Once the matching is completed, the additional information on the tracklet clusters, which was stored in a dedicated root-file during the simulation, is extracted for each matched tracklet. Before the clusters can be used for further analysis, they must be subjected to several corrections necessary to obtain the optimal PID information. Once these processing steps are successfully performed, the information needed for the analysis of the PID performance is stored for each “pair” of track and matched tracklets.

6.3.1 Matching procedure

Matching the tracklets to the offline tracks is restricted to the few pieces of tracking information which are available in the tracklet word – the transverse position y , the deflection d_y , and the longitudinal position z (see Section [4.4](#)). In addition, the identity of the chamber-half in which the MCM is located is stored when the tracklet information is read out. From this so-called half-chamber ID, the number of the read-out chamber can be deduced, which in turn allows the calculation of sector, stack and layer of the chamber. Based on these quantities, the matching algorithm is established, which is carried out for each offline track:

Firstly, the track is subsequently propagated from the outer edge of the TPC to the radial position of the anode wires in the respective layer of the TRD. Using the position information available from the track – given in the global coordinate system – the azimuthal angle φ , and thus the sector number, can be calculated. Afterwards, the coordinates of the track are transformed from the global to the local coordinate system of the TRD (cf. Sections 3.2.1 and 4.1.2), which will allow the comparison of the tracking coordinates of track and tracklet matching candidate.

In the next step, all tracklets which are found in the current event are extracted from the ESD file. For each tracklet, the layer and sector number are retrieved; if they do not agree with the corresponding information of the track, the tracklet is discarded. Otherwise, the tracking coordinates y and z are extracted from the tracklet word and compared with the ones from the track by calculating the residuals $\Delta y = |y_{\text{track}} - y_{\text{trkl}}|$ and $\Delta z = |z_{\text{track}} - z_{\text{trkl}}|$, and subsequently comparing them to a tunable threshold value. If the difference exceeds the threshold, the tracklet is discarded; otherwise, it is stored for further processing.

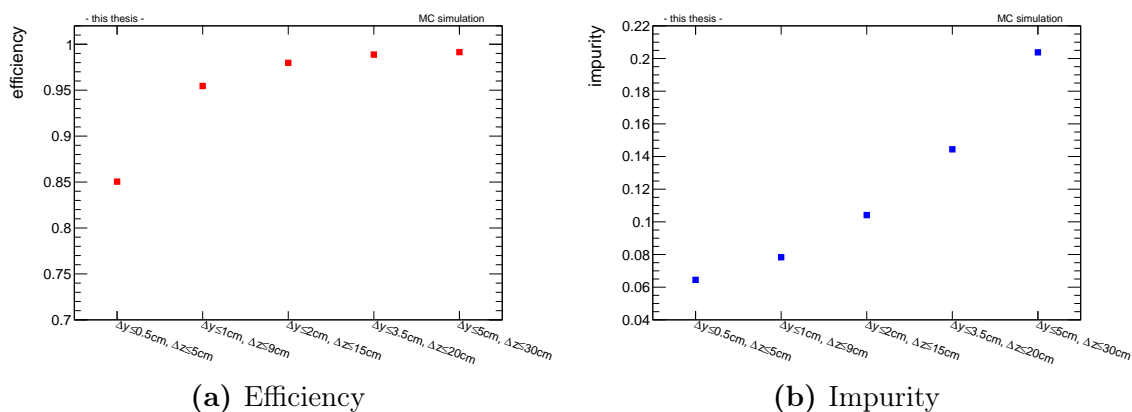


Figure 6.1: Efficiency and impurity after the tracklet matching for various matching windows.

For the decision on the threshold values, some considerations have to be made: if they are chosen too small, not all of the tracklets which truly belong to the track might be matched; and if they are chosen too large, it is possible that tracklets originating e.g. from secondary particles created in the material between the TRD layers are matched incorrectly. To investigate the effect of the threshold values on the matching, one can make use of so-called MC labels, which are assigned to the particles during their creation by the event generator. Since both track and tracklets carry the label of the particle they originate from, it is possible to clearly identify all tracklets belonging to the track in question via the MC labels. This allows the investigation of two quantities relevant for the matching: one is the *efficiency*, i.e. how many of the tracklets with the same label as the offline track are actually matched; the other one is the *impurity*, i.e. how many of the matched tracklets have a different label than the offline track. In Fig. 6.1a, the efficiency is shown for five different

pairs of threshold values — also referred to as matching windows — while Fig. 6.1b shows the impurity for the same windows. It can be clearly seen that, as expected, both the efficiency and the impurity of the matching increase if the matching window is widened. However, for the last three window sizes, the increase in efficiency is only small, while the impurity rises quite steeply. For the tightest window setting, on the other hand, the drop in efficiency is rather large, while the impurity is only improved by less than 2% compared to the next larger window. Therefore, the second tightest matching window shown in Fig. 6.1 ($\Delta y \leq 1$ cm, $\Delta z \leq 9$ cm) is chosen in this analysis, as it constitutes a compromise between a high efficiency of close to 96% and an acceptable impurity of around 8%. Furthermore, particularly the threshold value of $\Delta z \leq 9$ cm seems the most natural choice, as this corresponds to the maximum pad size in z direction (see Section 4.2).

Figure 6.2a shows the distribution of the difference in y between the offline track and all tracklets which fulfil the requirement $\Delta z \leq 9$ cm; equivalently, the distribution of the difference in z between the track and all tracklets meeting the condition $\Delta y \leq 1$ cm is depicted in Fig. 6.2b. As expected, there is a clear peak around 0 in both figures, which corresponds to all tracklets fulfilling both conditions $\Delta y \leq 1$ cm and $\Delta z \leq 9$ cm, showing that the matching in principle works as intended. The broad background visible in both figures is caused by those tracklets which fulfil only one condition ($\Delta z \leq 9$ cm in Fig. 6.2a and $\Delta y \leq 1$ cm in Fig. 6.2b). Accordingly, the chosen threshold values of 1 cm in y and 9 cm in z seem appropriate when looking at the distributions, as they ensure that this background is mostly cut away while at the same time preserving the peak around 0.

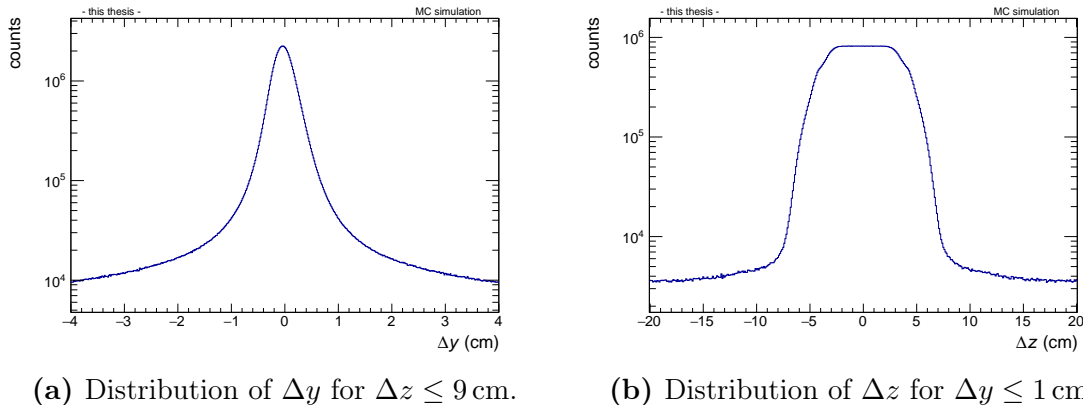
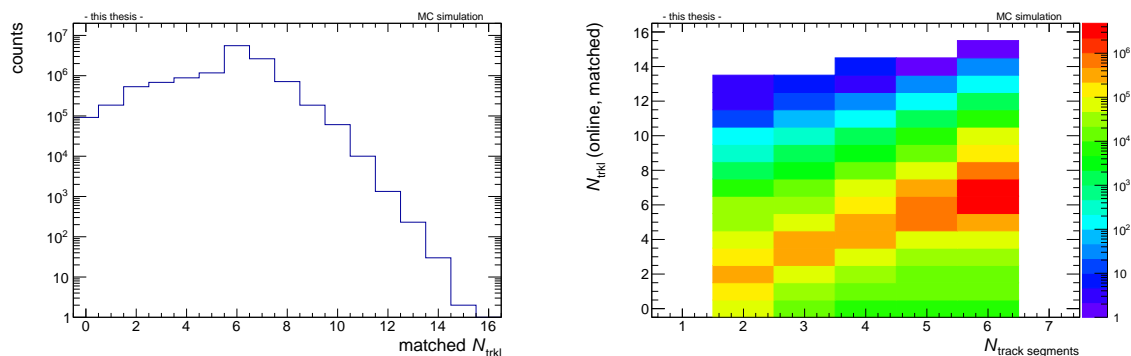


Figure 6.2: Distributions of the matching residuals. In (a), the difference Δy is shown for a fixed threshold in Δz , while in (b), Δz is depicted for a fixed threshold in Δy .

The tracklet matching can be further investigated by studying the number of matched tracklets per offline track, as depicted in Fig. 6.3a. In the most common case, six tracklets are matched to a track; however, it is also clear that with the matching algorithm as it is used in this analysis, more than one tracklet per layer can

be matched. This is desired, as it is possible that a tracklet is “split” over two rows in longitudinal direction — a phenomenon which will be explained (and corrected for) in Section 6.3.3. As Fig. 6.3a shows, this can result in matching as many as fifteen tracklets in the six layers to one track, even though this case is extremely rare. On the other hand, it is also possible that no tracklet is close enough to pass the spatial matching cuts, resulting in a track with no matched tracklets at all. This could for example be the case for a track which crosses the TRD on the border of two sectors. However, the number of those cases is almost two orders of magnitude smaller than the most common case of six matched tracklets, and only makes up a very small percentage of all matching cases.

In Fig. 6.3b, the number of matched tracklets per track is plotted against the number of offline track segments in the TRD layers. The number of offline track segments is shown on the x axis: due to the requirement of at least two contributing TRD layers (see Section 6.2.1), the number of offline track segments starts only at 2. Furthermore, given the six layers of the TRD, there can be at maximum six offline track segments which contribute to the track. The number of matched online tracklets, on the other hand, ranges from 0 to 15, as was shown in Fig. 6.3a. Still, in most cases, the number of track segments and the number of matched tracklets are equal, which manifests itself in the clear diagonal in Fig. 6.3b. Again, this indicates that the matching procedure works as expected.



(a) Number of matched online tracklets per offline track. (b) Number of matched online tracklets vs offline track segments.

Figure 6.3: Quality assurance of the tracklet matching.

6.3.2 Tracklet cluster processing

Following the tracklet matching, the clusters are extracted for each tracklet from the ROOT-file they were stored in. For this purpose, the tracklet word can be used to find the correct entry in the file, which allows the access of the cluster information in each time bin. Before the clusters can be used for PID, the dependence of the deposited charge on the pseudo-rapidity η has to be taken into consideration: if a particle crosses the TRD at a large $|\eta|$, the energy loss dE/dx will be larger than for

a particle passing the TRD at η close or equal to 0, as the distance the particle travels is longer, and thus more charge can be deposited in the chamber. While this effect is already accounted for during the offline reconstruction, it must be corrected for the online tracklets. For this purpose, the function `AliTRD1tuParam::GetElongation` is used, which provides the factor by which a tracklet in a given part of the TRD (parametrised by MCM, ROB, and ROC number) is longer relative to a tracklet with perpendicular incident angle. The correction factor for the deposited charge is therefore simply the reciprocal value of the elongation factor, and is depicted depending on η in Fig. 6.4. As expected, the correction factor is 1 for $\eta = 0$, where no correction has to be applied, and drops for large values of $|\eta|$, where the path length of the tracklet is longer and the energy loss larger.

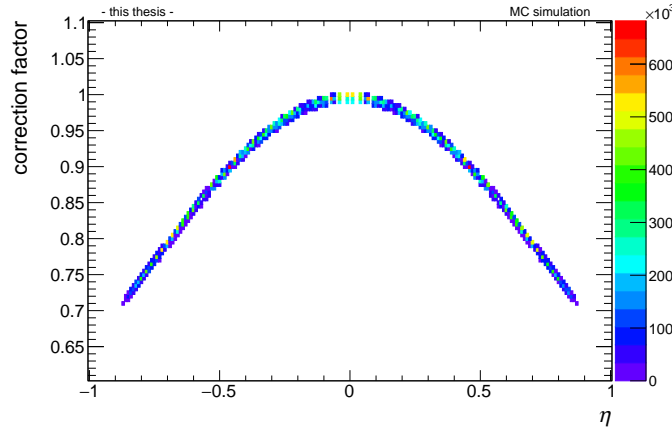


Figure 6.4: Correction factor for the tracklet cluster charge as a function of η .

Furthermore, it must be taken into account that the clusters still contain the baseline of the ADC signals, which must be subtracted. In summary, the deposited charge Q in the clusters is processed in each time bin n_{tb} as

$$Q'[n_{\text{tb}}] = Q[n_{\text{tb}}] \cdot x_{\text{corr}} - Q_{\text{baseline}}, \quad (6.1)$$

where x_{corr} denotes the correction factor shown in Fig. 6.4, and Q_{baseline} is the baseline. The cluster charge Q' is then used for further processing.

6.3.3 z-row merging

With the algorithm as it was established in Section 6.3.1, it is possible that more than one tracklet per layer is matched to the offline track. This is desired, as it may happen that a particle crosses the TRD under an angle such that the clusters are spread over several pads, which can result in the calculation of more than one tracklet per particle: if the charge is spread for example over the pads in two rows, i.e. in z direction, the tracklet calculation is performed by two different MCMs (as one MCM covers only one pad row). Accordingly, two separate tracklets are calculated instead

of one, as sketched in Fig. 6.5, with each of the tracklets carrying only part of the total charge deposited by the particle. Therefore, the cluster information of these “split” tracklets must be summed to recover the original deposited charge. Otherwise, this would result in a loss of charge, and would thus deteriorate the PID information. As the MCMs have no means of communicating over two pad rows, this so-called z -row merging of the tracklet clusters can only be performed offline, and is therefore implemented in the analysis task.

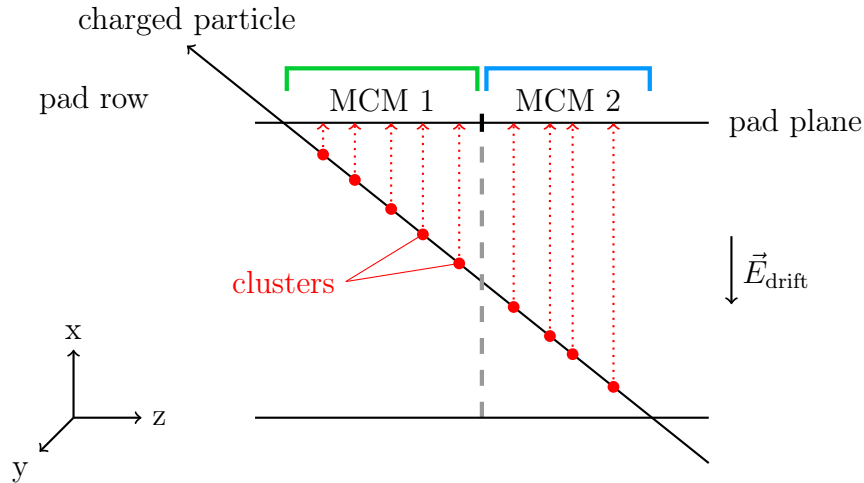


Figure 6.5: Sketch of the tracklet splitting across two z -rows (based on [58]).

6.3.4 Double-tracklet rejection

It is also possible that several tracklets per layer are matched which are located in the same pad row. This is expected from the algorithm used for the tracklet calculation (cf. Section 4.4.1), as the requirements for calculating a tracklet can be met in more than one channel of one MCM. As an example, we consider the case sketched in Fig. 6.6: the particle traverses the chamber under an angle such that the clusters are spread over the pads which correspond to channels 2 and 3. Accordingly, a tracklet is calculated from the clusters in channels 2 and 3, as the requirements $N_2 \geq N_{\text{CL}}^{\text{thr}}$ and $N_2 + N_3 \geq N_{\text{CT}}^{\text{thr}}$ are fulfilled. This tracklet, which is indicated by the green line in the sketch, is attributed the full deposited charge — it is, so to speak, the “correct” tracklet, which should be used for the PID analysis.

However, due to the spread of the clusters, it is now possible that there are enough clusters in channel 3 such that channels 3 and 4 also meet the requirements for the tracklet calculation — $N_3 \geq N_{\text{CL}}^{\text{thr}}$ and $N_3 + N_4 \geq N_{\text{CT}}^{\text{thr}}$ — even though there are no clusters at all in channel 4. This second tracklet, which is indicated by the orange line, is assigned only part of the originally deposited charge (that is, the charge from the clusters in channel 3). Hence, the orange tracklet would distort the PID information and therefore has to be discarded.

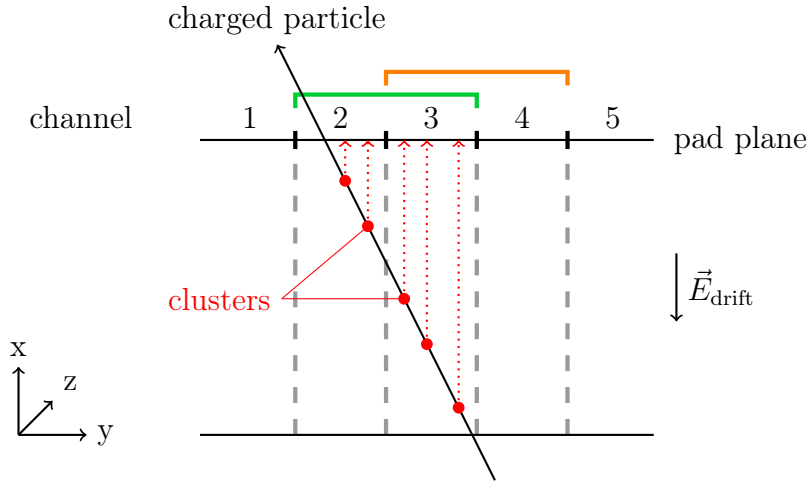


Figure 6.6: Sketch of double tracklets (based on [58]). Due to the online tracking algorithm, two tracklets can be calculated in one pad row, with one carrying the entire deposited charge (green), while the other is only attributed part of the charge (orange). To avoid the deterioration of the PID, the orange tracklet must be discarded.

As the calculation of double tracklets (mostly) occurs within one MCM, it can already be corrected in the FEE by checking if tracklets are calculated in neighbouring channels within one MCM, and then selecting only the one with the highest deposited charge. The rejection of double tracklets was already activated for the MC simulation used in this thesis. Still, the rejection capabilities in the FEE are limited, and not all double-tracklet cases are successfully sorted out; therefore, the double-tracklet rejection is also implemented in the analysis task: if two (or more) matched tracklets in one layer are found within the same pad row, the deposited charges are compared and the tracklet with the highest value is kept while the others are discarded.

After the double-tracklet rejection and the z -row merging, the cluster charges are subjected to a final quality check: only if the tracklet (or the two tracklets after merging) contains at least 18 clusters, which are spread from timebin 2 to at least timebin 20, it will be used for the PID calculation. The cluster information of the matched tracklets is then stored as the output of the analysis task, together with the particle species, the track momentum, and the deposited charge of the track. From this point on, the information on each track-tracklets pair can be used as the input for the PID analysis in Chapter 7.

Chapter 7

Evaluation of the tracklet-based PID approach

While the focus of the previous chapter mainly lay on the preparations for particle identification using online tracklets, in this chapter, the performance of the tracklet-based PID approach will be analysed. For the performance evaluation, a multi-dimensional likelihood approach is used, which will be introduced in the following section. Furthermore, the charge extracted from the tracklet clusters is transformed into a limited resolution representation, corresponding to the amount of bits which are considered for the storage of PID value in the FEE for RUN 3 (from now on referred to as “bit size” or “bits” for simplicity). Different combinations of the one-, two-, or three-dimensional likelihood methods and the bits form the data samples for which the PID performance will be analysed. Ultimately, this will result in a proposal for a combination of likelihood dimensionality and bits to be implemented in the FEE for RUN 3 in Chapter 8.

7.1 The multi-dimensional likelihood method

In this section, the likelihood method is illustrated based on the information from the offline tracks. The basic concept of the likelihood method is to “translate” the deposited charge in each TRD layer into an electron likelihood, and to subsequently combine the likelihood values in each layer to obtain the total electron likelihood for a particle traversing all TRD layers [53]. At first, the one-dimensional approach is introduced, which is later extended to two and three dimensions. In Section 7.3, the three methods are applied to the online tracklet information as well.

7.1.1 Likelihood in one dimension

As a first step, the deposited charge distributions of electrons and pions are obtained from the tracks for each layer. Here, only those tracks are taken into account which have a charge deposit in all six TRD layers. Furthermore, all seven slices (cf. Section 4.4.3) in which the charge deposit is stored in each layer must be filled. For tracks which fulfil these requirements, the sum of all seven slices, i.e. the total deposited charge, is extracted for each layer.

Figure 7.1 shows the normalised charge distributions of electrons and pions in one layer, for positively (Fig. 7.1a) and negatively (Fig. 7.1b) charged particles. This

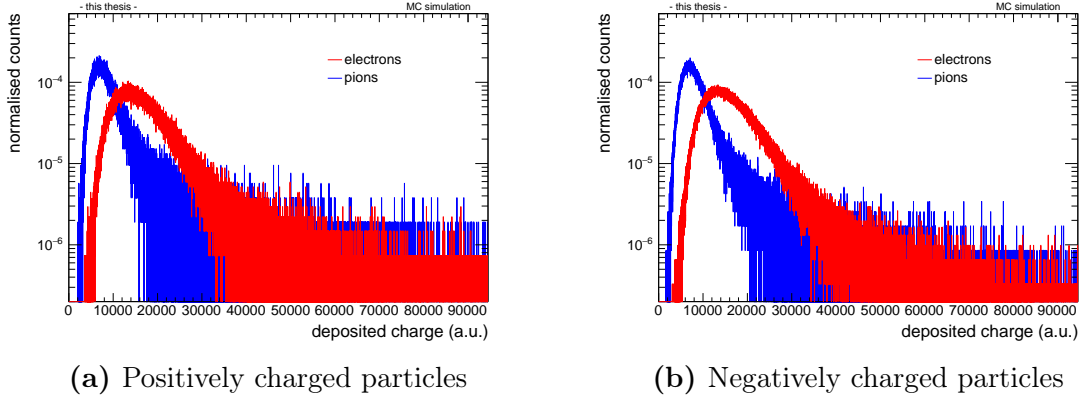


Figure 7.1: Deposited charge distributions of electrons and pions in one layer, obtained from the tracks for (a) positively charged particles, and (b) negatively charged particles.

separation is done since the behaviour of positive and negative charges differs slightly due to $\vec{E} \times \vec{B}$ effects. For both charges, the distributions of the electrons are clearly shifted to higher values, as the electrons deposit on average more charge in the TRD than the pions, both due to the specific energy loss by ionisation and the additional TR contribution (cf. Section 4.2).

The normalised electron and pion distributions can now be interpreted as the conditional probabilities $P(Q|e)$ and $P(Q|\pi)$, i.e. the probability that a particle which is an electron or a pion deposits the charge Q in the TRD [59]. Using these probabilities, the *electron likelihood* $L(e|Q)$ can be calculated as [53]

$$L(e|Q) = \frac{P(Q|e)}{\sum_k P(Q|k)} = \frac{P(Q|e)}{P(Q|e) + P(Q|\pi)}, \quad (7.1)$$

yielding the likelihood that a particle depositing the charge Q is an electron. While k generally denotes the different particle species, it is in this case replaced simply by electrons and pions, which are the only particles considered in this analysis. Extending this concept to the six layers of the TRD results in the electron likelihood for the charge Q_i deposited in layer i :

$$L_i(e|Q_i) = \frac{P_i(Q_i|e)}{P_i(Q_i|e) + P_i(Q_i|\pi)}. \quad (7.2)$$

In practice, the likelihood distributions depending on the charge Q are used in the form of LUTs. The entries of the LUTs can be calculated by taking each bin content of the electron charge distribution, and subsequently dividing it by the sum of the content of both the electron and the pion charge distribution in the same bin [58]. However, as the distributions fluctuate strongly in particular at high deposited charge, the resulting LUTs would strongly fluctuate as well. Therefore, the charge distributions are first smoothed using spline interpolation, shown in Fig. 7.2.

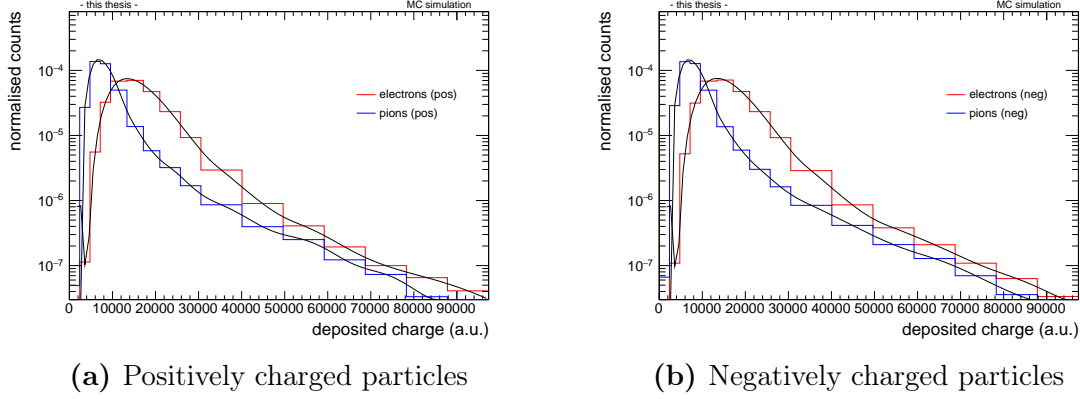


Figure 7.2: Spline interpolations of the deposited charge distributions obtained from the tracks (a) for positively charged electrons and pions, (b) for negatively charged electrons and pions. The original charge distributions are strongly re-binned to ensure the smoothness of the splines.

Based on the splines, the LUTs are now calculated as described above, by keeping the original binning of the charge distributions and evaluating the splines in each bin. Figure 7.3a shows the resulting LUTs for positively charged particles in all six layers. It is evident that the spline interpolation becomes problematic for very small and very large charge deposits, resulting in the (partly huge) fluctuations in the LUTs. To improve this, several steps of processing are performed: firstly, starting at small deposited charge, the LUTs are set to 0 as long as the original electron charge distribution (Fig. 7.1a) is still 0. Subsequently, the LUT values are fixed to the value of the minimum at a deposited charge of ~ 4000 (which in the case of the LUTs in Fig. 7.3a coincides with 0 as well). Secondly, for large charge deposits, the average value is determined at a deposited charge of $\sim 52\,000$, and set constant for all higher values to avoid the “wavy” behaviour caused by the splines. Thirdly, it becomes clear from Fig. 7.3a that particularly in the region of the step rise and the subsequent peak, the LUTs are quite similar in all layers; thus, for the range of deposited charge between ~ 4000 and $\sim 52\,000$, the average of all layers is calculated. The final LUT, which is now used for the positively charged particles in all six layers, is shown in Fig. 7.3b.

With the LUT for negative charges (which are shown in Appendix A.3) obtained in the same way, the likelihood L_i in layer i can be extracted, and the *combined electron likelihood*

$$L(e|\vec{Q}) = \frac{\prod_i L_i(e|Q_i)}{\prod_i L_i(e|Q_i) + \prod_i L_i(\pi|Q_i)} = \frac{\prod_i L_i(e|Q_i)}{\prod_i L_i(e|Q_i) + \prod_i (1 - L_i(e|Q_i))}, \quad (7.3)$$

where $\vec{Q} = \{Q_0, Q_1, \dots, Q_5\}$ denotes the deposited charges in the respective layers, can be calculated [53]. The obtained values of the combined likelihood are subsequently filled into two separate histograms for electrons and pions, respectively. An example

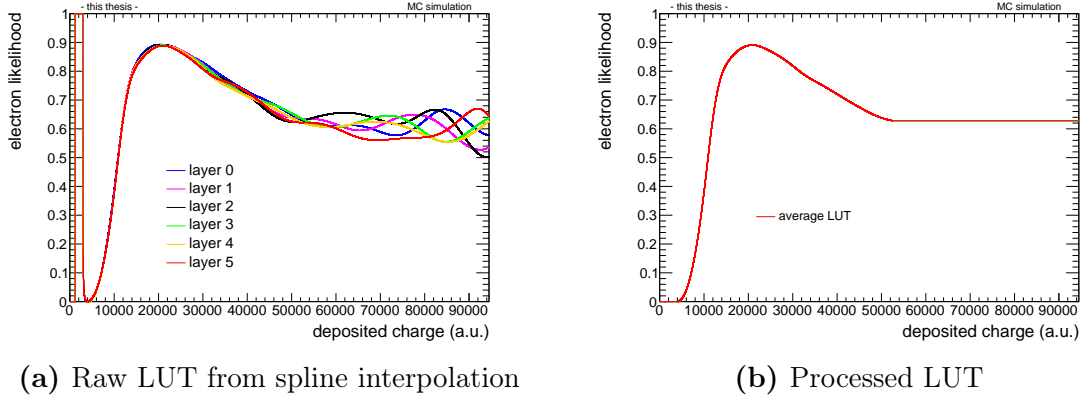


Figure 7.3: LUT creation using the spline-interpolated charge distributions (positively charged particles). To avoid the strong fluctuations caused by the edge effects of the splines seen in (a), the LUT is further processed, as detailed in the text. The resulting LUT is shown in (b).

for the resulting likelihood distribution of positively charged particles is shown in Fig. 7.4. As expected, a clear peak of electrons at likelihood values around $L(e|\vec{Q}) = 1$ can be seen, while pions are most often found close to $L(e|\vec{Q}) = 0$. Furthermore, rise of the pion curve at $L(e|\vec{Q}) = 1$ and of the electron curve at $L(e|\vec{Q}) = 0$ is visible. A possible explanation could be that there is still a large number of pions with a deposited charge in the region where the distribution of the electrons has its maximum (cf. Fig. 7.1). A likelihood value larger than 0.5 is therefore assigned to these pions. If this happens in several layers, the effect is “magnified” by the calculation method of the likelihood (Eq. 7.3): for the simplified example of a likelihood value of 0.6 in every layer, the resulting combined likelihood would amount to $L(e|\vec{Q}) = \frac{0.6^6}{0.6^6 + (1-0.6)^6} \approx 0.92$. From the LUT in Fig. 7.3b, it becomes clear that a likelihood value of 0.6 is obtained for a deposited charge of about 11 000. This means that for a non-negligible amount of pions, namely those in Fig. 7.1 with a deposited charge larger than 11 000, a combined electron likelihood between 0.9 and 1 would be calculated, causing an increase close to 1. Similar considerations can be made for electrons close to the maximum of the pion peak.

Based on this likelihood distribution, the performance of the PID can now be determined. This is done by calculating two quantities: the *electron efficiency* ε_e quantifies the fraction of electrons which have been correctly identified as electrons, while the *pion efficiency* ε_π gives the contamination of the electron sample, i.e. the fraction of pions which have been misidentified as electrons. The threshold t_e , for which an electron efficiency of $x\%$ is obtained from the electron likelihood distribution $f^e(L^e)$ (where L^e is shortened for the electron likelihood $L(e|\vec{Q})$), can be inferred

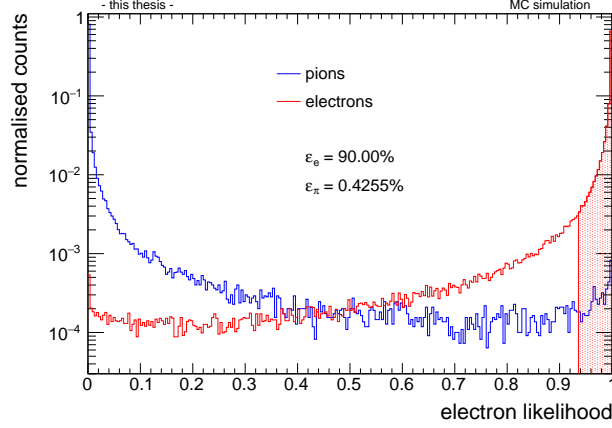


Figure 7.4: Likelihood distribution of positively charged tracks. The electron efficiency $\varepsilon_e = 90\%$ is marked by a red line. The fraction of pions contained in the red shaded area is the pion efficiency ε_π .

from the calculation of the electron likelihood:

$$\varepsilon_e = \frac{\int_{t_e(\varepsilon_e=x\%)}^1 f^e(L^e) dL^e}{\int_0^1 f^e(L^e) dL^e} \stackrel{!}{=} x\%. \quad (7.4)$$

For the example of $\varepsilon_e = 90\%$, a red line has been drawn in Fig. 7.4, marking the threshold $t_e(\varepsilon_e = 90\%)$. The pion efficiency at 90% electron efficiency is then calculated accordingly:

$$\varepsilon_\pi = \frac{\int_{t_e(\varepsilon_e=90\%)}^1 f^\pi(L^e) dL^e}{\int_0^1 f^\pi(L^e) dL^e}. \quad (7.5)$$

In practice, the electron efficiency is calculated by starting at an electron likelihood of 1, and subsequently going backwards and adding up the bin entries until the desired percentage — in our example 90% — of the total number of entries is reached. The final bin then corresponds to the lower limit t_e of the integrals in Eqs 7.4 and 7.5. The pion efficiency is accordingly given by the number of entries of the blue curve within the shaded area between t_e and 1 in Fig. 7.4. Note that using this procedure, it is possible that the electron efficiency can deviate from the target value, as will be seen for the higher-dimensional likelihood methods in the next section.

The pion efficiency is now calculated for electron efficiencies between 70% and 95%, as shown in Fig. 7.5. As expected from Fig. 7.4, the pion efficiency increases with increasing electron efficiency. The offline performance will be further discussed

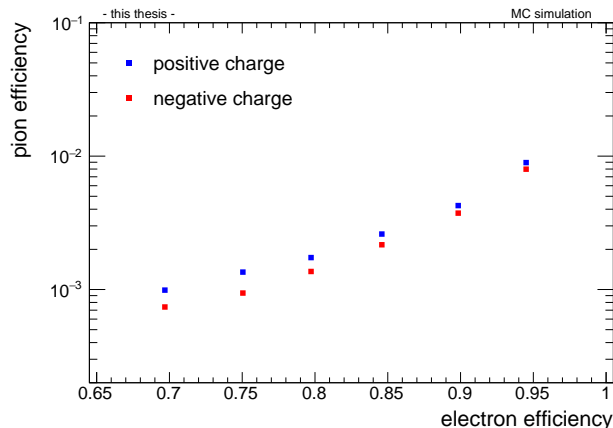


Figure 7.5: Pion efficiency vs electron efficiency for the offline tracks, calculated using the LQ1D method.

in Section 7.3, together with the online performance, on the basis of plots like the one in Fig. 7.5.

7.1.2 Extension to two and three dimensions

The one-dimensional likelihood method can be extended to n dimensions by dividing the temporal evolution of the signal into n slices. This allows the separation of the deposited charge in different time intervals, illustrated in Fig. 7.6 for the simplest case of two dimensions. Here, the average signal generated by electrons in the FEE is divided such that the first slice covers the amplification peak and part of the drift region, while the second slice contains the TR peak. In this way, additional information on the identity of the particle can be obtained: as pions do not produce TR in the momentum region of interest, a high amount of charge in the second slice would point strongly to an electron, while a low amount would more likely indicate a pion.

During the reconstruction of the offline tracks, the charge deposited in each TRD layer is stored in seven time slices. Thus, a likelihood approach with up to $n = 7$ dimensions is possible with the offline charge, as shown for example in [46]. In this thesis, however, the multi-dimensional likelihood method will be used only for $n = 2$ and $n = 3$ slices (from here on referred to as LQ2D and LQ3D). For the LQ2D approach, the signal in the original seven slices is split up 4 – 3, meaning that the charge deposited in the first four slices is combined to form the new first slice, while the sum of the charges in the last three slices constitutes the new second slice. Likewise, the slices are re-distributed 3 – 2 – 2 for the LQ3D method. Figure 7.7 shows the charge distributions for positively charged particles in the two slices, which are used in the LQ2D approach. While the charge distributions of the pions are similar in both slices, a clear difference can be seen for the distributions of the electrons, which is due to the additional TR contribution in the second slice.

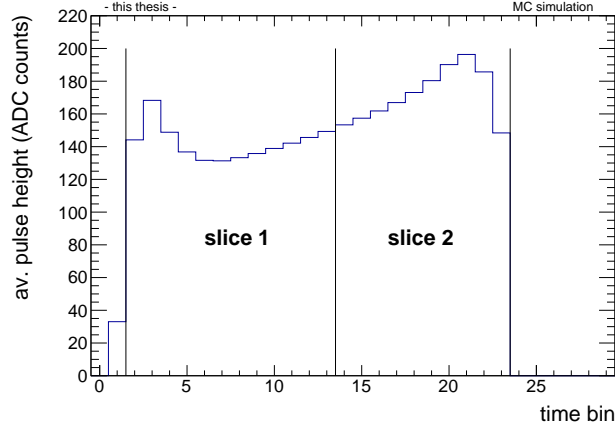


Figure 7.6: Splitting of the time interval into two time slices, shown for the temporal evolution of the average signal of electrons in the TRD.

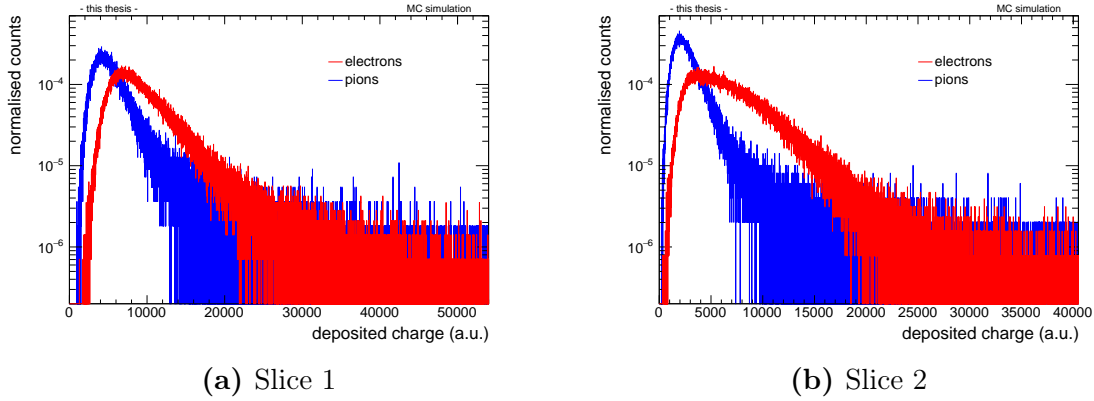


Figure 7.7: Deposited charge distributions of positively charged electrons and pions in one layer, obtained from the tracks for (a) slice 1, and (b) slice 2 as used for the LQ2D method.

A similar behaviour is exhibited by the charge distributions in the three slices of the LQ3D method, shown in Fig. 7.8. Again, the distributions of the pions remain similar in all slices, but the charge distributions of the electrons in the second and particularly in the third slice show the influence of the TR contribution. (The distributions for negatively charged particles are shown in Appendix A.3.)

In analogy to the procedure in the previous section, LUTs can be created for the slices. As becomes clear from the charge distributions in Fig. 7.7, the LUTs must be generated for each slice separately. For the layers, however, the LUTs in the respective slice behave very similar, thus motivating the calculation of the average of all layers as it is done in the LQ1D approach. In Fig. A.30, the LUTs calculated for positively charged particles in the two slices of the LQ2D method are shown. The

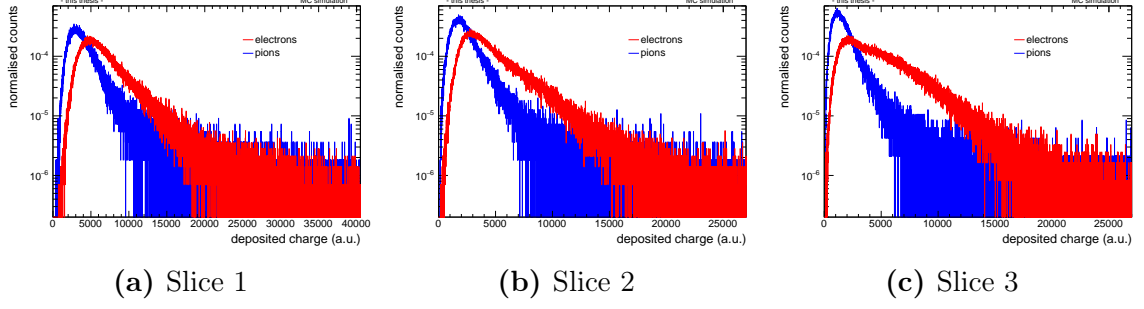


Figure 7.8: Deposited charge distributions of positively charged electrons and pions in one layer, obtained from the tracks for (a) slice 1, (b) slice 2, and (c) slice 3 as used for the LQ3D method.

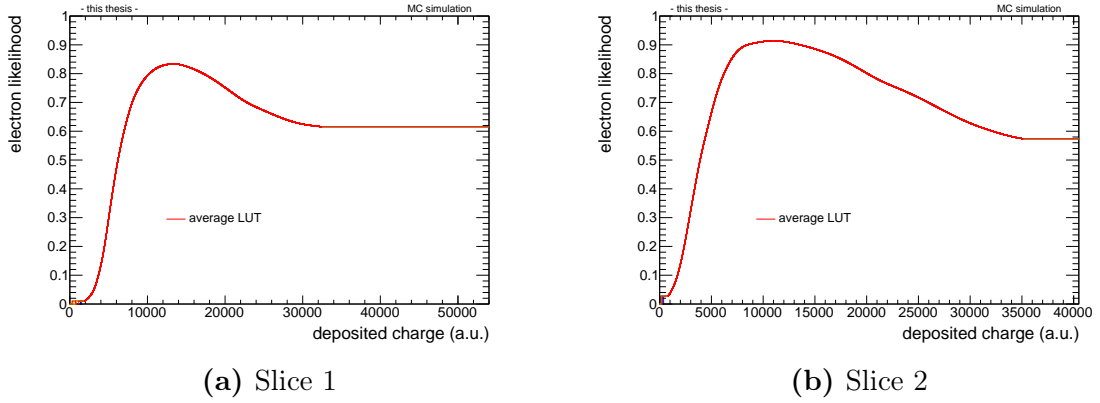


Figure 7.9: LUTs for positively charged tracks (a) in slice 1 and (b) in slice 2 as used for the LQ2D method.

LUTs for the negatively charged particles, as well as those for the LQ3D method, can be found in Appendix A.3.

Using the above LUTs, the likelihood $L_{i,j}$ can be obtained for each slice j in layer i . The likelihood in one layer i is then calculated by combining the likelihoods in the slices via

$$L_i^e = \frac{\prod_j L_{i,j}^e}{\prod_j L_{i,j}^e + \prod_j L_{i,j}^\pi} = \frac{\prod_j L_{i,j}^e}{\prod_j L_{i,j}^e + \prod_j (1 - L_{i,j}^e)} \quad (7.6)$$

(where the electron likelihood $L(e|Q)$ is again shortened to L^e for simplicity). In this approach, the charge sums in the slices are assumed to be uncorrelated, and the electron likelihood is calculated for each slice independently. For a truly n -dimensional likelihood, as for example used for two dimensions in [53], the correlations between the deposited charge in the slices would have to be taken into account. This is however complicated by the increasing need for statistics at higher dimensionality. Therefore, the simplified approach of treating all slices independently, which still

7.1 The multi-dimensional likelihood method

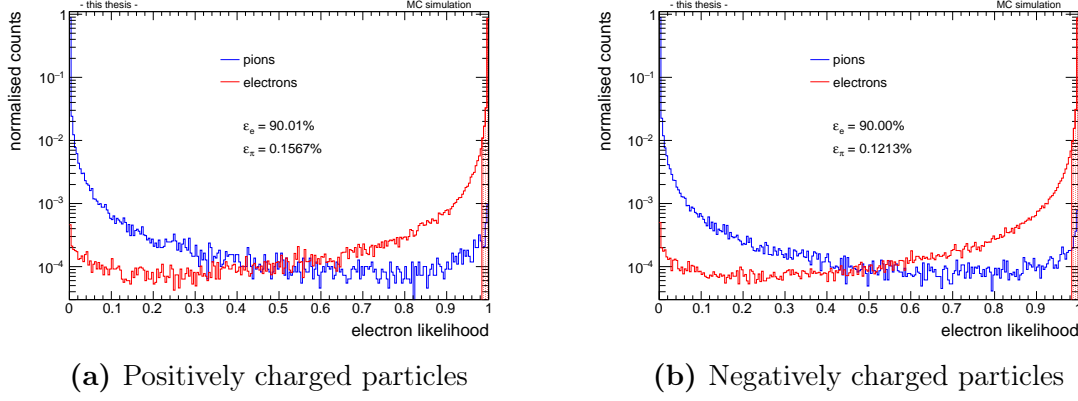


Figure 7.10: Likelihood distribution of (a) positively charged tracks and (b) negatively charged tracks for the LQ2D method. Within the shaded area, 90% of the electrons are contained.

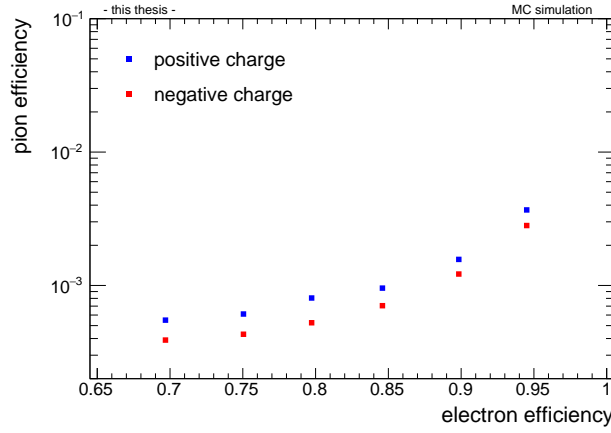


Figure 7.11: Pion efficiency vs electron efficiency for the offline tracks, using the LQ2D method.

greatly improves the performance compared to the LQ1D method, is used. The combined electron likelihood can now be calculated by inserting Eq. 7.6 into Eq. 7.3:

$$L^e = \frac{\prod_i L_i^e}{\prod_i L_i^e + \prod_i L_i^\pi} = \frac{\prod_i \prod_j L_{i,j}^e}{\prod_i \prod_j L_{i,j}^e + \prod_i \prod_j (1 - L_{i,j}^e)} \quad (7.7)$$

The resulting likelihood distribution is shown for the two-dimensional likelihood approach in Fig. 7.10. Again, the area which contains 90% of the electrons is marked accordingly. Due to the way the combined likelihood is calculated, the distributions are shifted even more to the “extreme” values of 0 and 1 compared to the LQ1D likelihood distribution, resulting in an increase of both the electron and the pion

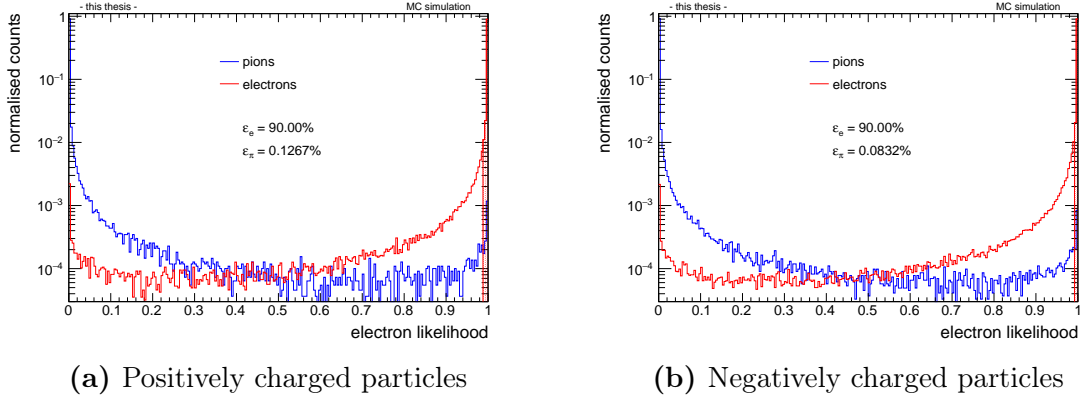


Figure 7.12: Likelihood distribution of (a) positively charged tracks and (b) negatively charged tracks for the LQ3D method. Again, the electron efficiency of 90% is marked by the red line.

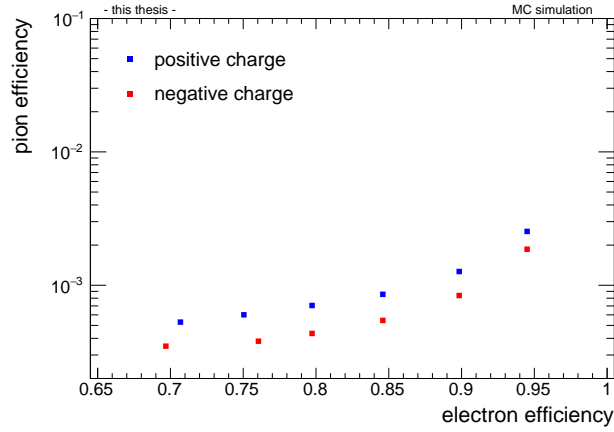


Figure 7.13: Pion efficiency vs electron efficiency for the offline tracks, calculated using the LQ3D method.

distribution at the edges of the figure. After calculating the pion efficiency at the different electron efficiencies between 70% and 95%, a clear improvement of the performance using the LQ2D method can be seen when comparing Fig. 7.11 to Fig. 7.5.

For the three-dimensional approach, the shift of both likelihood distributions to 0 and 1 is even more pronounced (see Fig. 7.12), as more likelihood values are included in the calculation of the combined likelihood. This affects the calculation of the electron efficiency, as illustrated in Fig. 7.13: for small electron efficiencies (70% and 75%), the electron efficiency is overestimated, resulting in the slightly displaced values in Fig. 7.13. In addition, the performance at small electron efficiencies hardly improves with respect to the 2D approach due to the increased contamination. For electron efficiencies above 80%, however, a clear improvement with respect to the

LQ2D method is visible, although it is not as strong as the improvement from LQ1D to LQ2D.

7.2 Analysis strategy for the tracklet-based PID

The calculation of the multi-dimensional likelihood method as presented above can be applied in the same way to the charge extracted from the online tracklet clusters, which will be used in the following analysis of the tracklet-based PID approach. The analysis focuses on three aspects of the tracklet calculation in the FEE, which can be tuned to achieve a performance suitable for RUN 3. The first one is the amount of bits which are available in the tracklet word to store the PID value (see Section 5.2.2). The second one is the time interval in which the deposited charge is collected, which in RUN 1 and RUN 2 simply contains all time bins, thus corresponding to the “slice” used in the LQ1D method. It is, however, also possible in the FEE to accumulate the charge in two or more time intervals, which can subsequently be employed in offline analyses to calculate the electron efficiency with the two- (or higher-)dimensional likelihood approach. The third aspect which can be tuned is the function used to transform the raw deposited charge into the PID value, which is implemented in the TRAP in the form of a LUT (see Section 4.4).

The following investigation of the most suitable combination of bits and time slices is divided into two steps: during the *training*, the first half of the data is used to create the LUTs needed for the multi-dimensional likelihood method, as described in the previous section. For the LUT calculation, the deposited charge in the clusters of the online tracklets, from here on also referred to as “full information”, is used.

Subsequently, the electron and pion efficiencies are determined for the second half of the data during the *analysis*. The tracklet cluster charge is transformed into n bits (see Section 7.2.2), where the value of n can be chosen from a set of suitable bit sizes. The PID performance is calculated for different combinations of n bits and likelihood dimensionality, which form the data samples (defined in the next paragraph).

In the end, the performance of the different combinations can be compared with each other, as well as with the offline results, which serve as a reference for the best performance achievable in this analysis.

7.2.1 Definition of samples

The different combinations of dimensionality and number of bits which will be analysed are summarised in Table 7.1. The following considerations concerning the bit values were made: firstly, the values of 8 bits, 18 bits, and 40 bits correspond to the available bits when calculating four tracklets, three tracklets, or two tracklets per MCM (see Section 5.2.2). In addition, 12 bits and 25 bits were chosen as intermediate values, while the 6-bit value is only used for the LQ1D case to illustrate how the performance would deteriorate. Secondly, it must be taken into account that some combinations of bits and likelihood dimensionality will not produce sensible results.

	6 bit	8 bit	12 bit	18 bit	25 bit	40 bit	full
LQ1D	✓	✓	✓	✓	✓	X	✓
LQ2D	X	✓	✓	✓	✓	✓	✓
LQ3D	X	X	✓	✓	✓	✓	✓

Table 7.1: Definition of data samples. Shown are the combinations of multi-dimensional likelihood method and bits, which are analysed in this thesis.

For the combination of LQ3D and 8 bit, for example, the 8 bits would have to be distributed onto the three slices, resulting (in the simplest case) in one slice with 2 bits and two slices with 3 bits. As no reasonable performance can be expected from this, the combination is omitted. The same reasoning applies for the combinations of LQ2D/LQ3D and the 6 bit-case. Furthermore, the combination of the LQ1D method and the 40 bits is omitted as well, since this exceeds by far the granularity available in the FEE. Finally, the performance of the full cluster information is also analysed for all three likelihood methods.

7.2.2 Transformation to n bits

The full cluster charge of the tracklets, denoted as Q , is translated into an n -bit value $Q_{n\text{bit}}$ using a transformation function f as

$$Q_{n\text{bit}} = f(Q). \quad (7.8)$$

However, to use the LUTs which are created based on the full information, $Q_{n\text{bit}}$ must first be transformed back using the inverse of the function,

$$Q' = f^{-1}(Q_{n\text{bit}}), \quad (7.9)$$

where Q' is now again in the “same” range as Q , but with a “resolution” of n bits.

In the analysis presented in this thesis, two different transformation functions will be used, and their results compared. The first is a simple linear function, shown in Fig 7.14 for the transformation of the cluster charge (given in ADC counts) to 8 bits. The second function, on the other hand, is non-linear with a sharp rise in the range where the charge distributions of electrons and pions overlap (see Fig. 7.15). In this way, the charge in the region which is particularly important for the likelihood calculation can be transformed with a higher resolution compared to the linear function.

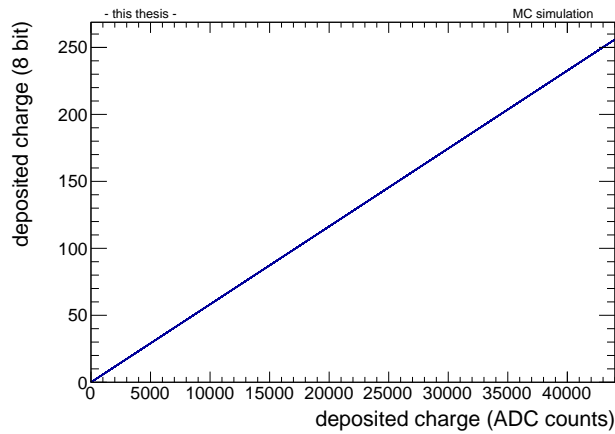
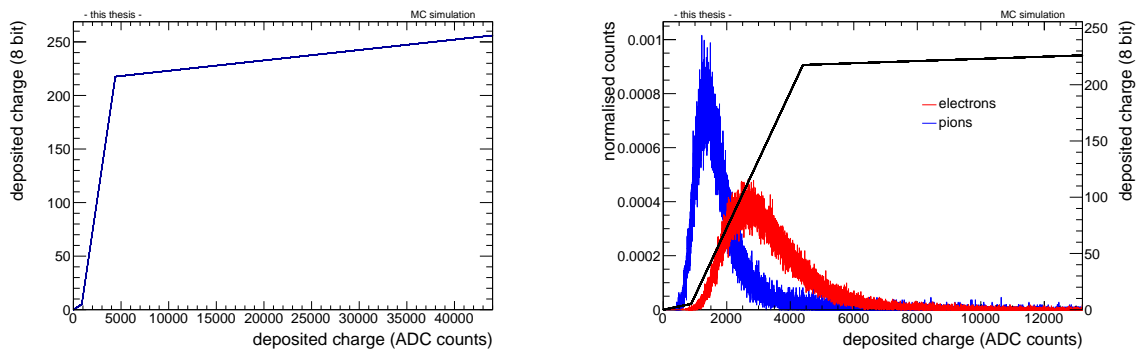


Figure 7.14: Linear transformation function. The deposited charge of the tracklets, given in ADC counts and ranging from 0 to 44 000, is translated into an 8-bit range.



(a) Non-linear transformation function (whole range) (b) Non-linear transformation function with deposited charge distributions (zoomed in)

Figure 7.15: Non-linear transformation function. In (a), the transformation function is shown over the whole range of ADC counts. In (b), the function is drawn together with the deposited charge distributions for the positively charged tracklets to illustrate the intended improvement of the transformation. Note that the range of the deposited charge is zoomed in.

7.3 Performance evaluation

To analyse the tracklet-based PID performance, the steps presented in Section 7.2 are applied to the data samples defined in Table 7.1 using the deposited charge from the online tracklet clusters as input. In parallel, the same analysis is performed for the offline tracks to provide a reference. This means in practice that for both offline and online information, a set of LUTs is created using the full charge information. Subsequently, for each track-tracklet pair, the deposited charge in each layer and slice is first transformed to n bits, and then transformed back to look up the electron likelihood. The likelihood values are combined according to Eq. 7.7, yielding the total electron likelihood of the track as well as the total electron likelihood of the matched tracklets. From the resulting likelihood distributions, the pion efficiency is calculated for a given electron efficiency separately for the offline and the online data, which can then be directly compared. This will be done in Sections 7.3.2 and 7.3.3 for the two transformation functions shown in Fig. 7.14 and Fig. 7.15, after some considerations presented in the next section.

7.3.1 Prior considerations

Before the actual analysis is performed, each track-tracklet pair is subjected to a number of selection criteria: as already mentioned in Section 7.1.1, only tracks with a charge deposit in every layer of the TRD are considered. Furthermore, all seven slices in each layer must be filled, i.e. the track must have deposited charge along the entire length of the chamber. Analogously, the tracklets are required to have a certain length at least (see Section 6.3.2), and there must also be a tracklet in each layer. Finally, only tracks with an average momentum in the TRD of $1.2 \leq p \leq 2.4 \text{ GeV}/c$ are taken into account. This momentum range was chosen in view of applying the same analysis on real data at some point, where the tracks will be identified using the dE/dx information provided by the TPC and the TOF detector. As this PID information can be contaminated by protons at momenta below $\sim 1.1 \text{ GeV}/c$, and by deuterons at momenta above $\sim 2.4 \text{ GeV}/c$, the momentum cut will ensure a clean sample. For the analysis in this thesis, it was simply kept in place (although not needed, as the available MC truth information already ensures that only electrons and pions are analysed). Only if the *set* of track and matched tracklets fulfils these criteria, it is further analysed. This means that all cases are excluded from the analysis where a track would be analysed, but not the matched tracklets, or vice versa.

Once the track-tracklet pair has passed the above requirements, the deposited charges can be extracted. As a first step of quality assurance, the charge of the track segment in a layer is compared to that of the matched tracklet. Figure 7.16 shows this charge correlation for the total deposited charge of both electrons and pions, combined for all layers. Several observations can be made from this plot: firstly, the scales of the deposited charge are different for offline and online information, as the online charge is directly extracted from the FEE (given in ADC counts), while

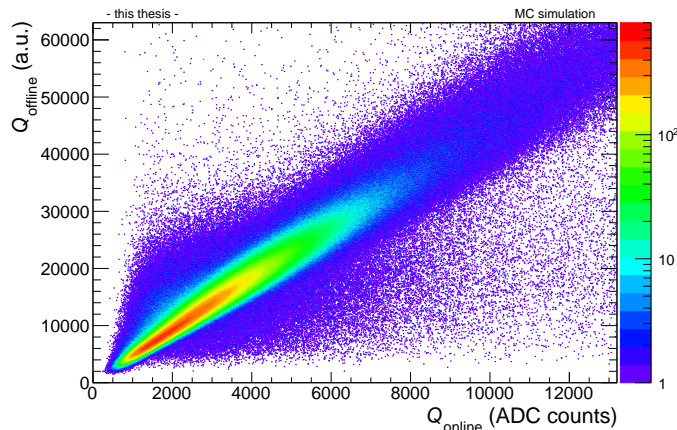


Figure 7.16: Correlation of the deposited charge extracted from the online tracklets and the deposited charge obtained from the offline tracks in all chambers. The tracklet charge Q_{online} is given in ADC counts, while the track charge Q_{offline} is shown in arbitrary units.

the offline charge is processed (given in arbitrary units). A conversion factor can be calculated from Fig. 7.16 to be approximately 4.81 for the conversion from online to offline charges.

Secondly, there are noticeable “bulks” deviating from the diagonal where most of entries are found. These could be caused by the impurity of the tracklet matching, since mismatched tracklets which do not truly belong to the offline track would not have a matching deposited charge, thus entering the correlation plot off the correlation diagonal.

Thirdly, the distribution, which ideally should just be a diagonal line, seems to be quite smeared out, indicating a systematic difference between online and offline charges. One possibility where such a discrepancy could be introduced is the gain correction, which is performed differently online and offline. To test whether this really has any influence on the charge correlation, an ideal MC simulation without any gain variations was produced. The resulting charge correlation is shown in Fig. 7.17. Compared to the distribution with gain variations in Fig. 7.16, a clear improvement can be seen. To further quantify this, a projection of the online charge is made at $Q_{\text{offline}} = 10\,000$ and fitted with a Gaussian to determine the width. The results are shown in Fig. 7.18a for the simulation with gain variations, and in Fig. 7.18b for the ideal simulation. Without gain variations, the width of the distribution is nearly cut in half, confirming the impression given by the charge correlation plot.

To understand what happens in the simulation with gain variation, a closer look must be taken at the correction procedure in the FEE: firstly, a correction is applied for each pad on the pad plane. This happens during the filtering stage, i.e. *before* any clusters are calculated in the TRAP (cf. Section 4.4.1). Secondly, the gain is corrected for each MCM *after* the clusters have been found. In the simulation of the FEE, which is included in the MC simulation, this behaviour is imitated.

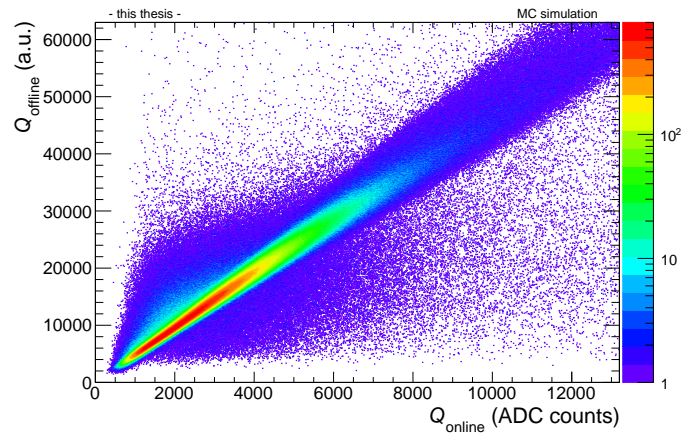


Figure 7.17: Correlation of online and offline charge for the ideal simulation (no gain variations). The smearing is clearly reduced compared to the simulation with gain variations.

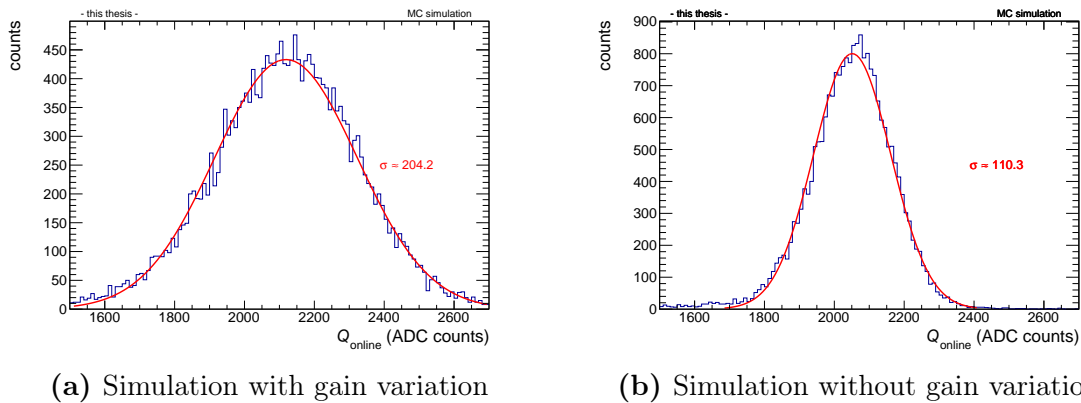


Figure 7.18: Projection of the online charge at $Q_{\text{offline}} = 10000$. For the simulation with gain variations, the distribution, shown in (a), is nearly twice as wide as the distribution for the simulation without gain variations, shown in (b).

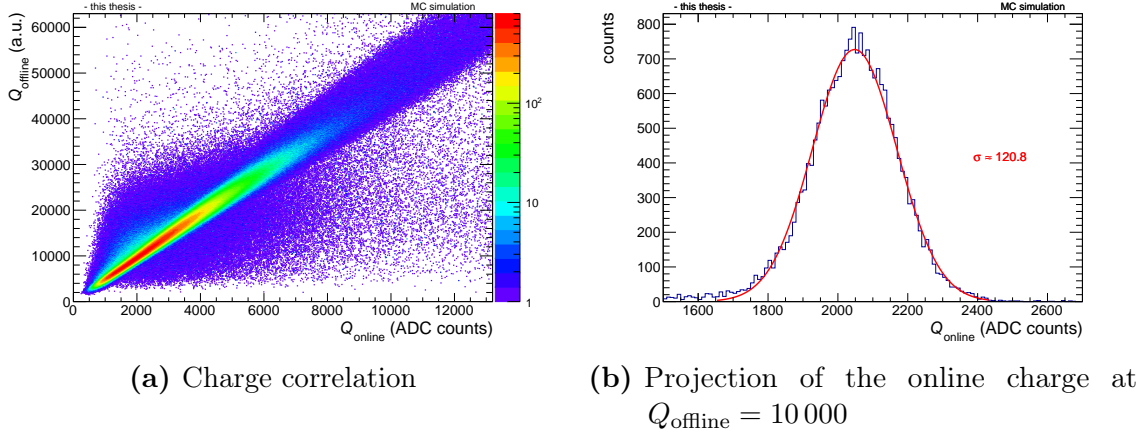


Figure 7.19: Charge correlation and online charge projection for the simulation with the MCM-wise gain correction applied.

However, the tracklet clusters which are used in this analysis are stored before the gain correction for the MCMs is applied. Therefore, they are only corrected pad-wise, meaning that the MCM-wise correction must be applied “by hand” — otherwise, the online charge is smeared out compared to the offline charge (for which the gain variations are properly corrected during the offline reconstruction). Indeed, once the MCM-wise correction is applied to the clusters, the charge correlation looks very similar to the one without any gain variations, see Fig. 7.19a. This is further underlined by the width of the distribution in Fig. 7.19b, which is only slightly wider (due to the fact that the gain correction does not work perfectly). Thus, the MCM-wise gain correction is applied to the clusters used in the following analysis.

7.3.2 Performance using the linear function

In the following paragraphs, the performance of the different data samples is presented sorted by the dimensionality of the likelihood method; in the end, the results of all data samples are compared for an electron efficiency of 90%. For the transformation of the full information to the bit sizes, the linear function shown in Fig. 7.14 is used. The results for the transformation with the non-linear function, presented in Section 7.3.3, will conclude this chapter.

LQ1D

Analogously to the offline information in Section 7.1.1, the charge distributions of the tracklets are obtained for each layer, and subsequently described by spline interpolations to create the LUTs. For the calculation of the total integrated charge, the cluster charge in 22 time bins is added up, starting from time bin 2, as illustrated in Fig. 7.20.

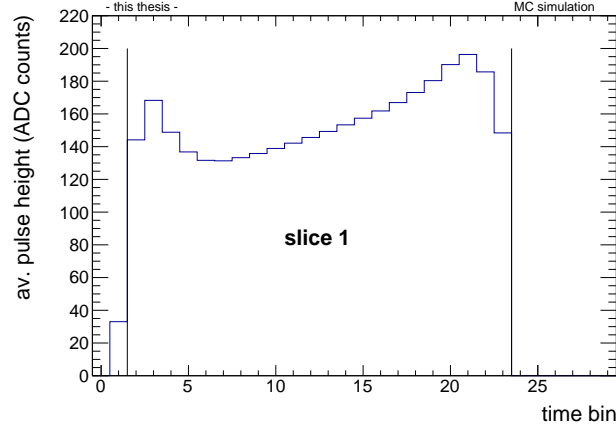
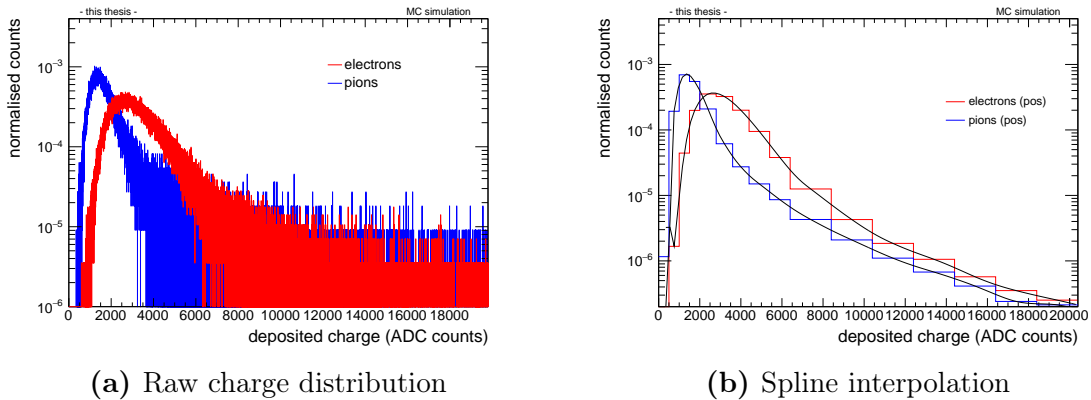


Figure 7.20: Definition of the time interval (marked by the black lines) as used in the LQ1D approach for the online tracklets.

An example of the charge distributions and corresponding spline interpolations is shown (for positively charged tracklets) in Fig. 7.21a and Fig. 7.21b, respectively. The distributions for negatively charged tracklets can again be found in Appendix A.3. For the creation of the LUTs, the same considerations concerning the fluctuations at high and low charges are made as in Section 7.1.1 for the offline information. At the steeply rising flank between deposited charges of about 1000 and 4000, however, the different layers do not coincide as well as in the offline case, as shown in Fig. 7.22a; therefore, this rise is kept for each layer individually, before using the average of all layers at a deposited charge of around 4500. The resulting LUTs are shown in Fig. 7.22b.



(a) Raw charge distribution

(b) Spline interpolation

Figure 7.21: Deposited charge distributions of the positively charged tracklets in layer 0. In (a) the raw charge distribution is shown for both electrons and pions, while in (b), the strongly re-binned distributions with the spline interpolations are depicted.

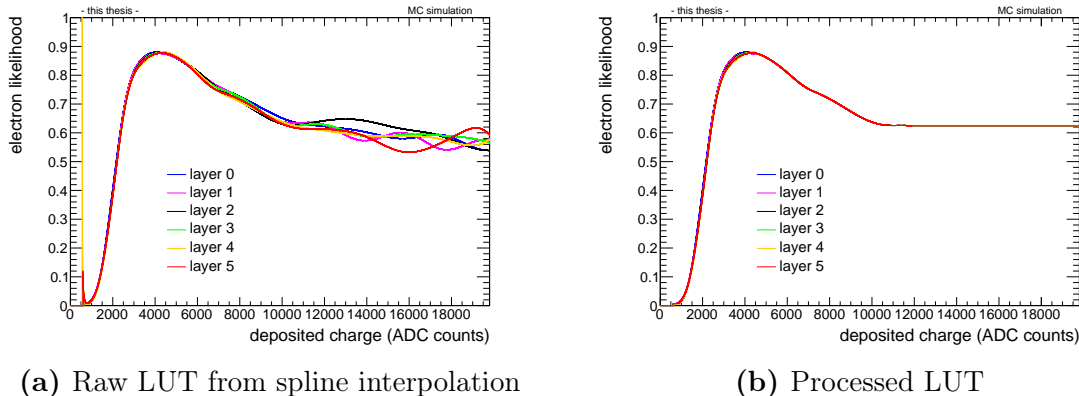


Figure 7.22: Creation of the LUTs using the spline-interpolated charge distributions of positively charged tracklets. The resulting LUTs, shown in (a), are further processed (as detailed in the text) to yield the smooth LUTs in (b).

Following the same procedure as before, the likelihood values are obtained in each layer and combined to yield the total electron likelihood distributions for electrons and pions, which are shown for positively charged tracklets in Fig. 7.23. Compared to the offline distributions in Fig. 7.4, the tracklet distributions show more entries for pions at intermediate to high likelihood values, as well as more entries for electrons at intermediate to low likelihood values. Consequently, the area which contains a certain percentage of the electrons is larger and the pion contamination higher for the tracklets than for the tracks. This can already be seen in Fig. 7.23 for an electron efficiency of 90%, for which the pion efficiency is about a factor 2 larger than for the tracks in Fig. 7.4. It is further confirmed by the results for the different combinations of the LQ1D method and the various bit sizes, which are summarised in Fig. 7.24 and Fig. 7.25 for the online and offline performance, respectively. Several observations can be inferred from these plots:

Firstly, the performance of all bit sizes except for the 6 bits coincides with that of the full information for both tracklets and tracks. This is in any case expected for the samples with 18 and 25 bits, as the full information corresponds to a resolution of approximately 15 bits, meaning that the 18- and 25-bit samples are more granular than the LUTs can resolve. From Fig. 7.24, it can therefore already be concluded that no improvement is gained for the LQ1D method by increasing the size of bits used to store the deposited charge. The case of 6 bits, which is not considered as an option for RUN 3, was included solely with the purpose of illustrating how the performance would deteriorate. Indeed, a clear, although not very large, difference is displayed in all plots of Figs 7.24 and 7.25 between the 6-bit case and the other data points. Therefore, the current implementation in the FEE using 8 bits is already the best option when using only one time slice (corresponding to the LQ1D method).

Secondly, there is a small but visible difference between performances using positively and negatively charged particles, see e.g. Figs 7.24a and 7.24b for the

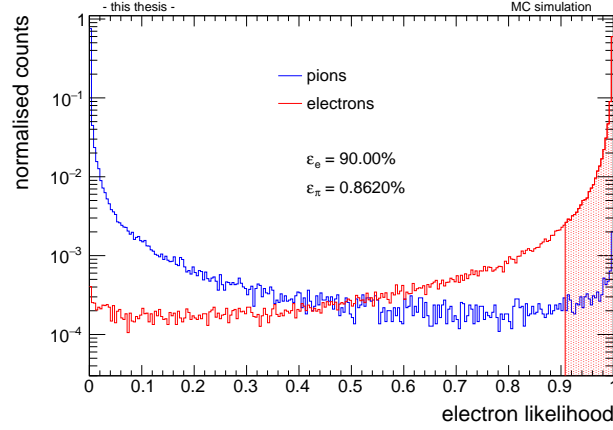
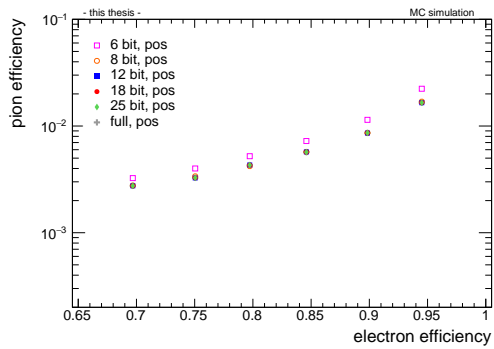


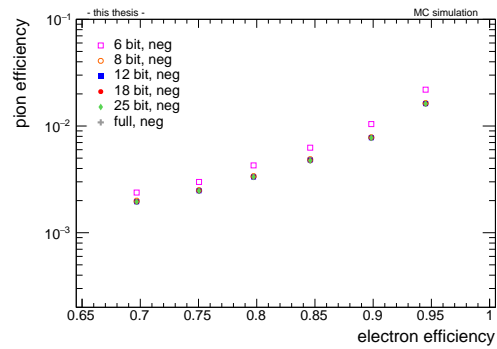
Figure 7.23: Likelihood distributions of electrons and pions for positively charged tracklets. In the shaded area, 90% of the electrons are contained.

online case. This could be caused by the influence of the magnetic field, which affects positively charged particles differently than those with negative charge.

Finally, as already inferred from the likelihood distributions, the performance of the tracks is clearly better than that of the tracklets. At 90% electron efficiency, for example, the pion efficiency of the full online information is worse by about a factor 2 than the efficiency of the full offline information. To gain a better understanding of this discrepancy, the resolution of the deposited charge obtained from the tracks was artificially smeared out to see how this would affect the performance. Indeed, it was found that the pion efficiencies calculated for the smeared offline charge became comparable to the pion efficiencies calculated based on the online tracklets. It seems therefore that the deposited charge which is extracted from the tracklets has a worse resolution than its offline counterpart. It is not entirely clear where this discrepancy comes from; a possible reason could be that deposited charge is processed differently during the offline reconstruction than in the FEE: the calculation of the offline track segments in one chamber is not restricted to only two neighbouring pads, as is the case for the online tracklets (cf. Section 4.4.1); besides, more precise corrections based on calibration measurements can be applied to the offline charge. Furthermore, an additional tail cancellation is applied to reduce correlations between subsequent time bins caused by the long ion tails of the signals. While this is primarily expected to positively affect the position and deflection resolution, it could also have an effect on the PID. Aside from that, the matching of the tracklets to the tracks was shown in Section 6.3.1 to not work perfectly, introducing a contamination by mismatched tracklets, which might deteriorate the charge distributions of electrons and pions (and thus also the LUTs).

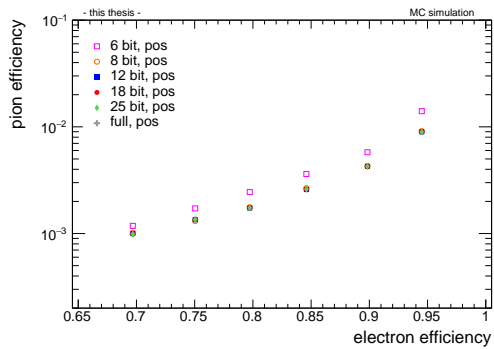


(a) Positively charged particles

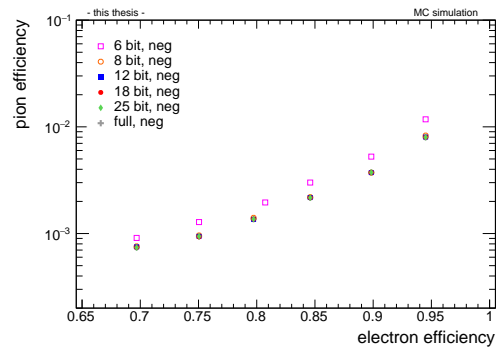


(b) Negatively charged particles

Figure 7.24: Pion efficiency vs electron efficiency calculated with the LQ1D method using the online tracklets as input, (a) for positively charged tracklets, (b) for negatively charged tracklets.



(a) Positively charged particles



(b) Negatively charged particles

Figure 7.25: Pion efficiency vs electron efficiency calculated with the LQ1D method using the offline tracks as input, (a) for positively charged tracks, (b) for negatively charged tracks.

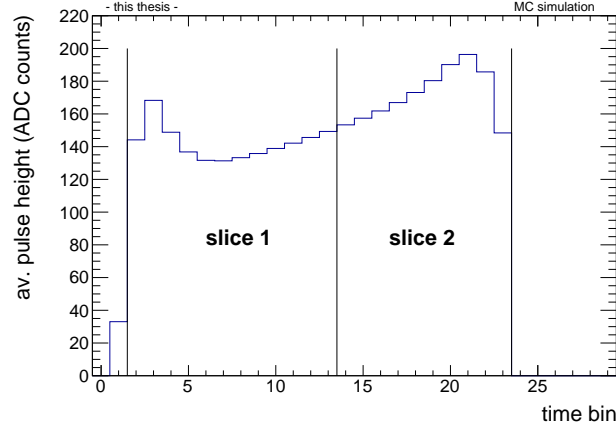


Figure 7.26: Definition of the two time intervals used in the LQ2D method for the online tracklets.

LQ2D

For the two-dimensional likelihood approach, the charge in the tracklet clusters is distributed in two slices. In analogy to the offline case (where the first four and the last three of the seven slices are combined), the 22 time bins are divided into intervals of 12 and 10 time bins, as shown in Fig. 7.26. The resulting charge distributions of electrons and pions are sketched in Fig. 7.27 for positively charged tracklets (in one layer). As in the offline case, the influence of the absorbed TR is clearly visible in the charge distribution of the electrons in the second slice, which exhibits a peak broadened to higher deposited charges. The distributions of the pions, on the other hand, remain similar in both slices. This behaviour is reflected in the LUTs, which are again created from spline interpolations and further processed as described in the previous section. While the LUTs in the first slice (Fig. 7.28a) reach a likelihood value of ~ 0.82 at most, the maximum of the LUTs in the second slice (Fig. 7.28b) is ~ 0.9 , since the separation of the distributions of electrons and pions is improved with respect to slice 1 due to the additional TR contribution.

The full charge information in the clusters is now transformed into the various bit sizes, which were defined in Table 7.1 for the LQ2D method. In this process, even bit sizes are divided equally (i.e. in the 8-bit case, 4 bits are allocated to each slice), while for the only odd bit size of 25 bits, 13 bits are distributed to slice 1 and 12 bits to slice 2.

Subsequently, the pion efficiency is determined for the different electron efficiencies. The results are shown for the tracklets in Fig. 7.29, again separated by charge. There is a clear discrepancy between the performance of the full information and that of the 8-bit case, which is about a factor 6 worse. There is also a visible difference between the 12 bits and the full information; the performance of all other bit sizes coincides again with the limit of the full information. Using this limit to judge the

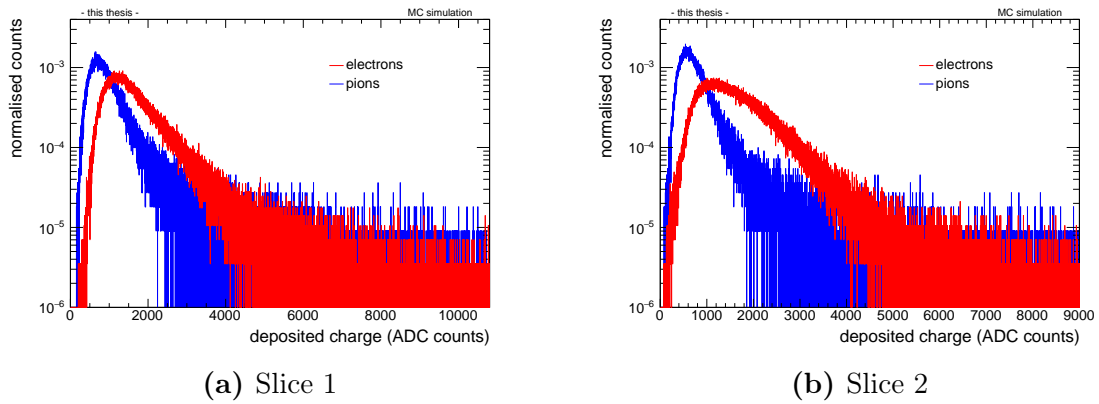


Figure 7.27: Charge distribution of positively charged tracks in layer 0, (a) in slice 1, and (b) in slice 2, as used for the LQ2D method.

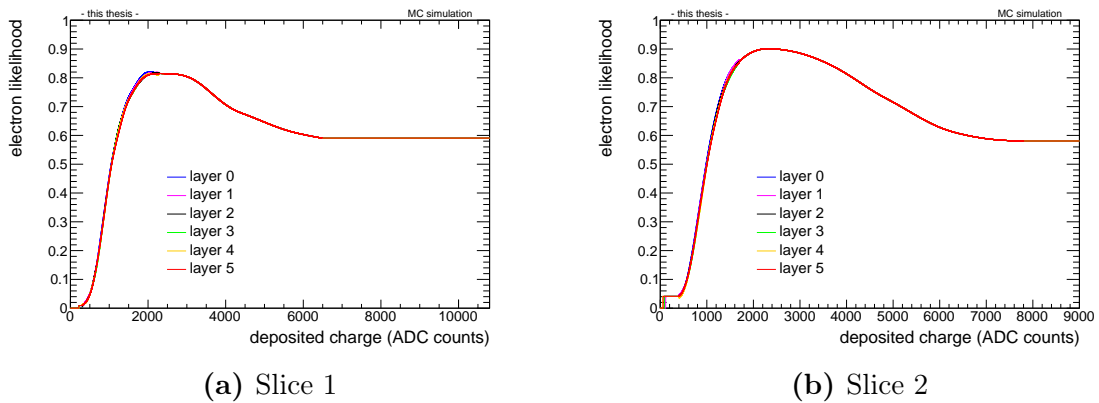


Figure 7.28: LUTs for positively charged tracklets, (a) in slice 1, and (b) in slice 2, as used in the LQ2D method.

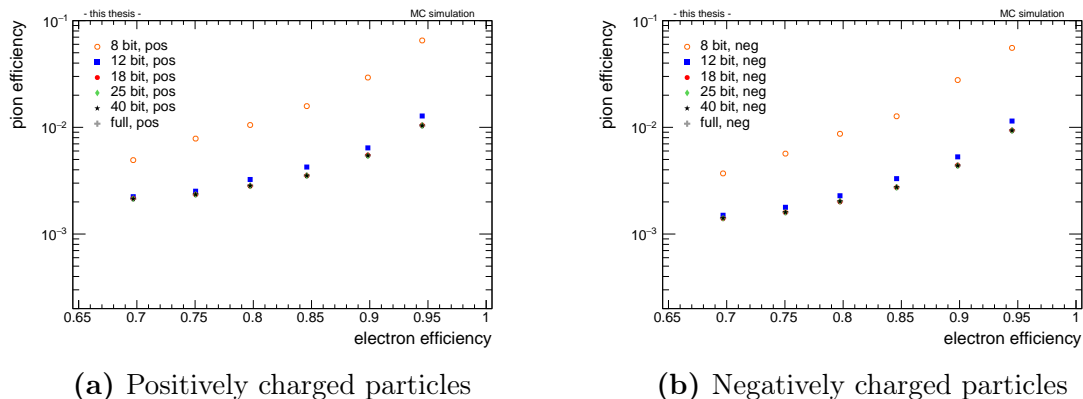


Figure 7.29: Pion efficiency vs electron efficiency calculated with the LQ2D method, (a) for positively charged tracklets, (b) for negatively charged tracklets.

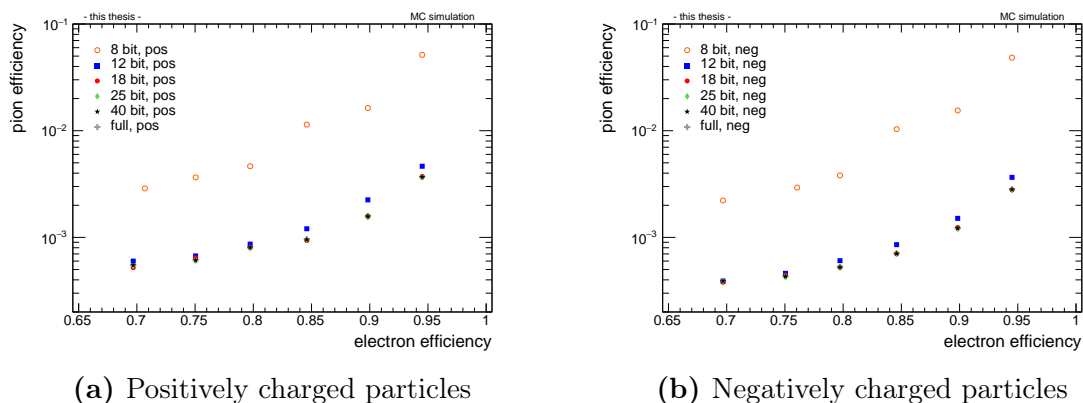


Figure 7.30: Pion efficiency vs electron efficiency calculated with the LQ2D method, (a) for positively charged tracks, (b) for negatively charged tracks.

improvement of the LQ2D method with respect to the LQ1D approach, the LQ2D performance is better by a factor of ~ 1.6 – 1.8 (for 90% electron efficiency).

Qualitatively, the same statements can be made for the tracks in Fig. 7.30. Quantitatively, however, the difference between 8 bits and full information is even larger, amounting to roughly one order of magnitude. Furthermore, the discrepancy of online and offline performance is again clearly visible, and with a factor of ~ 3.5 even larger than for the LQ1D case. This comes about as the improvement of the LQ2D method with respect to the one-dimensional approach is about a factor of 3 for the tracks, and therefore larger than for the tracklets.

LQ3D

To calculate the PID performance of the tracklets with the three-dimensional likelihood approach, the 22 time bins are first split into three slices of 9, 6, and 7 time bins, respectively (sketched in Fig. 7.31). This was chosen to reflect the distribution of

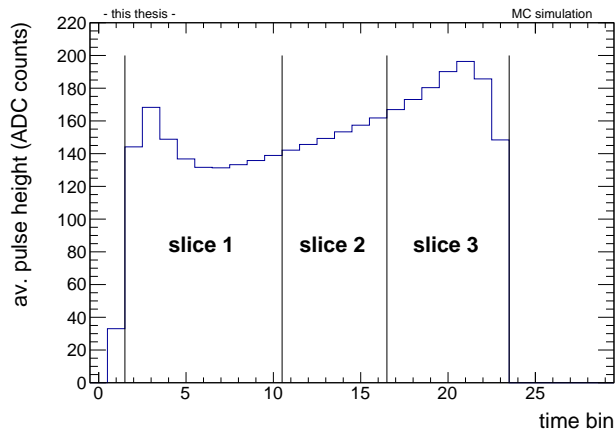


Figure 7.31: Definition of the three time intervals used in the LQ3D method for the online tracklets.

3—2—2 slices in the offline case. For the tracklets, one more time bin was allocated to slice 3 compared to slice 2 to ensure that the TR peak is contained in the last slice.

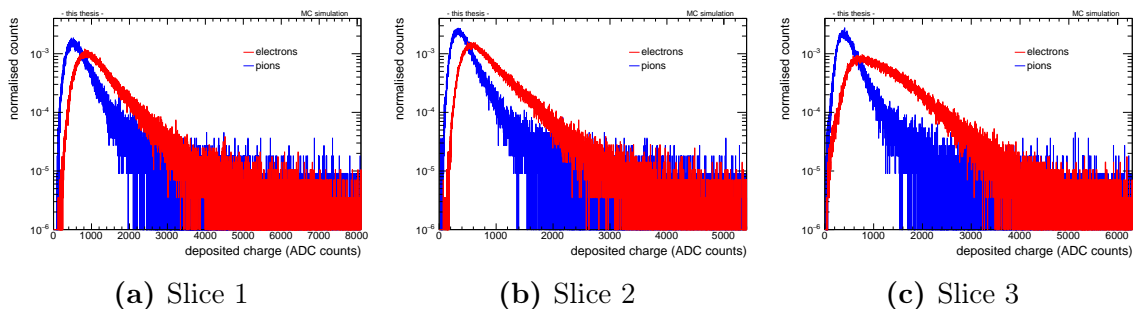


Figure 7.32: Charge distribution of positively charged tracklets in layer 0, (a) in slice 1, (b) in slice 2, and (c) in slice 3, as used for the LQ3D method.

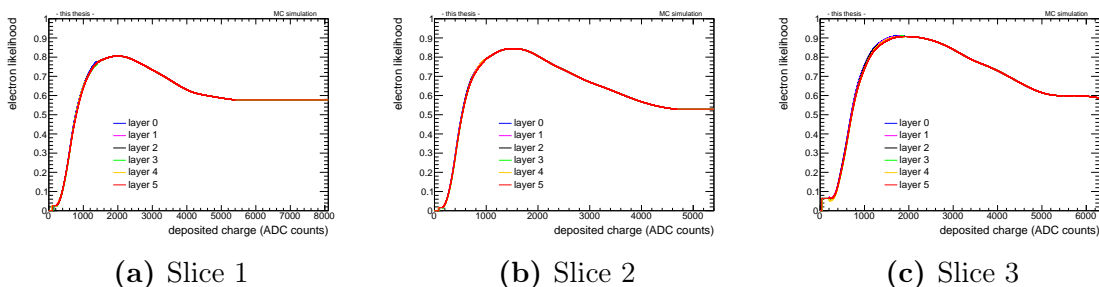


Figure 7.33: LUTs for positively charged tracklets, (a) in slice 1, (b) in slice 2, and (c) in slice 3, as used in the LQ3D method.

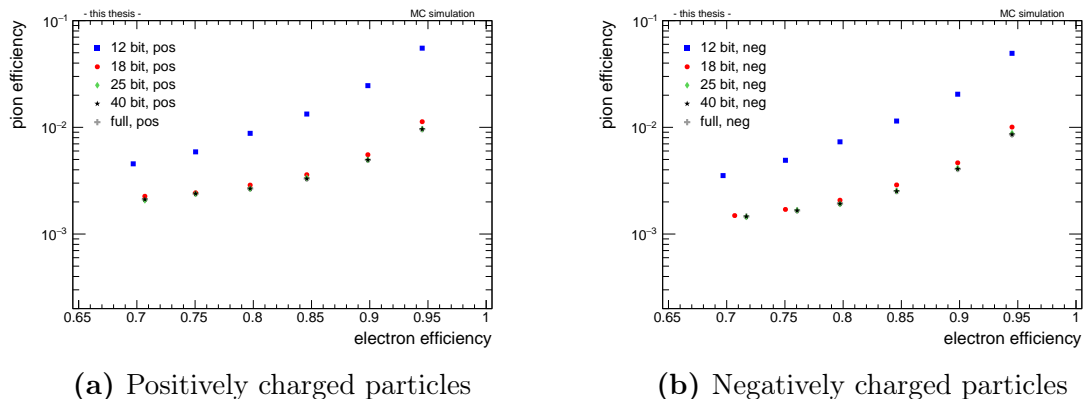


Figure 7.34: Pion efficiency vs electron efficiency calculated with the LQ2D method, (a) for positively charged tracklets, (b) for negatively charged tracklets.

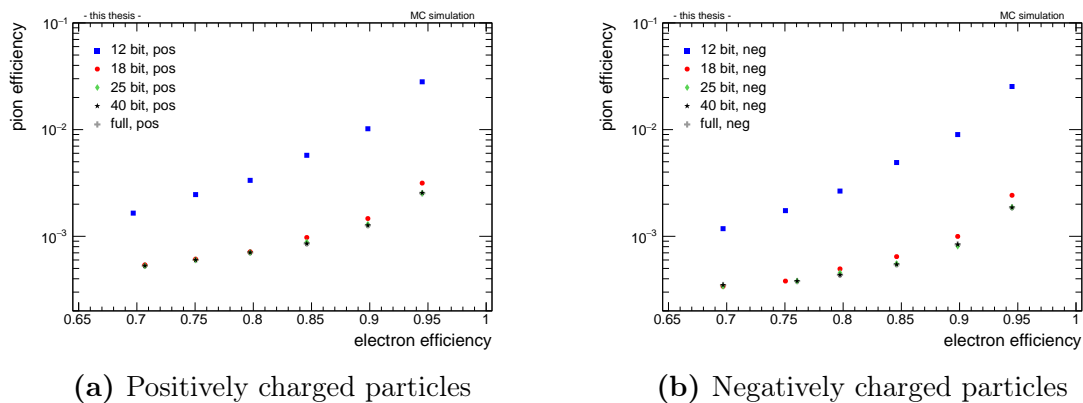


Figure 7.35: Pion efficiency vs electron efficiency calculated with the LQ3D method, (a) for positively charged tracks, (b) for negatively charged tracks.

The charge distributions in the three slices, depicted in Fig. 7.32 (for positively charged tracklets in one layer), show the same behaviour as their offline counterparts, i.e. similar charge distributions of the pions in all three slices, and clear changes in the distributions of the electrons due to the influence of the TRD contribution. The LUTs calculated from the spline interpolations are shown in Fig. A.34; here, too, the maximum value of the LUTs increases with the higher slice number, as the separation of electrons and pions due to TR improves.

For the transformation of the full charge to the different bit sizes, the bits are distributed equally into the three slices in the case of 12 and 18 bits. For the 25-bit case, 9 bits are allocated to slice 1, and 8 bits to slices 2 and 3, respectively. Analogously, the 40 bits are split up into 14, 13, and 13 bits. The resulting pion efficiencies are shown in Fig. 7.34a and Fig. 7.34b for positively and negatively charged tracklets, respectively. Similarly to the combination of the LQ2D method and 8 bits, the performance of the 12-bit scenario is worse by a factor of ~ 6 compared

to the full information. Additionally, there is a small but visible difference between the 18-bit case and the higher bit values, which have reached the limit of the full information. Relative to the LQ2D approach, there is very little improvement: the performance using the full cluster charge with the LQ3D method is only better by a factor ~ 1.1 (for both positive and negative charge). Finally, the electron efficiencies around 70% and 75% deviate noticeably from their target values, in particular for the negatively charged tracklets in Fig. 7.34b. These can be traced back to the shift of the likelihood distributions to 0 and 1, as already previously observed in Section 7.1.2 for the offline tracks.

For the performance of the offline tracks using the LQ3D approach, shown in Fig. 7.35, similar observations as for the LQ2D method can be made: the difference of the pion efficiencies (at 90% electron efficiency) of the worst case (12 bit) and the limit of the full information is about one order of magnitude. Furthermore, the improvement of the LQ3D method with respect to the LQ2D approach is with a factor of ~ 1.3 again better than in the online case; this is also reflected in the difference between the online and offline performance of the full information, which amounts to a factor 4–5 (as opposed to the LQ2D method, where they differed by about a factor of 3.5).

Comparisons

To compare the results of the tracklet-based PID performance in a more comprehensive manner, the pion efficiencies of all data samples listed in Table 7.1 are shown in Fig. 7.36 as a function of the bit size (separated by charge). The performance obtained with the full cluster information is added in the form of three lines (one for each dimensionality of the likelihood method).

The following observations can be made concerning the number of bits available for one slice: if 4 bits are allocated per slice (2D/8 bits or 3D/12 bits), the performance is significantly worse than the performance of the full information. For 6 bits per slice (1D/6 bits; 2D/12 bits; 3D/18 bits), the resulting pion efficiency clearly improves and is already close to that of the full information. Finally, for bit sizes of 8–9 bits per slice (1D/8 bit; 2D/18 bit; 3D/25 bit), the performance reaches the limit, and accordingly does not improve anymore if the bit size is further increased. It can therefore be concluded that a size of 8–9 bits per slice is already enough to obtain the same performance as in the case of the full information when using the linear transformation function. For the non-linear transformation function, even less bits per slice need to be allocated, as will be shown in the following section.

In Fig. 7.37, the pion efficiencies determined for the full charge information of the tracks are added as black lines for the three likelihood methods. Again, the difference between online and offline performance becomes clear; here, further investigation will be necessary to understand these discrepancies. The same applies for the improvement of the performance when going from one to higher likelihood dimensions, which is much more pronounced for the offline tracks than for the online tracklets.

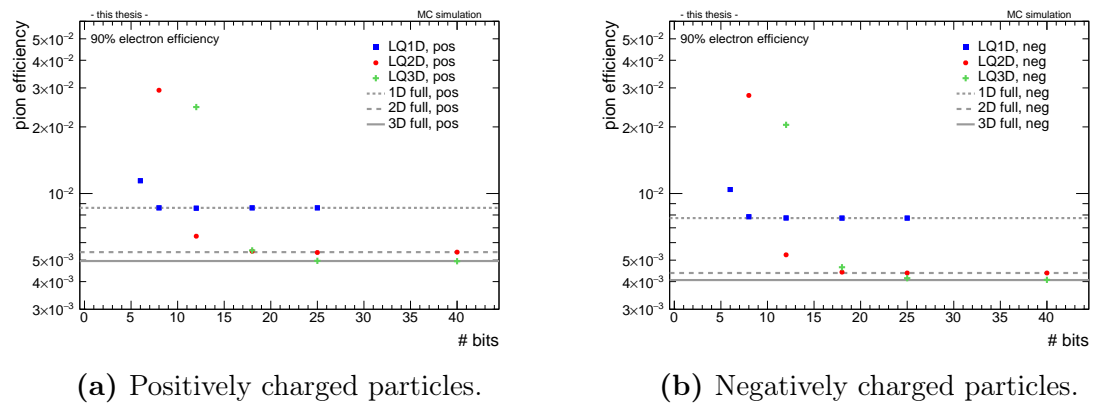


Figure 7.36: Pion efficiency of the tracklet samples vs number of bits, using the linear transformation function. In addition to the data points corresponding to the combination of likelihood dimensionality and bit size, the full information for all three likelihood approaches is drawn as grey lines.

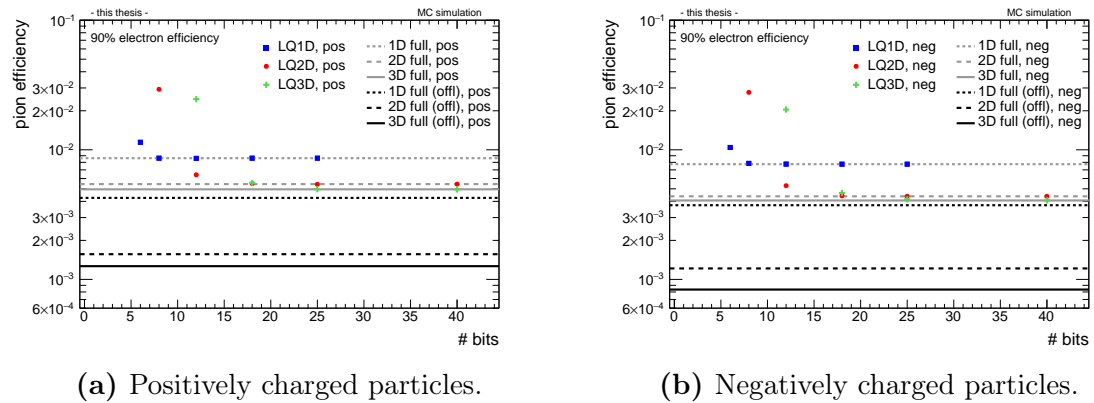


Figure 7.37: Pion efficiency of the tracklet samples vs number of bits, using the linear transformation function. In addition to the full information of the tracklets (grey lines), the full track information is added (black lines).

7.3.3 Performance using the non-linear function

For the transformation with the non-linear function, the analysis is performed analogously. Only the binning of the LUTs has to be changed to reflect the increase in granularity in the overlap region of the electron and pion distributions, and the decrease in the region of high deposited charge. Thus, only the final results for the LQ1D, LQ2D, and LQ3D method, as well as the final comparison of all performances at 90% electron efficiency are discussed in the following paragraphs.

LQ1D

Figures 7.38a and 7.38b show the performance of the LQ1D method for the 6-, 8-, 12-, 18-, and 25-bit scenarios, as well as the full information of the tracklets. The effect of the non-linear transformation function becomes immediately clear when comparing the 6 bit-performance in both figures with that in Figs. 7.24a and 7.24b: while there was a clear difference between 6 bits and all other samples for the linear function, now the performances are overall very similar. This is a first indication of the improvement which can be gained for small bit numbers by choosing a suitable transformation function. For bit sizes larger than 6 bit, the performance is already saturated, and cannot be further improved with respect to the full information. The performance of the offline tracks, shown in Fig. 7.39, exhibits in that respect the same behaviour as the online tracklets. As the efficiency obtained for the full charge information remains unchanged for both transformation functions, the observations concerning the difference between online and offline performance made in Section 7.3.2 still hold true.

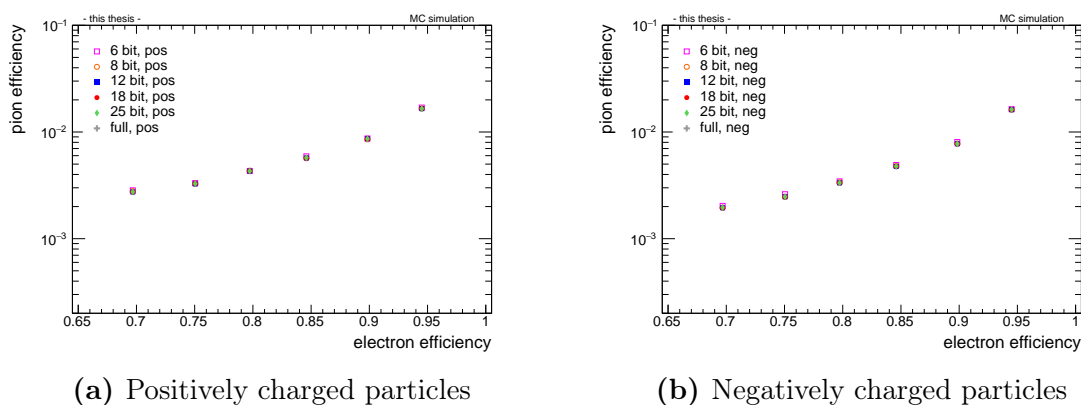


Figure 7.38: Pion efficiency vs electron efficiency calculated with the LQ1D method, (a) for positively charged tracklets, (b) for negatively charged tracklets. For the bit-transformation, the non-linear function is used.

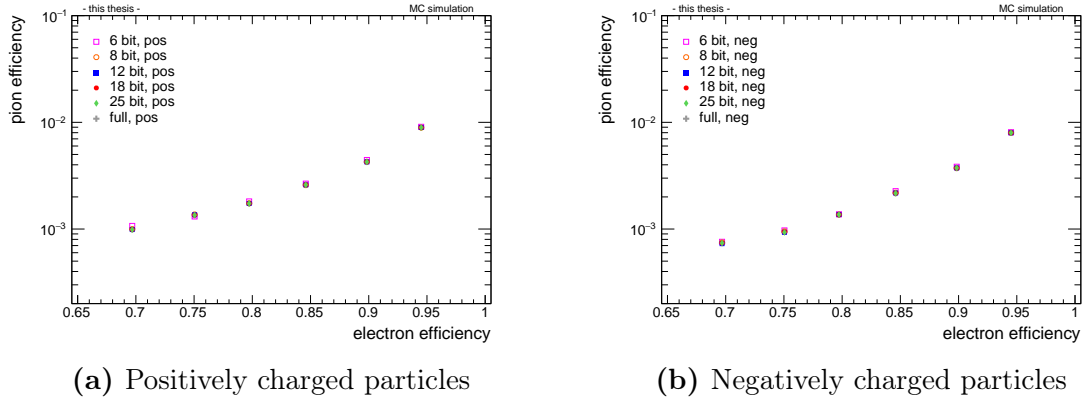


Figure 7.39: Pion efficiency vs electron efficiency calculated with the LQ1D method, (a) for positively charged tracks, (b) for negatively charged tracks. For the bit-transformation, the non-linear function is used.

LQ2D

The improvement of the non-linear transformation function becomes even more evident when comparing the performances of the various LQ2D/ n bit combinations in Fig. 7.40 (online) and in Fig. 7.41 (offline) to their counterparts in Figs 7.29 and 7.30. In the 8-bit case, the pion efficiency decreases dramatically, in particular for high electron efficiencies. For example at $\varepsilon_e = 90\%$, the performance of the tracklets improves approximately by a factor of 6, while for the tracks, an improvement of about one order of magnitude is observed (for both positive and negative charge, respectively). Furthermore, there is also an improvement, if not quite as distinct, of the 12-bit performance, which now coincides with the performances of the larger bit sizes and the full information.

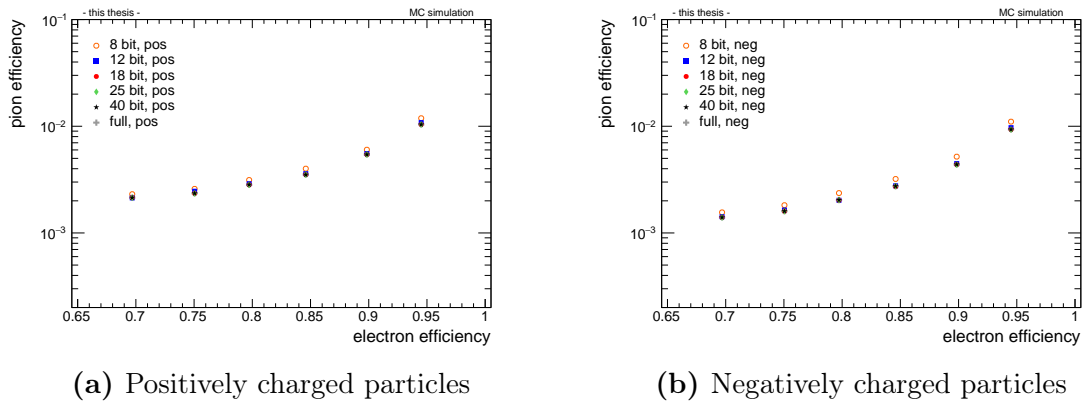


Figure 7.40: Pion efficiency vs electron efficiency calculated with the LQ2D method, (a) for positively charged tracklets, (b) for negatively charged tracklets. For the bit-transformation, the non-linear function is used.

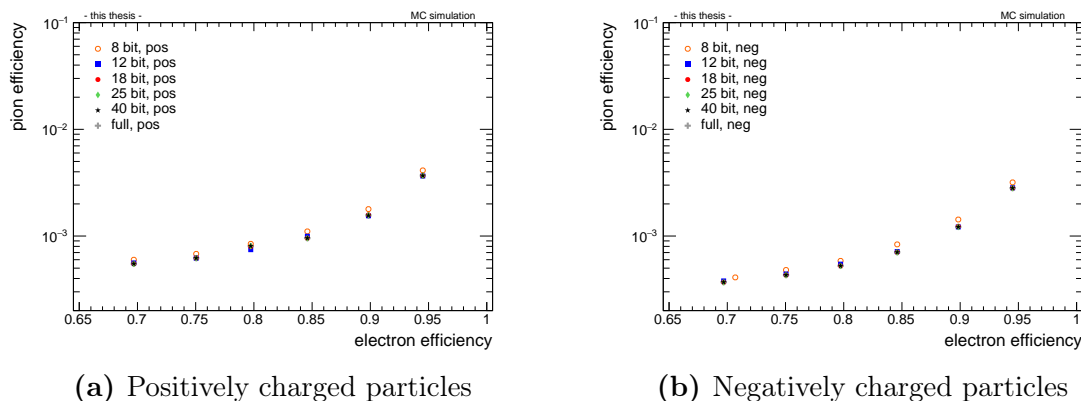


Figure 7.41: Pion efficiency vs electron efficiency calculated with the LQ2D method, (a) for positively charged tracks, (b) for negatively charged tracks. For the bit-transformation, the non-linear function is used.

LQ3D

For the LQ3D method, similar observations are made concerning the improvement of the performance using small bit sizes: as the comparison of the tracklet-based PID in Fig. 7.42 and Fig. 7.34 demonstrates, the pion efficiency of the 12-bit sample decreases by a factor 5–6 for an electron efficiency of 90%. Similarly, an improvement of an order of magnitude is illustrated for positively as well as negatively charged tracks in Fig. 7.43 when compared to Fig. 7.35. For both offline and online PID, the performance of the 18-bit sample reaches the limit of the full information.

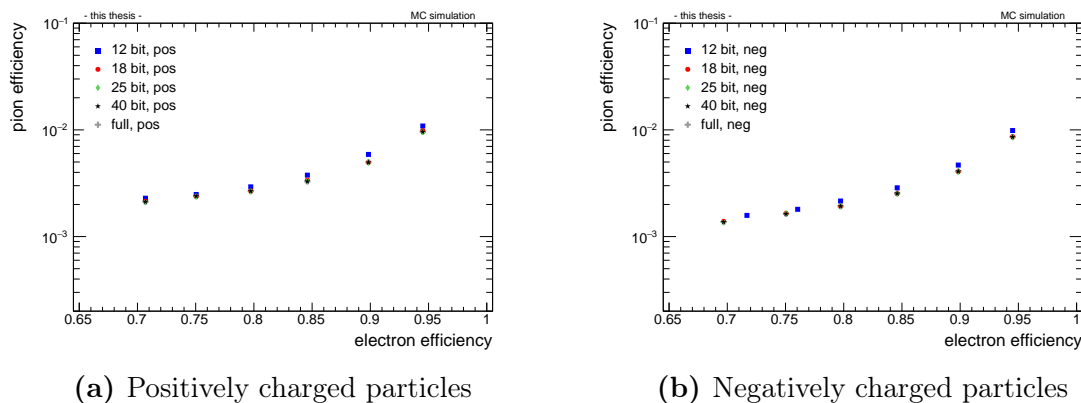


Figure 7.42: Pion efficiency vs electron efficiency calculated with the LQ3D method, (a) for positively charged tracklets, (b) for negatively charged tracklets. For the bit-transformation, the non-linear function is used.

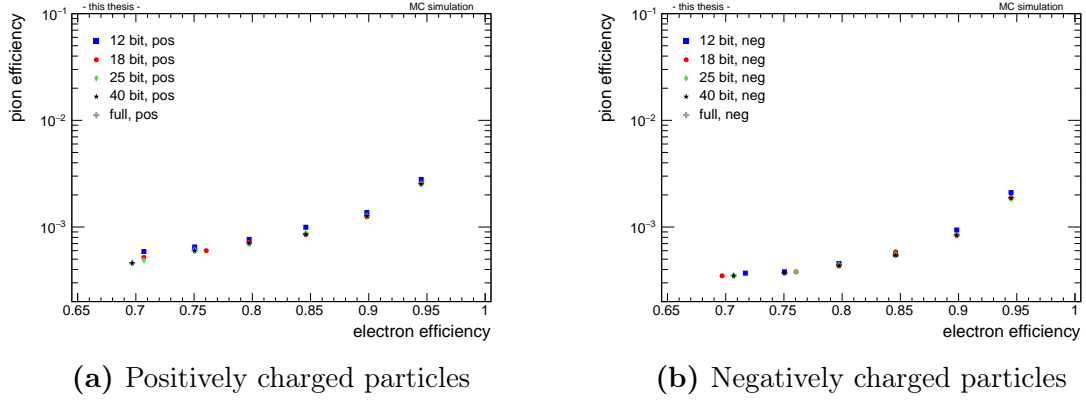


Figure 7.43: Pion efficiency vs electron efficiency calculated with the LQ3D method, (a) for positively charged tracks, (b) for negatively charged tracks. For the bit-transformation, the non-linear function is used.

Comparisons

Finally, the pion efficiencies at 90% electron efficiency are compared for all combinations of dimensionality and bit sizes. The striking improvement of the small bit sizes using the non-linear transformation function, which was already discussed in the previous sections, is again evident for both positively and negatively charged tracklets in Figs 7.44a and 7.44b. Almost all data samples have reached the limit of the full information marked by the grey lines, with only the “worst cases” of 8 bit for the LQ2D method and 12 bit for the LQ3D method yielding pion efficiencies slightly above. Therefore, the best possible performance can already be achieved using 18 bits for the tracklet-based PID by choosing a suitable transformation function. The conclusions drawn from the investigations discussed above will be presented in the next chapter in the form of a proposal of implementation for the FEE in RUN 3.

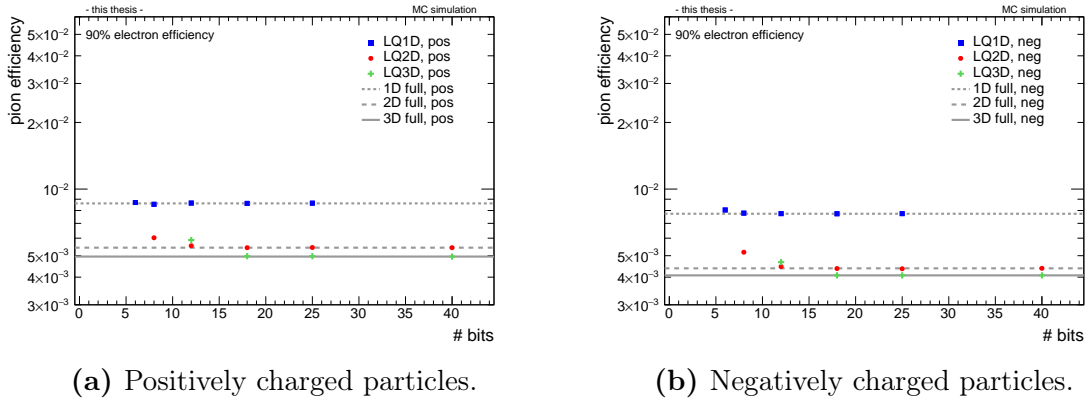


Figure 7.44: Pion efficiency of the tracklet samples vs number of bits, using the non-linear transformation function. Again, the full information for all three likelihood approaches is added as grey lines.

Chapter 8

Proposal for implementation

Within the scope of this thesis, the PID performance using the online tracklet information was investigated depending on three variables: the amount of bits to store the deposited charge in the tracklet word (also referred to as the “bit size”), the number of time slices in which the charge is accumulated (determining the dimensionality of the likelihood method), and the function to be used in the TRAP to transform the deposited charge from the full resolution to the resolution of the bits. The combinations of these three parameters best suited for the implementation in the FEE for RUN 3 will be presented in this chapter. In the following paragraphs, each parameter will be discussed shortly, before a final conclusion is drawn.

Likelihood dimensionality

As the analysis presented in Chapter 7 showed, the performance can be clearly improved by using a higher-dimensional likelihood method. Using the full information on the cluster charge (that is, without any bit transformation), the pion efficiency at 90% electron efficiency is decreased by a factor ~ 1.6 (~ 1.8) for positively (negatively) charged tracklets when using the two- instead of the one-dimensional likelihood approach. The improvement of the performance when applying the three- instead of the one-dimensional likelihood amounts to a factor ~ 1.7 (~ 1.9) for positively (negatively) charged particles. This is once more illustrated in Fig. 8.1, which summarises the performance of the different parameter sets for positively charged tracklets.

It must, however, be taken into account that for small bit sizes, the higher-dimensional likelihood methods yield a performance which is worse than the one-dimensional approach, when used in combination with the linear transformation function (cf. Fig. 8.1a). With the 8 bits currently in use, for example, the LQ2D method would lead to a clear deterioration of the pion efficiency. In this case, the charge in each of the two slices only has a resolution of 4 bits, which is not enough to effectively distinguish electrons from pions using the linear function. With the non-linear transformation function optimised for electron/pion separation, on the other hand, this situation is greatly improved, as a comparison of Fig. 8.1a and Fig. 8.1b shows. Furthermore, for bit sizes which result in at least 8 bits per slice (e.g. LQ1D/8 bits; LQ2D/18 bits; LQ3D/25 bits), the performance using either transformation function reaches its maximum, given by the pion efficiency of the cluster charges with full resolution.

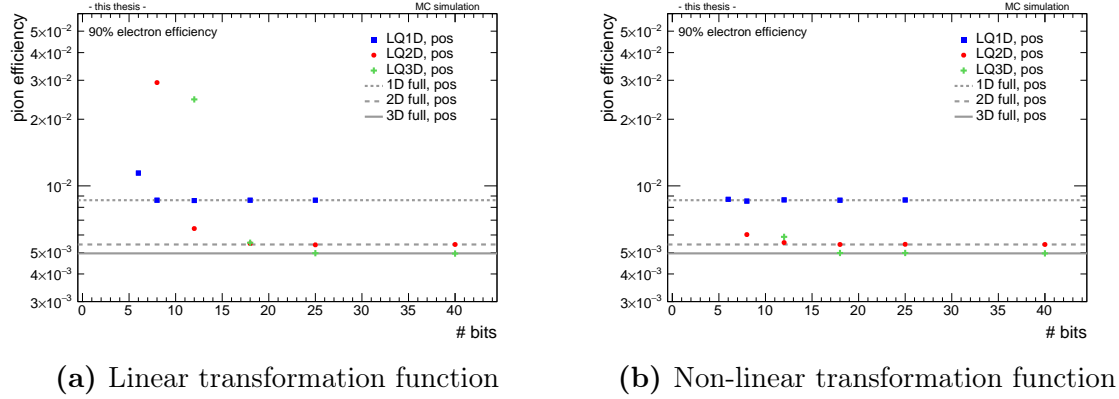


Figure 8.1: Pion efficiency of the positively charged tracklets vs number of bits. In (a), the linear transformation function is used, while (b) shows the performance with the non-linear function. The performance of the clusters with the full resolution is added as lines for the three likelihood methods.

In summary, it can therefore be inferred from Fig. 8.1 that the two- and three-dimensional likelihood methods are preferable to the LQ1D approach, provided that the bits size is large enough and/or the non/linear transformation function is used.

Another point to consider is the actual implementation in the FEE: the use of two time windows instead of one to accumulate the deposited charge is included in the TRAP programme already now. The sum of the deposited charge could also be calculated in three time windows by looping over the event data in the CPUs; this is however not implemented yet, and would thus require further work and manpower. As there is only little improvement of the performance when using the LQ3D method relative to the LQ2D method, the two-dimensional approach is favoured for RUN 3.

Transformation function

As the comparison of Fig. 8.1a and Fig. 8.1b demonstrates, the use of the non-linear transformation function greatly improves the performance of small bit sizes in combination with the two- or three-dimensional likelihood method. However, no decrease in the pion efficiency can be achieved for larger bit sizes (i.e. those which result in least 8 bits per slice depending on the likelihood dimensionality), since the performance of these samples has already reached the limit of the full resolution when using the linear transformation function. The same holds true for the LQ1D approach, where no improvement of the performance can be gained by using the non-linear instead of the linear transformation function. The actual implementation in the FEE is the same for both functions.

Number of bits

To discuss the number of bits ideally used in RUN 3, the number of tracklets per MCM must first be considered. In the current implementation of the FEE, four

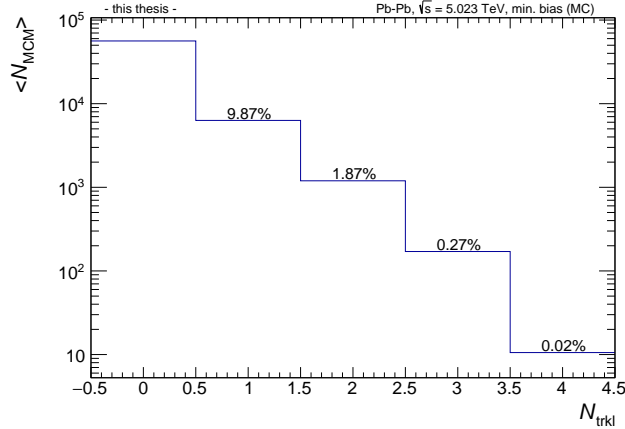


Figure 8.2: Number of tracklets calculated per MCM. The y axis shows the average number of MCMs per event which calculated N_{trkl} tracklets. In this plot, data from minimum-bias Pb–Pb collisions at $\sqrt{s_{\text{NN}}} = 5.023$ TeV, which were re-simulated to include the double-tracklet suppression in the MCMs, are used.

tracklets can be calculated in parallel at most (see Section 4.4); if 18 bits were to be used, the number of tracklets per MCM would be reduced to three; and if the PID storage size were chosen to be 40 bits, only two tracklets could be processed per MCM.

To quantify how many tracklets are actually calculated in the MCMs in real collisions, and how many would be lost when giving up one or two tracklets per MCM, minimum-bias Pb–Pb collisions at $\sqrt{s_{\text{NN}}} = 5.023$ TeV recorded in 2015 are analysed. The data are re-simulated first to suppress the double tracklets (cf. Sec. 6.3.4), since the double-tracklet rejection in the MCMs will be used in RUN 3, but is not yet implemented in the FEE. Subsequently, the number of tracklets which were calculated in each MCM are counted. The result is illustrated in Fig. 8.2, which shows the average number of MCMs calculating 0, 1, ..., 4 tracklets per event. In more than 97% of the almost 64 000 MCMs, not more than one tracklet is calculated on average per event. The extreme case of four tracklets, on the other hand, is only calculated in about ten MCMs on average, i.e. in 0.02% of all MCMs. If only those instances are considered where at least one tracklet is found, the four-tracklet case accounts for $\sim 0.14\%$ of the MCMs. Thus, four tracklets are calculated so rarely that reducing the number of tracklets per MCM from four to three should still be tolerable. Processing only two tracklets per MCM might be more problematic, as the three- and four-tracklet cases account for $\sim 2.36\%$ of all instances where at least one tracklet is processed (and for $\sim 0.29\%$ of all MCMs).

Following these considerations, the performance achieved with the different bit sizes is now taken into account: as Fig. 8.1 illustrates, the increase in bit size positively affects the pion efficiency calculated with both the two- and the three-dimensional likelihood approach. In combination with the non-linear transformation function, 12

bits are already enough to reach the maximal performance of the LQ2D method; the same applies to 18 bits and the LQ3D method. Therefore, neither 25 nor 40 bits are needed to achieve the best performance which is possible with the approaches introduced in this thesis. This coincides well with the observations concerning the number of tracklets per MCM made above: even if the LQ3D method were to be used, only 18 bits would be needed, corresponding to the loss of only one tracklet per MCM, which should be acceptable.

Conclusions

Taking all considerations made above into account, the easiest implementation which would still deliver acceptable results is the combination of the two-dimensional likelihood method, 12 bits of storage size for the deposited charge and a non-linear transformation function. Using these settings, a pion efficiency of $\sim 5.4 \cdot 10^{-3}$ and $\sim 4.4 \cdot 10^{-3}$ is achieved at 90% electron efficiency for positively and negatively charged tracklets, which is still well below the original TRD design goal of a pion efficiency of 10^{-2} for 90% electron efficiency [22].

Another option to be considered is the setting of the three-dimensional likelihood approach, together with 18 bits and the non-linear transformation function. This combination yields slightly better pion efficiencies of $\sim 5.0 \cdot 10^{-3}$ and $\sim 4.1 \cdot 10^{-3}$ at 90% electron efficiency for positively and negatively charged tracklets, but comes with the drawback that the three time windows for the charge accumulation would have to be implemented in the electronics first. In addition, one tracklet per MCM has to be given up in order to have 18 bits available for storage in the tracklet word; however, it was shown that this would affect only a negligibly small amount of tracklets.

To gain 12 bits for the PID storage, on the other hand, it could be considered to reduce the 7 bits for the deflection to 3 bits. This would allow to keep the maximum of four tracklets per MCM at the cost of a lower granularity of the deflection. At the time of this thesis, it is not yet clear whether a high granularity is needed. If the low granularity of 3 bits turns out to be not enough, one tracklet per MCM has to be given up for the 12 bits as well; the remaining leftover bits could then be used to increase e.g. the position resolution, if this proves to be beneficial for the tracking. In the end, the decision on what to implement will thus also depend on the requirements on the tracking with the TRD in RUN 3.

Chapter 9

Summary and outlook

In the third run period of the LHC, RUN 3, collisions of Pb ions at a rate of 50 kHz are foreseen. To cope with these high rates, the mode of operation of the TRD, which was originally designed for collisions at 8 kHz, must be adapted. The proposed strategy is to read out the online tracklets, which are processed in the FEE directly installed on the read-out chambers, instead of the raw data. As the identification of electrons via TR is one of the purposes of the TRD, it must be ensured that an adequate PID performance using the online tracklets can still be achieved with respect to the current performance, which is based on the raw data.

Over the course of this thesis, the framework for the analysis and evaluation of the PID performance using online tracklets was developed. To investigate the PID performance, a MC simulation was produced specifically for this thesis, and subsequently analysed depending on different tunable parameters, leading to a proposal for the operating mode of the FEE in RUN 3.

The analysis presented in this thesis was split into two parts: in the first part, implemented as a dedicated offline analysis task, offline tracks were first processed to select only electrons and pions originating from the primary vertex, which furthermore had an average momentum larger than $0.9 \text{ GeV}/c$ in the six layers of the TRD. Subsequently, tracklets were matched to these tracks in every layer based on their spatial difference. Various matching window sizes were investigated with the help of the MC truth information available for both tracks and tracklets in order to keep the number of wrongly matched tracklets small, while at the same time ensuring a high matching efficiency. In the end, a matching window of $\Delta y = 1 \text{ cm}$ and $\Delta z = 9 \text{ cm}$ was chosen. The clusters used to calculate the tracklets, which were stored in a dedicated file during the simulation, were then extracted and processed for all matched tracklets: double tracklets were rejected, and tracklets split over two pad rows were merged. Additionally, an η -dependent length correction was applied to the deposited charge stored in the clusters.

In the second part of the analysis, the multi-dimensional likelihood method was introduced for one, two, and three dimensions using the charge obtained from the offline tracks. Subsequently, the data samples to be analysed were defined. They each consisted of a combination of likelihood dimensionality (1D, 2D, or 3D) and one of various bit sizes, which were considered for the PID storage in the tracklet word. To avoid having to produce a new simulation for each data sample, the deposited charge in the tracklet clusters was transformed to the bits in question instead. For

this transformation, both a linear and a non-linear function were available, with the non-linear function chosen such that the separation region of electrons and pions was attributed a high granularity. Finally, the actual evaluation of the tracklet-based PID performance was carried out using the charge in the clusters of the tracklets, as well as the deposited charge of the matched tracks as reference. To quantify the PID performance, the pion efficiency was calculated for electron efficiencies between 70% and 95%. Furthermore, the pion efficiencies at 90% electron efficiency were compared for the different data samples as a function of the amount of bits. As a reference, the performance using the full cluster charge information, which poses the limit of the achievable pion efficiency, was added as well. For sufficiently large bit sizes resulting in at least 8 bits per slice (e.g. 18 bits for the LQ2D method, or 25 bits for the LQ3D method), the same performance could be achieved as for the full information when using the linear transformation function. In addition, the use of the non-linear transformation function also strongly improved the performance of the LQ2D and LQ3D methods for small bit sizes. In general, a clear decrease of the pion efficiency could be observed for the higher-dimensional likelihood methods.

As a conclusion, the combination of the two-dimensional likelihood method with 12 bits of storage for the deposited charge and using the non-linear transformation function were proposed for the implementation in the FEE for RUN 3. Another option could be the setting of the three-dimensional likelihood method with 18 bits and the non-linear transformation function, provided there is manpower available to implement the accumulation of the charge in three time windows in the FEE. Both options would require to give up at most one of the four tracklets which can be calculated in parallel per MCM. For a data sample obtained in minimum-bias Pb–Pb collisions at $\sqrt{s_{\text{NN}}} = 5.023$ TeV, the case of actually processing four tracklets per MCM in one event was shown to account for only $\sim 0.02\%$ of all MCMs, and thus to be negligible.

Further steps could now include the fine-tuning of the suggested parameters: the non-linear transformation function, for example, could be optimised to best exploit the charge range where the separation of electrons and pions is most crucial. In addition, the splitting of the bits for the LQ2D and LQ3D methods could be further improved, for example by assigning a larger number of bits to the last slice, which contains the TR peak of the electron charge distribution. Furthermore, a more in-depth investigation into the difference between the online and offline performance could prove to be instructive.

Finally, the proposed settings could be tested by implementing them in the TRAP simulation, which could either be run on a realistic MC production, or directly on real data. The filtering of interesting events (in particular those including electrons to increase the statistics) of data from p–Pb collisions in 2016, which could be used for this purpose, is currently in preparation.

Appendix A

Tracklet-based PID analysis

A.1 Monte Carlo simulation

In the following paragraph, the specifications of the MC simulation used in this thesis are listed:

- particle generation:
 - particle generator: particle gun (TRDbox generator)
 - $\sim 100,000$ events generated
 - 200 particles generated per event (50 e^+ , 50 e^- , 50 π^+ , 50 π^-)
 - momentum: 2 GeV/ c
 - azimuthal range: $0^\circ \leq \varphi \leq 360^\circ$
 - pseudo-rapidity range: $-0.9 \leq \eta \leq 0.9$
- TRD specifications:
 - ideal detector geometry
 - double-tracklet rejection in MCMs
 - magnetic field: +0.5 T
 - pedestal filter and gain filter in use (no tail cancellation filter)
 - 24 time bins
 - full TRAP configuration:
cf_pg-fpnp32_zs-s16-deh_tb24_trkl-b5p-fs1e24-ht200-qs0e24s24e23-
pidlinear-pt100_ptrg.r5570
 - full tracklet cluster information written to TRD.Tracklets.root file

A.2 Track cuts

The following track cuts were applied on the global offline tracks:

- using the class AliESDtrackCuts:
 - maximum transverse DCA to primary vertex: 3 cm

- maximum longitudinal DCA to primary vertex: 3 cm
 - require ITS refit
 - require at least one hit in one of the SPD layers
 - require TPC refit
 - maximum χ^2 of fit per TPC cluster: 4
 - minimum of clusters in the TPC: 80
 - range in pseudo-rapidity: $-0.9 \leq \eta \leq 0.9$
 - reject kink daughters
- other cuts:
 - particle from primary vertex (using MC truth)
 - must be electron or a pion (using MC truth)
 - average momentum in the TRD: $\geq 0.9 \text{ GeV}/c$

A.3 LQND results

In the following paragraphs, the relevant plots for the calculation of the PID performance using the multi-dimensional likelihood approach are presented. They are shown for the full charge information extracted from both positively and negatively charged offline tracks and online tracklets. The distributions of the deposited charge and the corresponding spline interpolations are shown only for layer 0, as they are similar in all layers. For the LUTs, only the processed versions are presented.

Deposited charge distributions and spline interpolations

1D — offline:

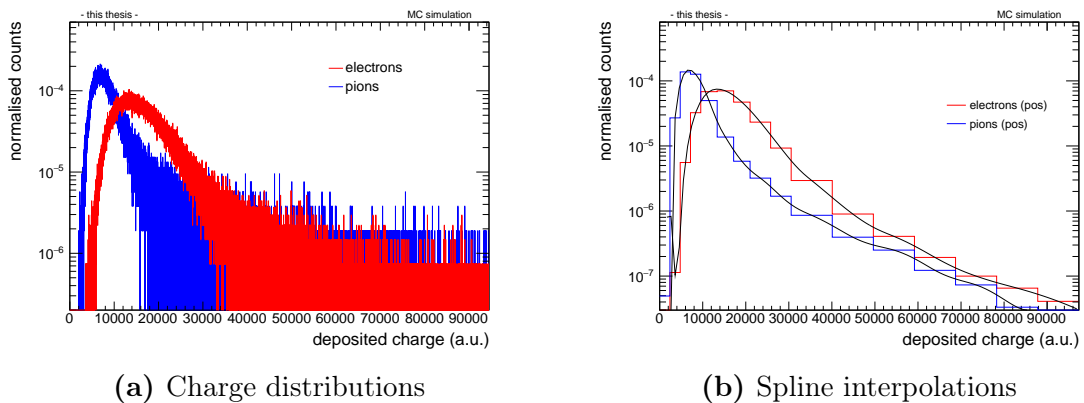
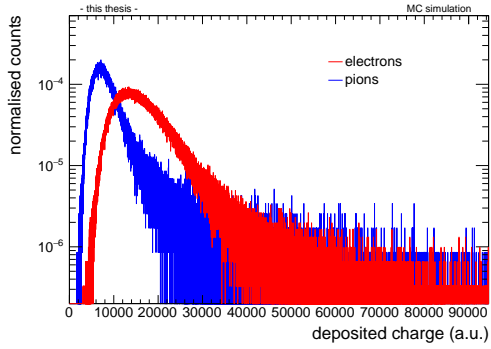
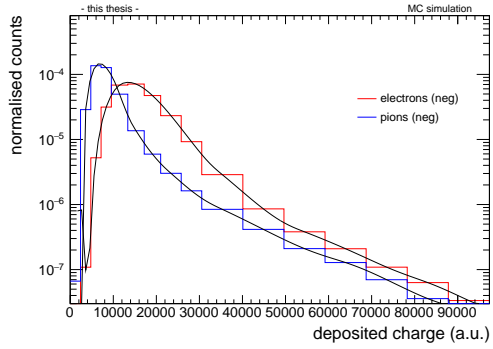


Figure A.1: Offline tracks, 1D, positive charge



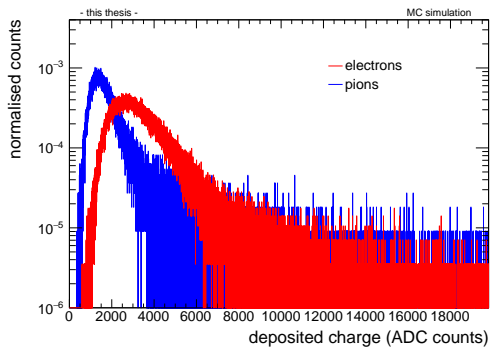
(a) Charge distributions



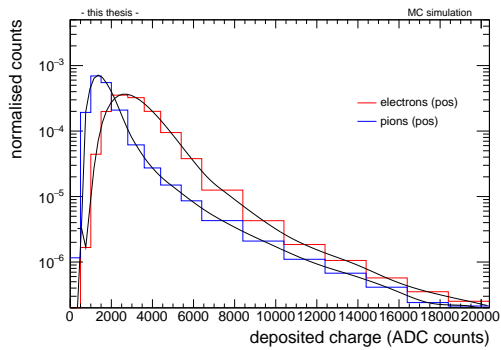
(b) Spline interpolations

Figure A.2: Offline tracks, 1D, negative charge

1D — online:

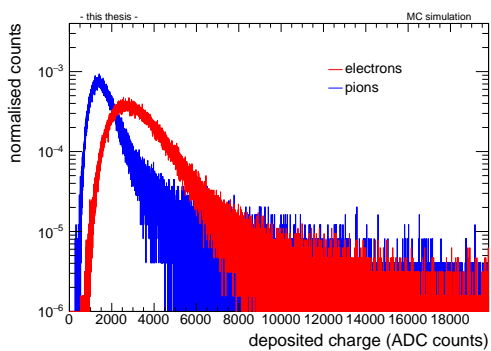


(a) Charge distributions

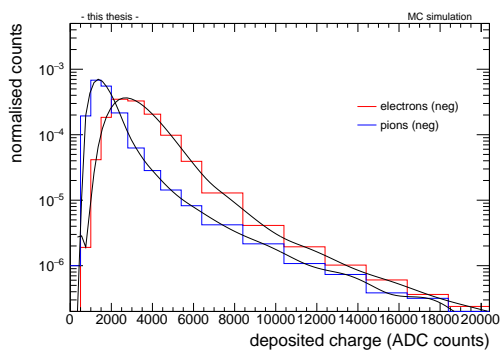


(b) Spline interpolations

Figure A.3: Online tracklets, 1D, positive charge



(a) Charge distributions



(b) Spline interpolations

Figure A.4: Online tracklets, 1D, negative charge

2D — offline:

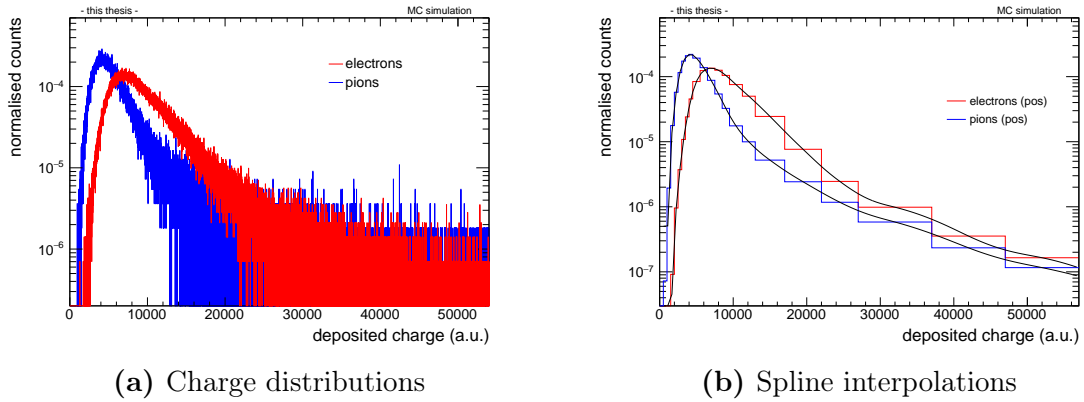


Figure A.5: Offline tracks, 2D (slice 1), positive charge

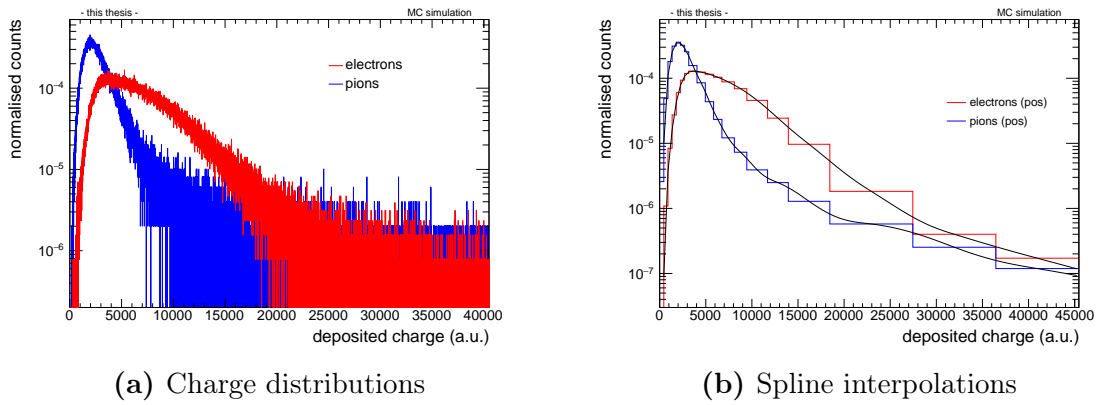


Figure A.6: Offline tracks, 2D (slice 2), positive charge

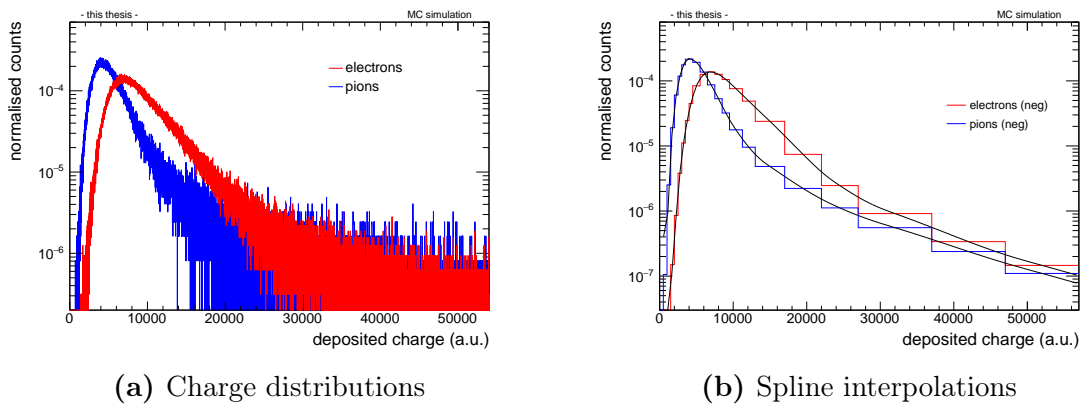
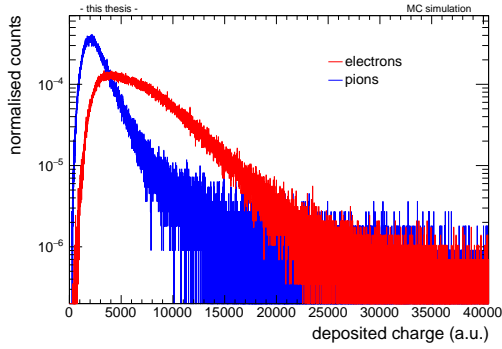
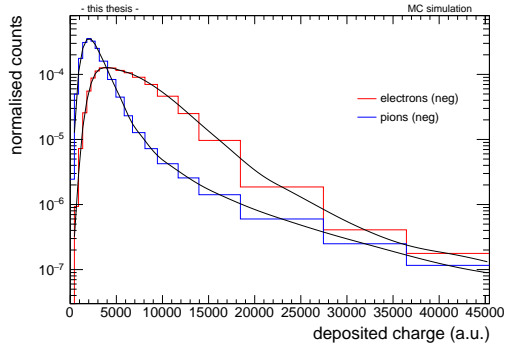


Figure A.7: Offline tracks, 2D (slice 1), negative charge



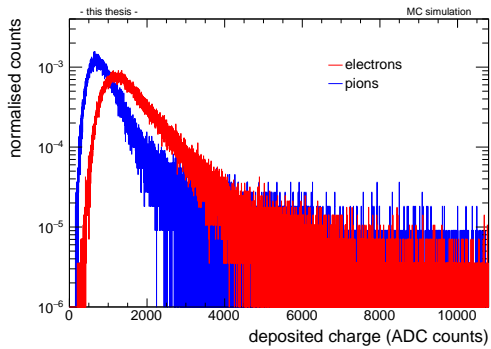
(a) Charge distributions



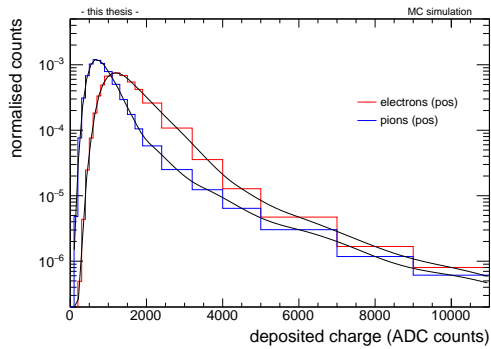
(b) Spline interpolations

Figure A.8: Offline tracks, 2D (slice 2), negative charge

2D — online:

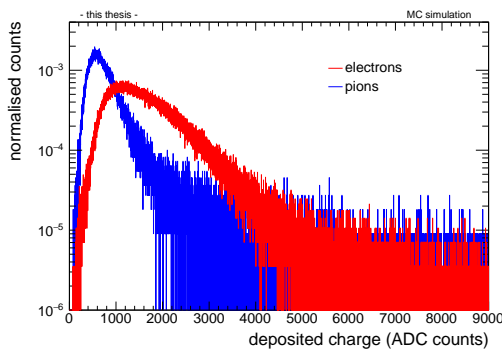


(a) Charge distributions

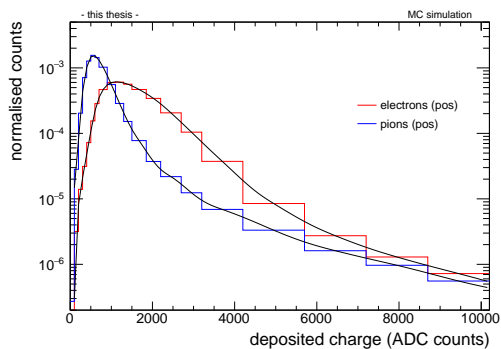


(b) Spline interpolations

Figure A.9: Online tracklets, 2D (slice 1), positive charge



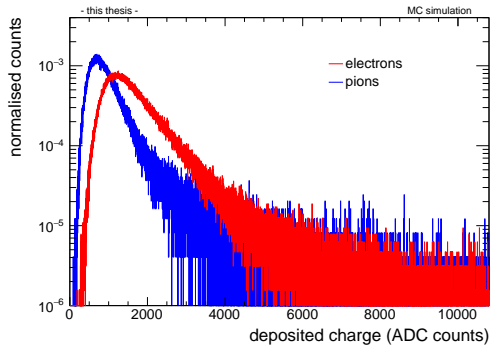
(a) Charge distributions



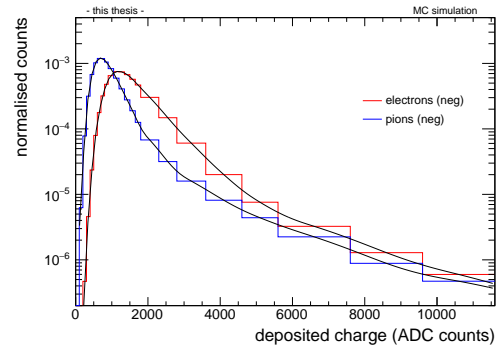
(b) Spline interpolations

Figure A.10: Online tracklets, 2D (slice 2), positive charge

Appendix A Tracklet-based PID analysis

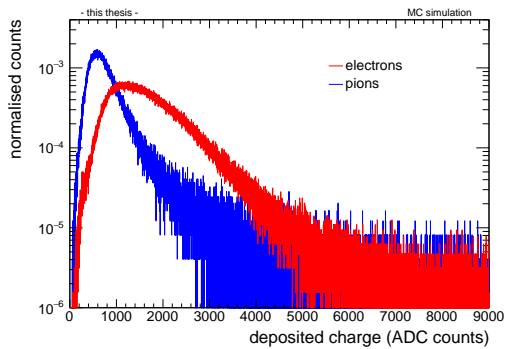


(a) Charge distributions

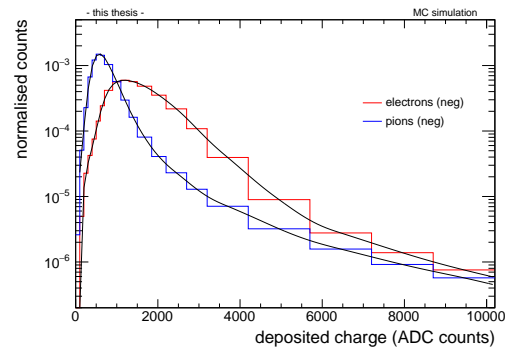


(b) Spline interpolations

Figure A.11: Online tracklets, 2D (slice 1), negative charge



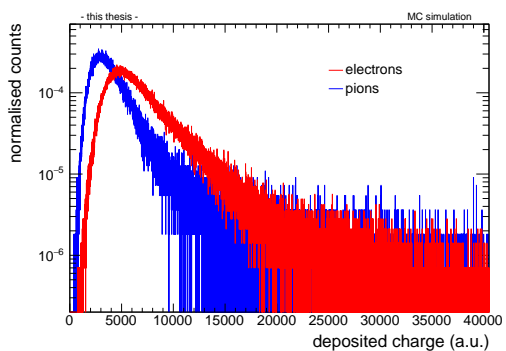
(a) Charge distributions



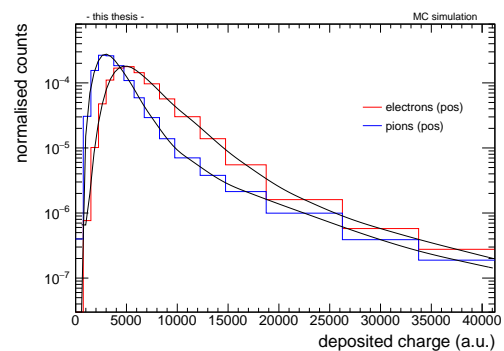
(b) Spline interpolations

Figure A.12: Online tracklets, 2D (slice 2), negative charge

3D — offline:

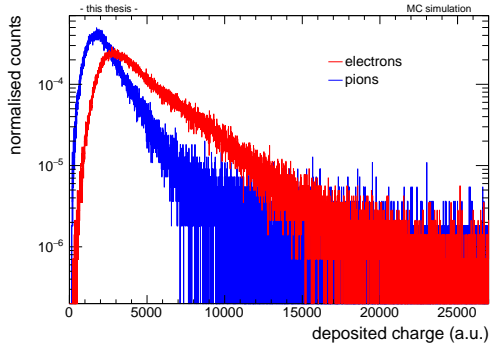


(a) Charge distributions

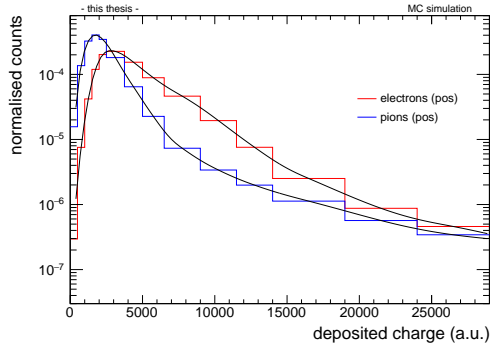


(b) Spline interpolations

Figure A.13: Offline tracks, 3D (slice 1), positive charge

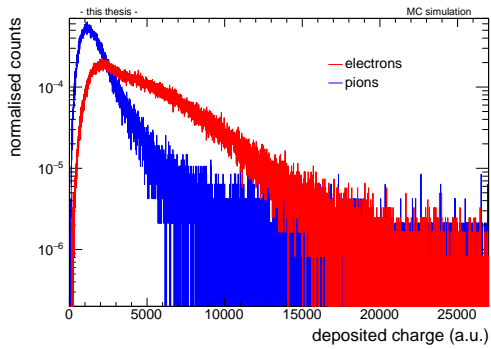


(a) Charge distributions

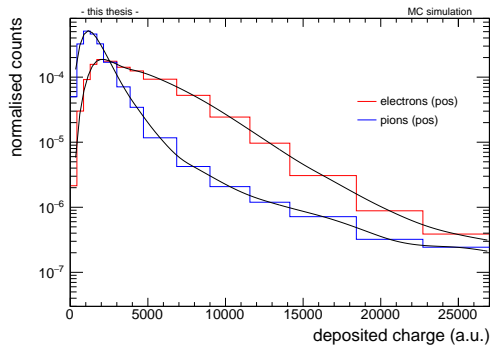


(b) Spline interpolations

Figure A.14: Offline tracks, 3D (slice 2), positive charge

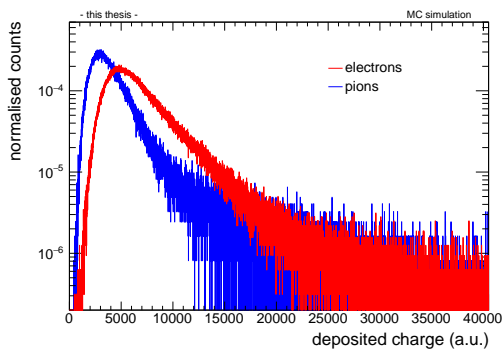


(a) Charge distributions

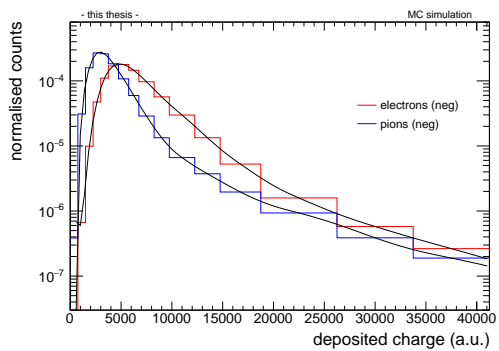


(b) Spline interpolations

Figure A.15: Offline tracks, 3D (slice 3), positive charge



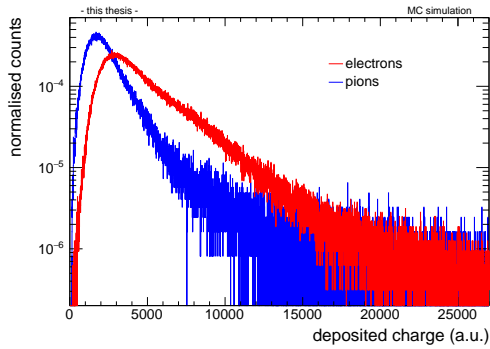
(a) Charge distributions



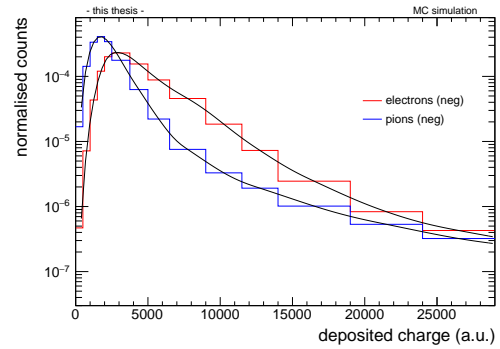
(b) Spline interpolations

Figure A.16: Offline tracks, 3D (slice 1), negative charge

Appendix A Tracklet-based PID analysis

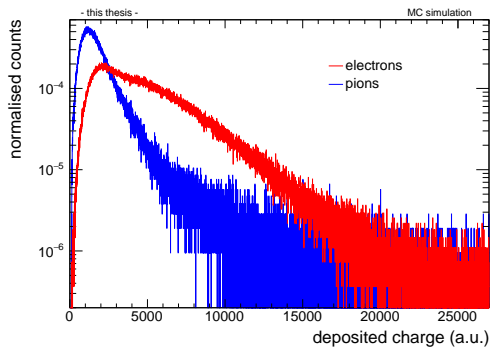


(a) Charge distributions

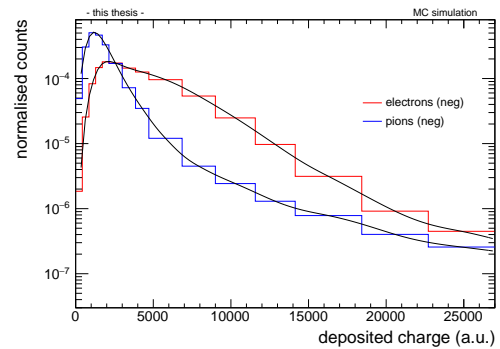


(b) Spline interpolations

Figure A.17: Offline tracks, 3D (slice 2), negative charge



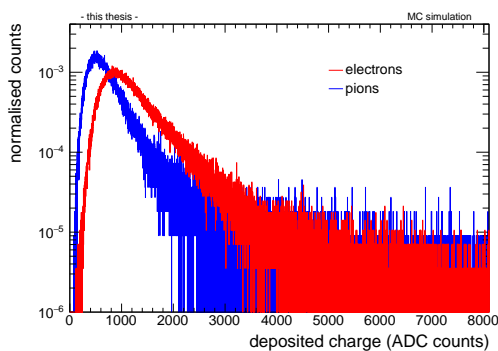
(a) Charge distributions



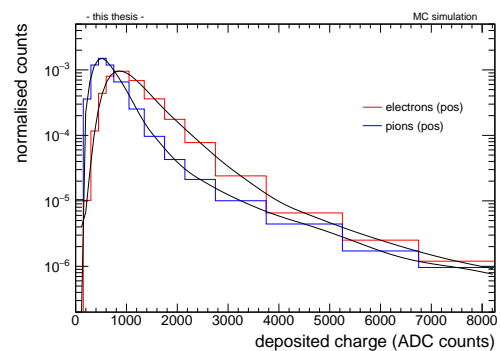
(b) Spline interpolations

Figure A.18: Offline tracks, 3D (slice 3), negative charge

3D — online:

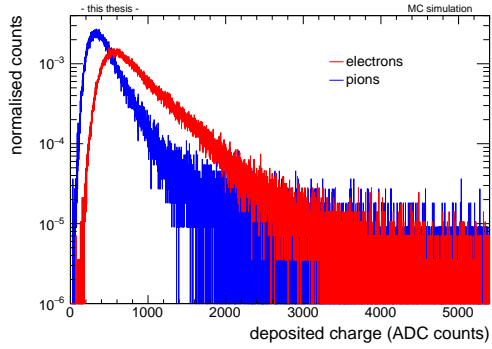


(a) Charge distributions

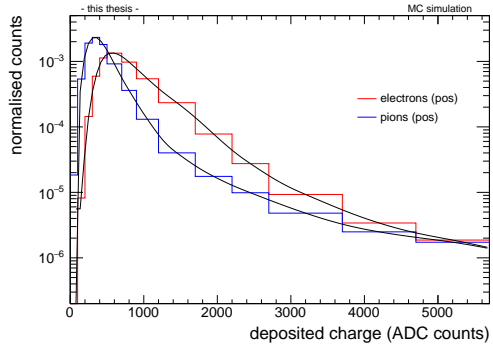


(b) Spline interpolations

Figure A.19: Online tracklets, 3D (slice 1), positive charge

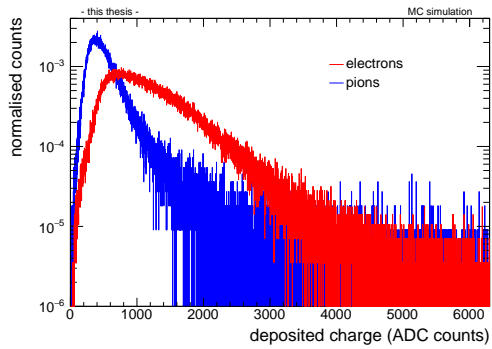


(a) Charge distributions

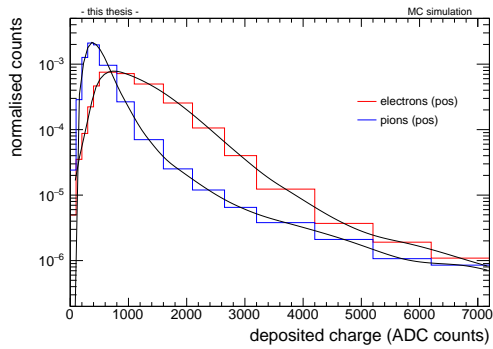


(b) Spline interpolations

Figure A.20: Online tracklets, 3D (slice 2), positive charge

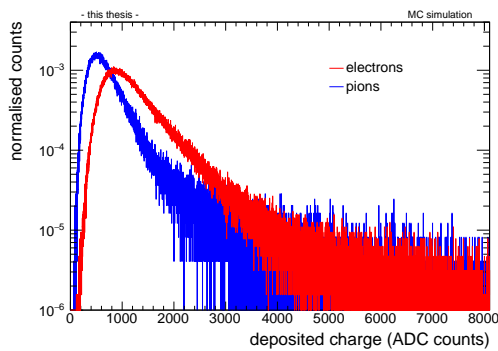


(a) Charge distributions

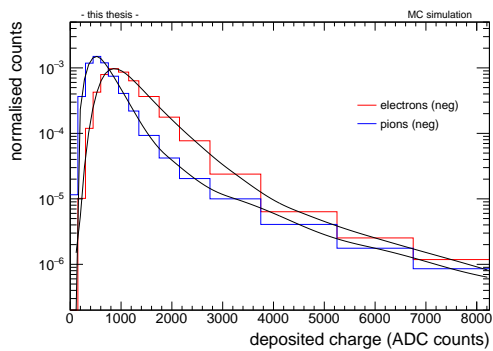


(b) Spline interpolations

Figure A.21: Online tracklets, 3D (slice 3), positive charge



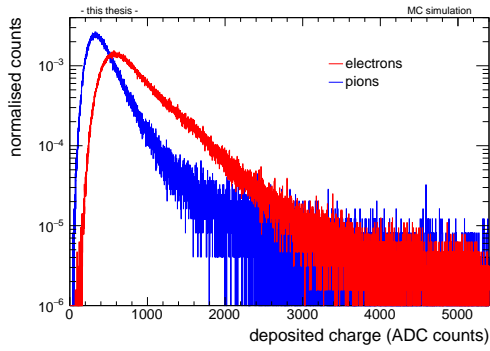
(a) Charge distributions



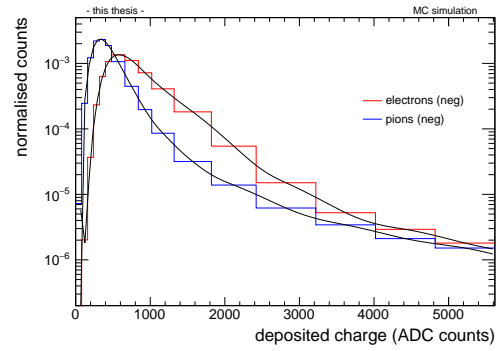
(b) Spline interpolations

Figure A.22: Online tracklets, 3D (slice 1), negative charge

Appendix A Tracklet-based PID analysis

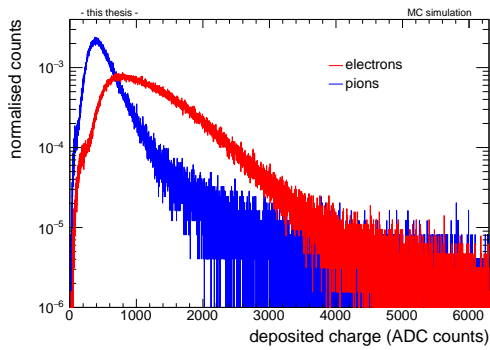


(a) Charge distributions

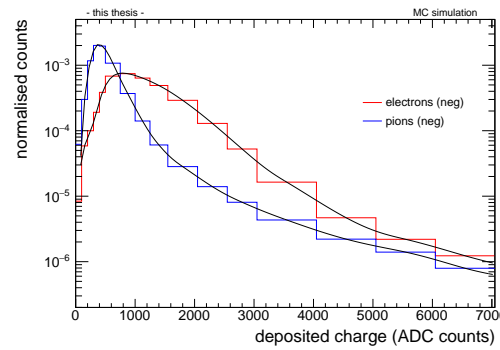


(b) Spline interpolations

Figure A.23: Online tracklets, 3D (slice 2), negative charge



(a) Charge distributions

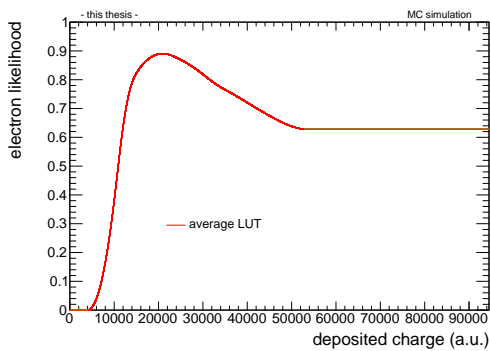


(b) Spline interpolations

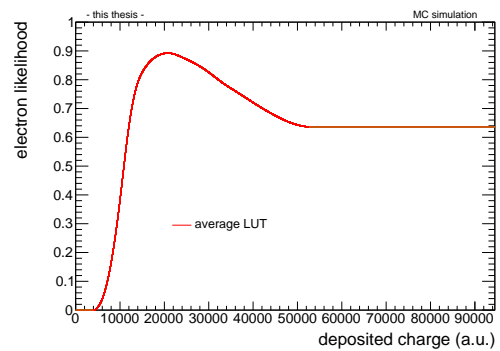
Figure A.24: Online tracklets, 3D (slice 3), negative charge

Look-up tables

1D — offline:



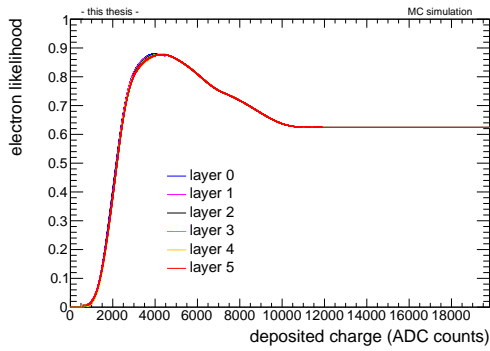
(a) Positive charge



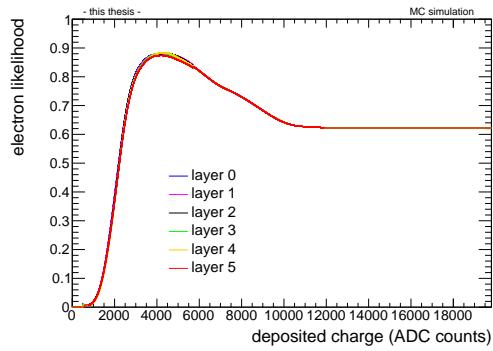
(b) Negative

Figure A.25: Processed LUTs for the offline tracks, 1D

1D — online:



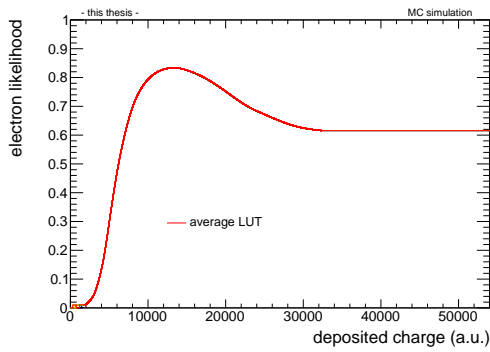
(a) Positive charge



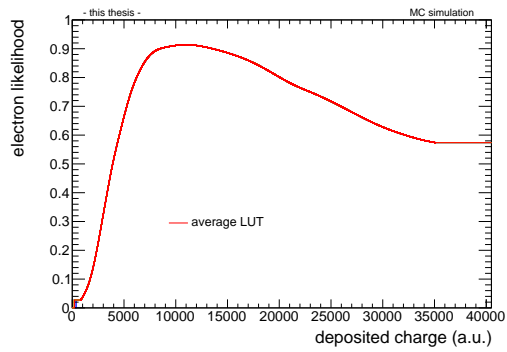
(b) Negative

Figure A.26: Processed LUTs for the online tracklets, 1D

2D — offline:

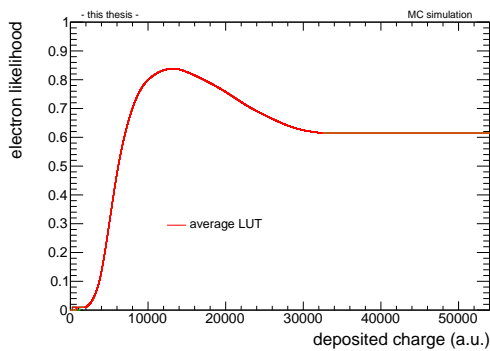


(a) Slice 1

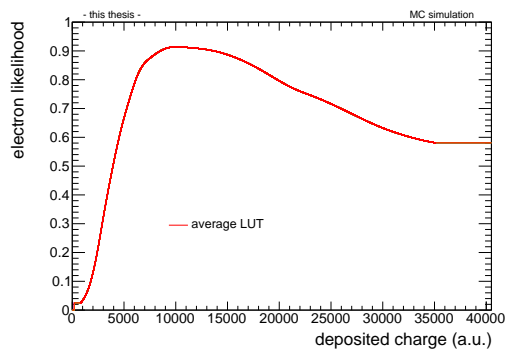


(b) Slice 2

Figure A.27: Processed LUTs for the offline tracks, 2D, positive charge



(a) Slice 1



(b) Slice 2

Figure A.28: Processed LUTs for the offline tracks, 2D, negative charge

2D — online:

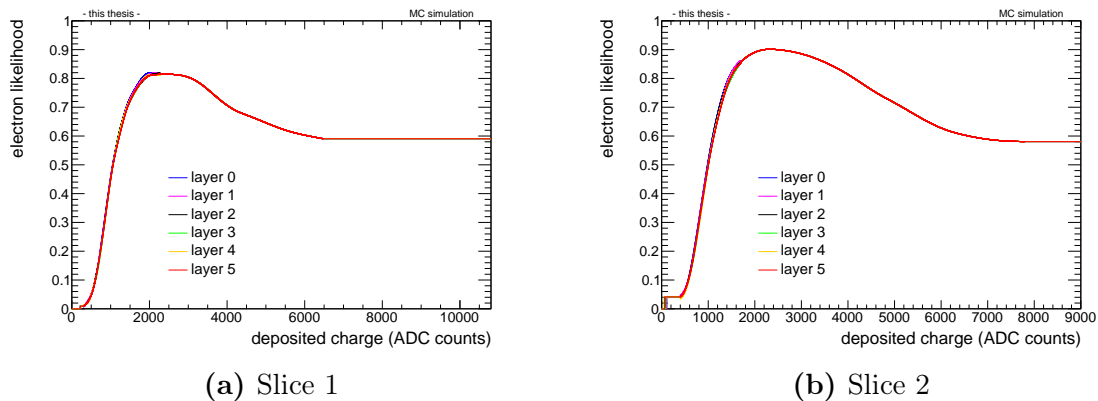


Figure A.29: Processed LUTs for the online tracklets, 2D, positive charge

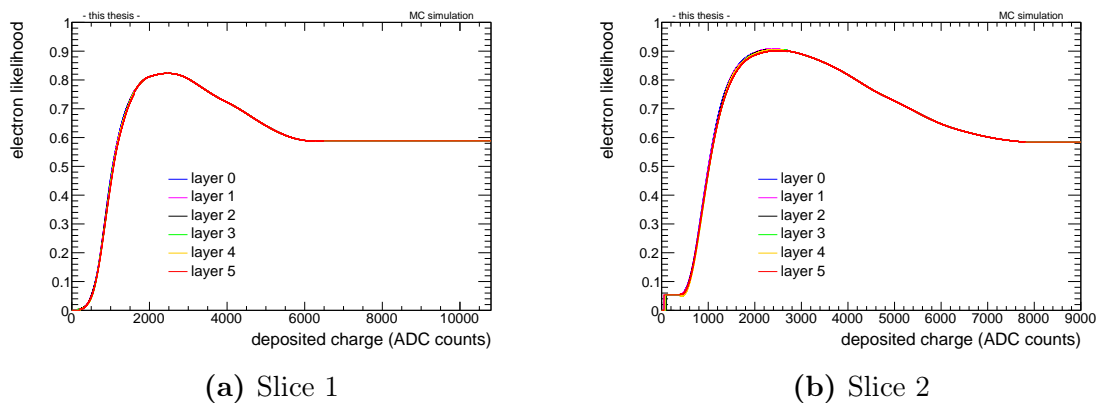


Figure A.30: Processed LUTs for the online tracks, 2D, negative charge

3D — offline:

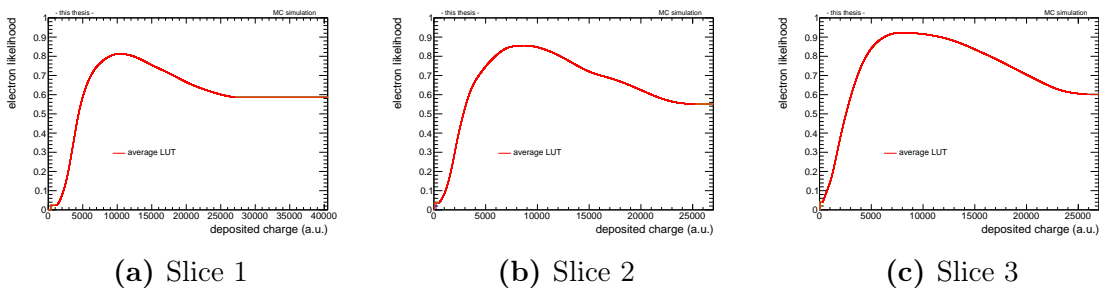


Figure A.31: Processed LUTs for the offline tracks, 3D, positive charge

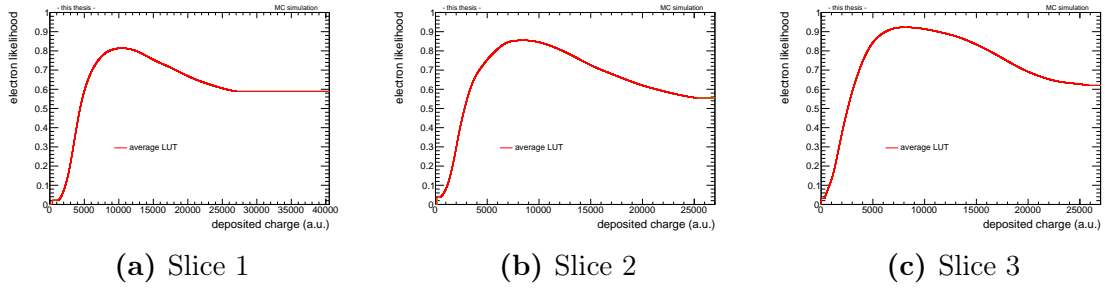


Figure A.32: Processed LUTs for the offline tracks, 3D, negative charge

3D — online:

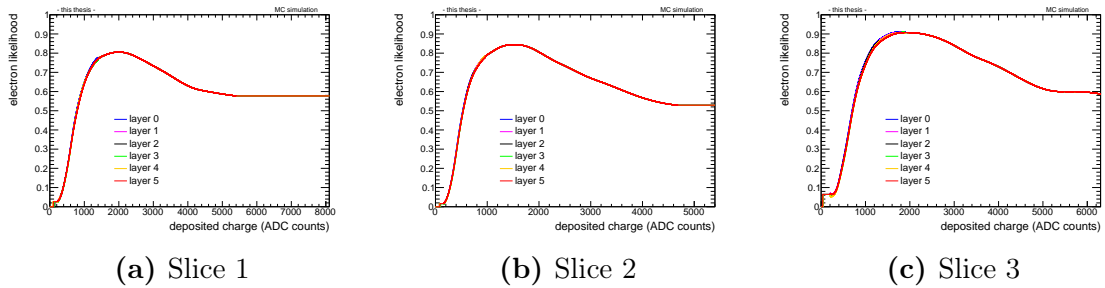


Figure A.33: Processed LUTs for the online tracklets, 3D, positive charge

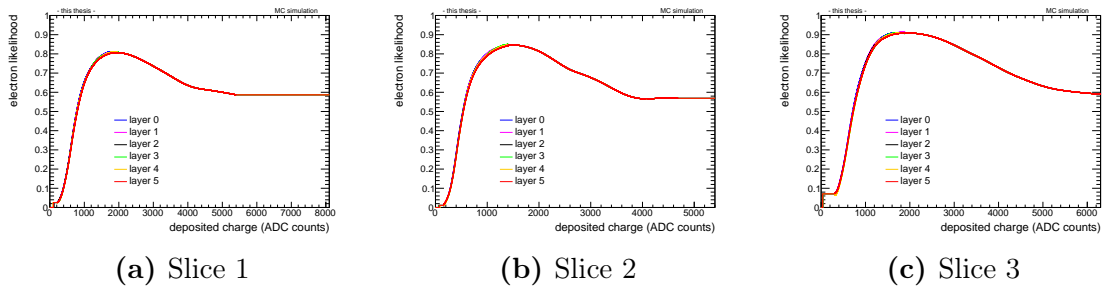
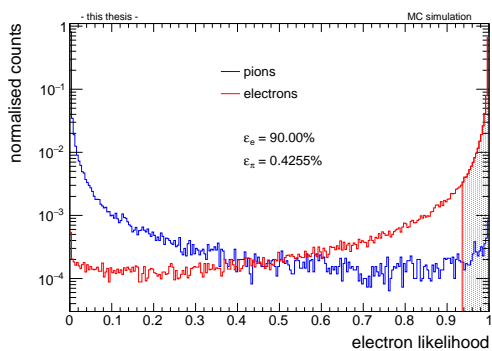


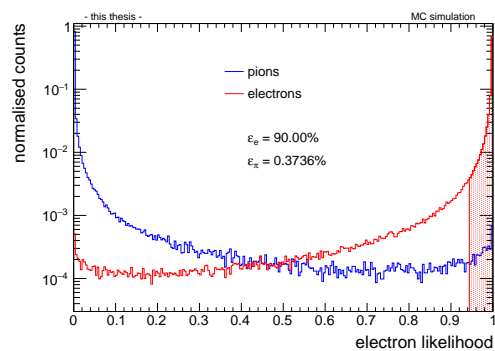
Figure A.34: Processed LUTs for the online tracks, 3D, negative charge

Likelihood distributions

1D — offline:



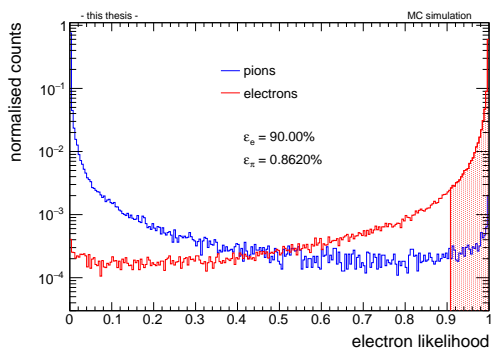
(a) Positive charge



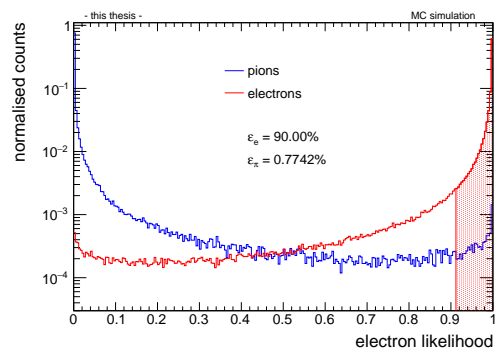
(b) Negative charge

Figure A.35: Offline tracks, 1D, $\varepsilon_e = 90\%$

1D — online:



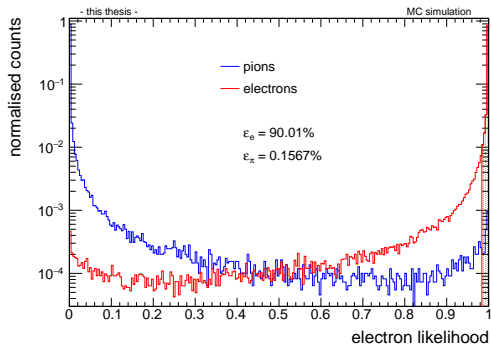
(a) Positive charge



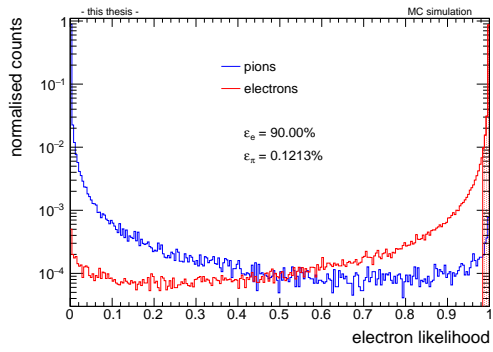
(b) Negative charge

Figure A.36: Online tracklets, 1D, $\varepsilon_e = 90\%$

2D — offline:



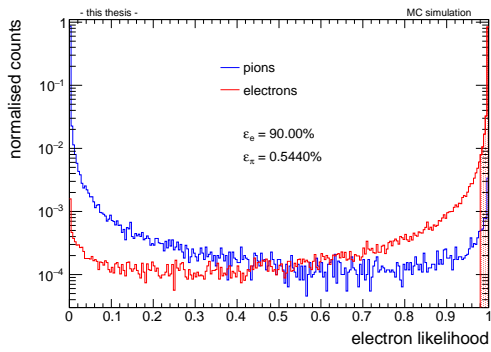
(a) Positive charge



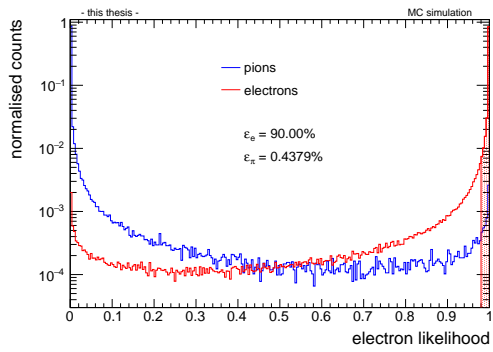
(b) Negative charge

Figure A.37: Offline tracks, 2D, $\varepsilon_e = 90\%$

2D — online:



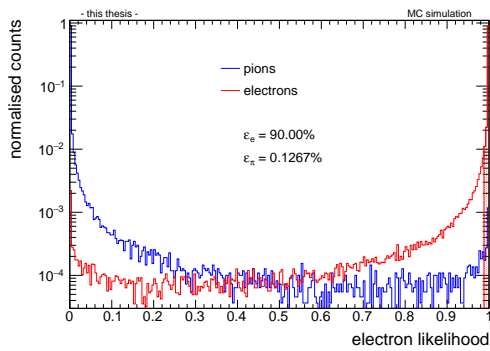
(a) Positive charge



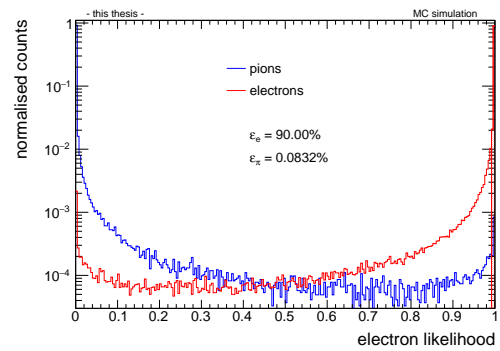
(b) Negative charge

Figure A.38: Online tracklets, 2D, $\varepsilon_e = 90\%$

3D — offline:



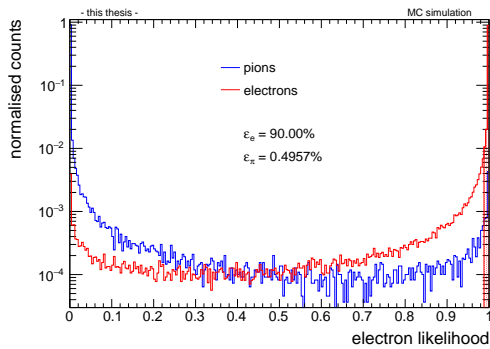
(a) Positive charge



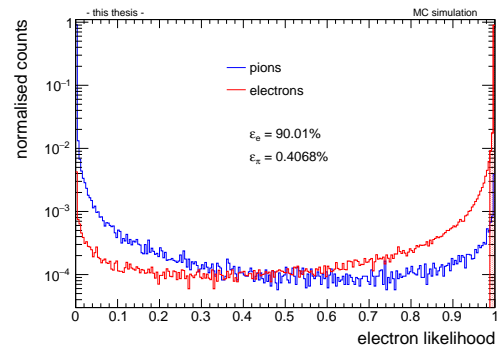
(b) Negative charge

Figure A.39: Offline tracks, 3D, $\varepsilon_e = 90\%$

3D — online:



(a) Positive charge



(b) Negative charge

Figure A.40: Online tracklets, 3D, $\varepsilon_e = 90\%$

Appendix B

Acronyms

ADC	Analog-to-Digital Converter
ALICE	A Large Ion Collider Experiment
ATLAS	A Toroidal LHC ApparatuS
CERN	European Organisation for Nuclear Research
CMS	Compact Muon Solenoid
CRU	Common Read-out Unit
CTP	Central Trigger Processor
DAQ	Data AcQuisition
DCA	Distance of Closest Approach
DCS	Detector Control System
ESD	Event Summary Data
FEE	Front-End Electronics
GEM	Gas Electron Multiplier
GTU	Global Tracking Unit
HLT	High-Level Trigger
IP	Interaction Point
ITS	Inner Tracking System
LEIR	Low Energy Ion Ring
LEP	Large Electron-Positron collider
LHC	Large Hadron Collider
LHCb	Large Hadron Collider beauty

Appendix B Acronyms

LUT	Look-Up Table
MC	Monte Carlo
MCM	Multi-Chip Module
MWPC	Multi-Wire Proportional Chamber
OCDB	Offline Condition DataBase
PASA	PreAmplifier-ShAper
PDG	Particle Data Group
PID	Particle IDentification
PS	Proton Synchrotron
PSB	Proton Synchrotron Booster
QCD	Quantum ChromoDynamics
QED	Quantum ElectroDynamics
QGP	Quark-Gluon Plasma
RHIC	Relativistic Heavy-Ion Collider
ROB	Read-Out Board
ROC	Read-Out Chamber
SDD	Silicon Drift Detector
SMU	SuperModule Unit
SPD	Silicon Pixel Detector
SPS	Super Proton Synchrotron
SSD	Silicon Strip Detector
TMU	Track Matching Unit
TOF	Time-Of-Flight
TPC	Time Projection Chamber
TR	Transition Radiation
TRAP	TRAcklet Processor
TRD	Transition Radiation Detector

Bibliography

- [1] J. J. Thomson. “Cathode Rays”. *Phil. Mag. Series 5* 44.269 (1897), pp. 293–316. URL: <http://dx.doi.org/10.1080/14786449708621070>.
- [2] E. Rutherford. “LIV. Collision of α particles with light atoms. IV. An anomalous effect in nitrogen”. *Phil. Mag.* 37.222 (1919), pp. 581–587.
- [3] James Chadwick. “Possible existence of a neutron”. *Nature* 129.3252 (1932), p. 312.
- [4] C. D. Anderson. “The apparent existence of easily deflectable positives”. *Science* 76 (1932), pp. 238–239.
- [5] S. H. Neddermeyer and C. D. Anderson. “Note on the nature of cosmic-ray particles”. *Phys. Rev.* 51.10 (1937), p. 884.
- [6] J. C. Street and E. C. Stevenson. “New evidence for the existence of a particle of mass intermediate between the proton and electron”. *Phys. Rev.* 52.9 (1937), p. 1003.
- [7] F. Reines and C. L. Cowan. “The neutrino”. *Nature* 178.4531 (1956), pp. 446–449.
- [8] H. Yukawa. “On the Interaction of Elementary Particles I”. *Proc. Phys. Math. Soc. Jap.* 17 (1935), pp. 48–57. DOI: [10.1143/PTPS.1.1](https://doi.org/10.1143/PTPS.1.1).
- [9] C. M. G. Lattes, G. P. S. Occhialini, and C. F. Powell. “Observations on the tracks of slow mesons in photographic emulsions”. *Nature* 160.4066 (1947), pp. 453–456.
- [10] G. D. Rochester and C. C. Butler. “Evidence for the existence of new unstable elementary particles”. *Nature* 160.4077 (1947), p. 855.
- [11] M. Gell-Mann. “A schematic model of baryons and mesons”. *Phys. Lett.* 8.3 (1964), pp. 214–215.
- [12] G. Zweig. “An SU (3) model for strong interaction symmetry and its breaking. Version 1” (1964). URL: <http://inspirehep.net/record/11881/files/CM-P00042883.pdf>.
- [13] M. Breidenbach et al. “Observed behavior of highly inelastic electron-proton scattering”. *Phys. Rev. Lett.* 23.16 (1969), p. 935.
- [14] D. P. Barber et al. “Discovery of Three-jet Events and a Test of Quantum Chromodynamics at PETRA”. *Phys. Rev. Lett.* 43.12 (1979), p. 830.
- [15] Mark Thomson. *Modern Particle Physics*. Cambridge: Cambridge University Press, 2013.

- [16] G. Aad et al. (ATLAS Collaboration). “Observation of a new particle in the search for the Standard Model Higgs boson with the ATLAS detector at the LHC”. *Phys. Lett. B* 716.1 (2012), pp. 1–29.
- [17] S. Chatrchyan et al. (CMS Collaboration). “Observation of a new boson at a mass of 125 GeV with the CMS experiment at the LHC”. *Phys. Lett. B* 716.1 (2012), pp. 30–61.
- [18] *CERN web page*. URL: <https://home.cern/> (visited on 01/26/2017).
- [19] P. Braun-Munzinger and J. Stachel. “The quest for the quark–gluon plasma”. *Nature* 448.7151 (2007), pp. 302–309.
- [20] E. V. Shuryak. “Theory of Hadronic Plasma”. *Sov. Phys. JETP* 47 (1978). [Zh. Eksp. Teor. Fiz.74,408(1978)], pp. 212–219.
- [21] F. Carminati et al. (ALICE Collaboration). “ALICE: Physics Performance Report, Volume I”. *Journal of Physics G: Nuclear and Particle Physics* 30.11 (2004), p. 1517. URL: <http://stacks.iop.org/0954-3899/30/i=11/a=001>.
- [22] P. Cortese et al. (ALICE Collaboration). *ALICE Transition Radiation Detector: Technical Design Report*. Technical Design Report ALICE. Geneva: CERN, 2001. URL: <https://cds.cern.ch/record/519145>.
- [23] C. Patrignani et al. (Particle Data Group). “Review of Particle Physics”. *Chin. Phys. C* 40.10 (2016), p. 100001. URL: <http://dx.doi.org/10.1088/1674-1137/40/10/100001>.
- [24] *Fermilab web page*. URL: <http://www.fnal.gov/pub/science/particle-physics-101/science-matter-energy-space-time.html> (visited on 02/05/2017).
- [25] Nobel Media AB. *The Nobel Prize in Physics 1979*. 2014. URL: http://www.nobelprize.org/nobel_prizes/physics/laureates/1979/ (visited on 01/12/2017).
- [26] H. Satz. “The Quark-Gluon Plasma – A Short Introduction”. *Nucl. Phys. A* 862–863 (2011). The Sixth International Conference on Physics and Astrophysics of Quark Gluon Plasma (ICPAQGP-2010), pp. 4–12. ISSN: 0375-9474. DOI: <http://dx.doi.org/10.1016/j.nuclphysa.2011.05.014>. URL: <http://www.sciencedirect.com/science/article/pii/S0375947411003435>.
- [27] S. Borsanyi et al. (Wuppertal-Budapest Collaboration). “Is there still any T_c mystery in lattice QCD? Results with physical masses in the continuum limit III”. *JHEP* 09 (2010), p. 073. DOI: [10.1007/JHEP09\(2010\)073](https://doi.org/10.1007/JHEP09(2010)073). arXiv: [1005.3508](https://arxiv.org/abs/1005.3508) [hep-lat].
- [28] A. Bazavov et al. (HotQCD Collaboration). “Equation of state in (2+1)-flavor QCD”. *Phys. Rev. D* 90 (2014), p. 094503. DOI: [10.1103/PhysRevD.90.094503](https://doi.org/10.1103/PhysRevD.90.094503). arXiv: [1407.6387](https://arxiv.org/abs/1407.6387) [hep-lat].

- [29] Rajeev S. Bhalerao. “Relativistic heavy-ion collisions”. *Proceedings, 1st Asia-Europe-Pacific School of High-Energy Physics (AEPSHEP): Fukuoka, Japan, October*. 2014, pp. 219–239. DOI: [10.5170/CERN-2014-001.219](https://doi.org/10.5170/CERN-2014-001.219). arXiv: [1404.3294](https://arxiv.org/abs/1404.3294) [nucl-th]. URL: <https://inspirehep.net/record/1290394/files/arXiv:1404.3294.pdf>.
- [30] S. Sarkar, H. Satz, and B. Sinha. *The Physics of the Quark–Gluon Plasma: Introductory Lectures*. Berlin Heidelberg: Springer, 2010.
- [31] S. Chatrchyan et al. (CMS Collaboration). “Observation of sequential Upsilon suppression in PbPb collisions”. *Phys. Rev. Lett.* 109 (2012), p. 222301. DOI: [10.1103/PhysRevLett.109.222301](https://doi.org/10.1103/PhysRevLett.109.222301). arXiv: [1208.2826](https://arxiv.org/abs/1208.2826) [nucl-ex].
- [32] B. Abelev et al. (ALICE Collaboration). “Centrality, rapidity and transverse momentum dependence of J/ψ suppression in Pb-Pb collisions at $\sqrt{s_{NN}}=2.76$ TeV”. *Phys. Lett.* B734 (2014), pp. 314–327. DOI: [10.1016/j.physletb.2014.05.064](https://doi.org/10.1016/j.physletb.2014.05.064). arXiv: [1311.0214](https://arxiv.org/abs/1311.0214) [nucl-ex].
- [33] L. Evans and P. Bryant. “LHC machine”. *JINST* 3.08 (2008), S08001. URL: <http://stacks.iop.org/1748-0221/3/i=08/a=S08001>.
- [34] B. Abelev et al. (ALICE Collaboration). “Performance of the ALICE Experiment at the CERN LHC”. *International journal of modern physics A* (2014).
- [35] CERN Communication Group. *CERN LHC: the guide. faq. frequently asked questions*. Geneva: CERN, 2006. URL: <http://cds.cern.ch/record/999421>.
- [36] G. Aad et al. (ATLAS Collaboration). “The ATLAS Experiment at the CERN Large Hadron Collider”. *JINST* 3.08 (2008), S08003. URL: <http://stacks.iop.org/1748-0221/3/i=08/a=S08003>.
- [37] S. Chatrchyan et al. (CMS Collaboration). “The CMS experiment at the CERN LHC”. *JINST* 3.08 (2008), S08004. URL: <http://stacks.iop.org/1748-0221/3/i=08/a=S08004>.
- [38] A. Augusto Alves Jr et al. (LHCb Collaboration). “The LHCb Detector at the LHC”. *JINST* 3.08 (2008), S08005. URL: <http://stacks.iop.org/1748-0221/3/i=08/a=S08005>.
- [39] K. Aamodt et al. (ALICE Collaboration). “The ALICE experiment at the CERN LHC”. *JINST* 3.08 (2008), S08002. URL: <http://stacks.iop.org/1748-0221/3/i=08/a=S08002>.
- [40] *ALICE Collaboration*. URL: <http://alice-collaboration.web.cern.ch/> (visited on 01/12/2017).
- [41] L. Betev and P. Chochula. *Definition of the ALICE Coordinate System and Basic Rules for Sub-detector Components Numbering*. 2003. URL: <https://edms.cern.ch/file/406391/2/ALICE-INT-2003-038.pdf> (visited on 01/28/2017).

- [42] J. Adam et al. (ALICE Collaboration). “Centrality dependence of the pseudorapidity density distribution for charged particles in Pb-Pb collisions at $\sqrt{s_{\text{NN}}} = 5.02$ TeV” (2016). arXiv: [1612.08966](https://arxiv.org/abs/1612.08966) [nucl-ex].
- [43] J. Klein. “Jet Physics with A Large Ion Collider Experiment at the Large Hadron Collider”. Doctoral Thesis. University of Heidelberg, 2014.
- [44] *The ALICE Off-line Project*. URL: <http://aliweb.cern.ch/Offline/> (visited on 01/12/2017).
- [45] *ROOT Data Analysis Framework*. URL: <https://root.cern.ch/> (visited on 01/12/2017).
- [46] The ALICE Collaboration. “The ALICE Transition Radiation Detector: construction, operation, and performance”. *In preparation* (2017).
- [47] I. M. Frank and V. L. Ginzburg. “Radiation of a uniform moving electron due to its transition from one medium into another”. *J. Phys.(USSR)* 9 (1945), p. 353.
- [48] E. Sicking. “Alignment of ALICE TRD Modules Using Cosmic Ray Data”. Diploma Thesis. Westfälische Wilhelms-Universität Münster, 2009.
- [49] C. Adler et al. “Position reconstruction in drift chambers operated with Xe, (15%)”. *Nucl. Instrum. Meth.* 540.1 (2005), pp. 140–157. ISSN: 0168-9002. DOI: <http://doi.org/10.1016/j.nima.2004.11.016>. URL: <http://www.sciencedirect.com/science/article/pii/S0168900204024131>.
- [50] A. Andronic (ALICE TRD Collaboration). “Electron identification performance with ALICE TRD prototypes”. *Nucl. Instrum. Meth.* 522 (2004), pp. 40–44. URL: <https://arxiv.org/abs/physics/0402131>.
- [51] J. Stiller. “Gain Calibration of the ALICE TRD using the Decay of $^{83\text{m}}\text{Kr}$ and Alignment of the ALICE TRD”. Diploma Thesis. University of Heidelberg, 2011.
- [52] M. Fasel. “Single-electron analysis and open charm cross section in proton-proton collisions at $\sqrt{s} = 7$ TeV”. Doctoral Thesis. Technische Universität Darmstadt, 2012.
- [53] D. Lohner. “Anisotropic flow of direct photons in Pb-Pb collisions at $\sqrt{s_{\text{NN}}} = 2.76$ TeV”. Doctoral Thesis. University of Heidelberg, 2013.
- [54] B. Abelev et al. (ALICE Collaboration). *Upgrade of the ALICE Experiment: Letter of Intent*. Tech. rep. CERN-LHCC-2012-012. LHCC-I-022. ALICE-UG-002. Geneva: CERN, 2012. URL: <https://cds.cern.ch/record/1475243>.
- [55] P. Antonioli, A. Kluge, and W. Riegler. *Upgrade of the ALICE Readout & Trigger System*. Tech. rep. CERN-LHCC-2013-019. ALICE-TDR-015. 2013. URL: <https://cds.cern.ch/record/1603472>.
- [56] P. Buncic, M. Krzewicki, and P. Vande Vyvre. *Technical Design Report for the Upgrade of the Online-Offline Computing System*. Tech. rep. CERN-LHCC-2015-006. ALICE-TDR-019. 2015. URL: <https://cds.cern.ch/record/2011297>.

- [57] ALICE TRD Collaboration. “ALICE TRD Upgrade Discussion Paper”. *ALICE internal* (2016).
- [58] B. Heß. “Online Electron Identification for Triggering with the ALICE Transition Radiation Detector”. Diploma Thesis. University of Heidelberg, 2011.
- [59] A. Wilk. “Particle Identification using Artificial Neural Networks with the ALICE Transition Radiation Detector”. Doctoral Thesis. Westfälische Wilhelms-Universität Münster, 2010.

Bibliography

Erklärung:

Ich versichere, dass ich diese Arbeit selbstständig verfasst habe und keine anderen als die angegebenen Quellen und Hilfsmittel benutzt habe.

Heidelberg, den (Datum)